STARS

Electronic Theses and Dissertations, 2020-

2020

Exoplanets: Correlated Noise and Cautionary Tales

Ryan Challener
University of Central Florida

Part of the Stars, Interstellar Medium and the Galaxy Commons

Find similar works at: https://stars.library.ucf.edu/etd2020

University of Central Florida Libraries http://library.ucf.edu

Showcase of Text, Archives, Research & Scholarship

EXOPLANETS: CORRELATED NOISE AND CAUTIONARY TALES

by

RYAN C. CHALLENER
B.S. Physics and Astronomy, University of Rochester, 2014
B.A. Mathematics, University of Rochester, 2014

A dissertation submitted in partial fulfilment of the requirements
for the degree of Doctor of Philosophy in Phyics, Planetary Sciences Track
in the Department of Physics
in the College of Sciences
at the University of Central Florida
Orlando, Florida

Spring Term
2020

Major Professor: Joseph Harrington

ABSTRACT

Transiting exoplanets provide the best opportunity for planetary characterization, and thus the search for life outside the Solar System. These planets orbit such that they pass in front ("transit") and behind ("eclipse") their host star, and a spectrum of the lost flux constrains the atmospheric properties of the planet. In transits, the flux modulation scales with the cross-sectional area of the planet, and the spectrum includes signatures of molecules in the upper atmosphere of the planet's terminator, which the host star's light passes through on the way to the observer. With eclipses, the lost flux is the direct emission of the planet, a spectrum of which contains emission and absorption features of molecules in the atmosphere depending on atmospheric thermal structure. These signals scale with the size and brightness of the planet and are so dwarfed by the brightness of the host star that only $\gtrsim 1000$ K Jupiter-sized planets are observable with current instrumentation. In this work, I develop new techniques and compare existing data analysis methods to extract weak planetary signals. Chapter 2 describes a new elliptical photometry data analysis approach to disentangle exoplanet observations from telescope vibrations. Chapter 3 describes an analysis of *Spitzer Space Telescope* observations of eclipses of the planet WASP-29b using elliptical photometry and two different light curve modeling methods, and addresses the differences between results. In Chapter 4, I analyze two similar observations of WASP-34b using a grazing eclipse light-curve model. Finally, in Chapter 5 I reanalyze all *Spitzer* eclipse observations of the Neptune-sized GJ 436b, applying the lessons learned from my earlier works, and comparing my results with the literature.

ACKNOWLEDGMENTS

This dissertation would not have been possible without the unending support of family, friends, and colleagues. While this dissertation represents my scientific growth, I have learned much more than is presented here during my time at the University of Central Florida, in no small part thanks to the wonderful people who have surrounded me.

First, endless thanks to my fiancée, Emily, who has endured countless late nights and sacrificed much to make this work possible. Your constant encouragement has been invaluable. I am ever grateful.

I also must thank my advisor, Joseph Harrington. I learned so much from your research guidance, career advice, your thoroughness, and your extraordinary diligence. I will carry these lessons throughout my career.

I thank Katie McIntyre for her help and friendship throughout the years. Thanks for keeping me sane when the work seemed insurmountable. You've helped me at least as much as you think I've helped you.

Thanks to my family and friends, who have been nothing but supportive in my pursuit of this degree. And thanks to the students in my research group whose assistance helped make this work possible.

TABLE OF CONTENTS

LIST OF FIGURES

LIST OF TABLES

CHAPTER 1: INTRODUCTION

Exoplanet science is a rapidly-growing field. Since the first exoplanet discoveries (Wolszczan 1994, Mayor & Queloz 1995, Marcy & Butler 1996), over 4,000 additional planets have been found, with thousands more candidate detections (NASA Exoplanet Archive). The most easily observed of these planets are as large as Jupiter with orbital periods of a few days and extreme temperatures. However, as instrumentation and data analysis methods improve, smaller and colder planets are discovered (e.g., Anglada-Escudé et al. 2016, Gillon et al. 2017). With careful analysis and sufficient observational resources, Earth-like planets may be characterizable with the next generation of space telescopes (Morley et al. 2017).

Though there are many methods to detect exoplanets, the vast majority are discovered with the radial velocity or transit methods. If a star is host to a planet, the gravitational pull of the planet induces a wobble in the star's motion. This radial velocity is detectable in high-resolution spectroscopy as a Doppler shift in the star's atomic and molecular emission lines, provided a component of the wobble is along the observer's line of sight. The periodicity and amplitude of the wobble provide the planet's orbital period and mass, respectively. The transit method observes the brightness variation of the planet-star system, searching for periodic dimming as the planet passes between the observer and the star. The magnitude of the dimming is proportional to the cross-sectional area of the planet, and the periodicity of the dimming is the planet's orbital period. Early planet discoveries were therefore biased toward large, hot planets on very short orbital periods.

Following initial exoplanet discovery, dedicated instrumentation and observatories were constructed to leverage these methods. Working in tandem, ground-based transit surveys (e.g., Bakos et al. 2002, Pollacco et al. 2006) and high-resolution spectrographs (e.g., Queloz et al. 2000, Mayor et al. 2003) confirmed dozens of additional planets. Later, space-based observatories like the *Kepler Space Telescope* (Basri et al. 2005) and its successor mission *K2* (Howell et al. 2014) discovered thousands of transiting planets using space-based photometry, enabling exoplanet population studies (e.g., Fulton et al. 2017, Petigura et al. 2018). The next generation of planet finders, like the Transiting Exoplanet Survey Satellite (Ricker et al. 2014) and the Characterising Exoplanets Satellite (Benz et al. 2018) have started discovering planets ideal for follow-up characterization (e.g., Huang et al. 2018, Vanderspek et al. 2019).

1.1   Atmospheric Characterization

Transiting planets remain the best targets for exoplanet atmospheric characterization. There are three types of observations used: the planet passing in front of its host star ("transit"), the planet passing behind its host star ("eclipse"), and a full orbit of the planet ("phase curve").

In transmission spectroscopy (transits), the presence of opaque molecules in a planetary atmosphere causes an apparent increase in the size of the planet. Since molecular opacity is wavelength-dependent, and each molecule has a unique spectral signature, a transmission spectrum can tell us which molecules are present in the atmosphere. Due to the star-planet geometry, light must pass through a significant portion of the atmosphere (the terminator), so transmission spectra are sensitive to trace molecules, and molecular absorption signatures are adversely affected by high-altitude clouds and hazes. The earliest works, using ground-based observatories, were limited to measurements of planetary radius and orbital parameters (e.g., Charbonneau et al. 2000, Henry et al. 2000, Jha et al. 2000, Deeg et al. 2001). Using the *Hubble Space Telescope* (HST, e.g., Lallo 2012),

Charbonneau et al. (2002) detected the presence of sodium and Vidal-Madjar et al. (2003) detected an extended hydrogen envelope around planet. Later observations with the *Spitzer Space Telescope* and upgraded HST instrumentation showed water in hot-Jupiter atmospheres (e.g., Deming et al. 2013, Kreidberg et al. 2015, Evans et al. 2017) and a range of cloudless to cloudy atmospheres (Sing et al. 2016).

With eclipses, the lost flux as a function of wavelength is a spectrum of the thermal radiation and reflected light from the planet's day side. Like transits, this spectrum constrains atmospheric composition and thermal structure, and the eclipse ephemeris places additional constraints on orbital eccentricity. Deming et al. (2005) observed the first exoplanet emission, confirmed the planetary temperature, and determined a circular orbit. Eclipse spectroscopy led to the proposal of thermal inversions in hot-Jupiter atmospheres (e.g., Burrows et al. 2007, Knutson et al. 2008) and subsequent contention (Line et al. 2016). While current exoplanet emission spectra have insufficient resolution for detailed compositional analyses, studies have debated the carbon-to-oxygen ratio of exoplanet atmospheres (Madhusudhan et al. 2011, Cowan et al. 2012, Crossfield et al. 2012, Swain et al. 2013, Line et al. 2014, Stevenson et al. 2014, Oreshenko et al. 2017). The shape of eclipse ingress and egress (when the planet is partially eclipsed) can be used to build two-dimensional thermal maps of the brightest planets (Majeau et al. 2012, de Wit et al. 2012).

Phase curves show the brightness of the planet as its day and night sides rotate into and out of view. This enables study of planets' heat distribution efficiency through comparison of the day-night temperature gradient (e.g., Harrington et al. 2006, Cowan et al. 2007). Planets have been observed with phase-curve maxima shifted from the eclipse center, implying the hottest part of the planet is shifted eastward from the substellar point (e.g., Knutson et al. 2007, 2009, Crossfield et al. 2010). This shift implies strong winds and, thus, an atmosphere, so its presence can be used to search for atmospheres on small hot planets that would be otherwise undetectable (Kreidberg et al. 2019).

This process of exoplanetary atmosphere inference is called retrieval. Exoplanet signals are weak, and their spectra are not well sampled, so retrieval models must be simple. They typically describe temperature as a function of pressure represented with up to five parameters and a parameter for the abundances of a few key molecular absorbers, such as H_2O, CO, CO_2, and CH_4. The entire planet is described by this single one-dimensional atmosphere.

Uncertainties on model parameters are large, and the goodness-of-fit parameter space is complex, with many similarly good fits. When measuring exoplanetary atmospheres, one must be careful to use an approach that accurately determines best fits and parameter uncertainties. This is achieved with a Bayesian approach, where prior knowledge (the "prior" distribution) about atmospheric parameters is adjusted (the "posterior" distribution) to reflect new observations. Rather than attempting to compute the complex posterior, Markov-chain Monte Carlo (MCMC) sampling estimates the posterior by drawing samples from that distribution, weighted by goodness-of-fit.

Several Bayesian atmospheric retrieval packages exist, using a variety of planet models and MCMC algorithms (e.g., Madhusudhan & Seager 2009, Benneke & Seager 2012, Line et al. 2013, Waldmann et al. 2015, Harrington et al. 2020). In this work, I use the Bayesian Atmospheric Radiative Transfer code (Harrington et al. 2020, Cubillos et al. 2020, Blecic et al. 2020, `https://github.com/exosports/BART`) to retrieve exoplanet atmospheres. In keeping with BART's Reproducible Research Software License, each chapter has an associated compendium containing the data inputs, outputs, and instructions to reproduce the work done therein, including best-fit models and correlated-noise diagnostics.

1.2 Observational Challenges

Observations like these are challenging. Transit and eclipse signals of hot Jupiters, the largest and brightest planets, are of order 1% and 0.1% of the host stars' flux, respectively, so stellar photon noise is significant. Planets become brighter relative to their host stars at longer wavelengths, but Earth's atmosphere becomes more opaque, brighter, and more variable in the infrared, so space-based telescopes are a necessity. The *Hubble Space Telescope* (HST) and the *Spitzer Space Telescope* (Werner et al. 2004) have proven the most successful exoplanet observatories. Before exhausting its cryogen in 2009, *Spitzer* provided a 3.6–24 μm spectral range useful for transiting exoplanets; from then until the end of the mission in early 2020, it was limited to broadband photometry at the 3.6 and 4.5 μm filters of the InfraRed Array Camera (Fazio et al. 2004). The Wide Field Camera 3 spectrograph aboard HST provides a 1.1–1.7 μm wavelength range. Neither instrument was designed for exoplanet study, and telescope effects ("systematics") make observations even more difficult, but innovative observational techniques and data analysis methods have made the science possible.

Spitzer suffers from two primary systematics, both of which dwarf the exoplanet signals: a time-dependent flux variation due to pointing settling and charge trapping, and an intrapixel gain variation that creates a correlation between telescope pointing and measured flux. The first effect can typically be modeled out with a low-degree polynomial model, or avoided by discarding the beginning of an observation, when the telescope is still settling to its position. The intrapixel effect is much more complex, and the field has developed many methods to correct it, including polynomial
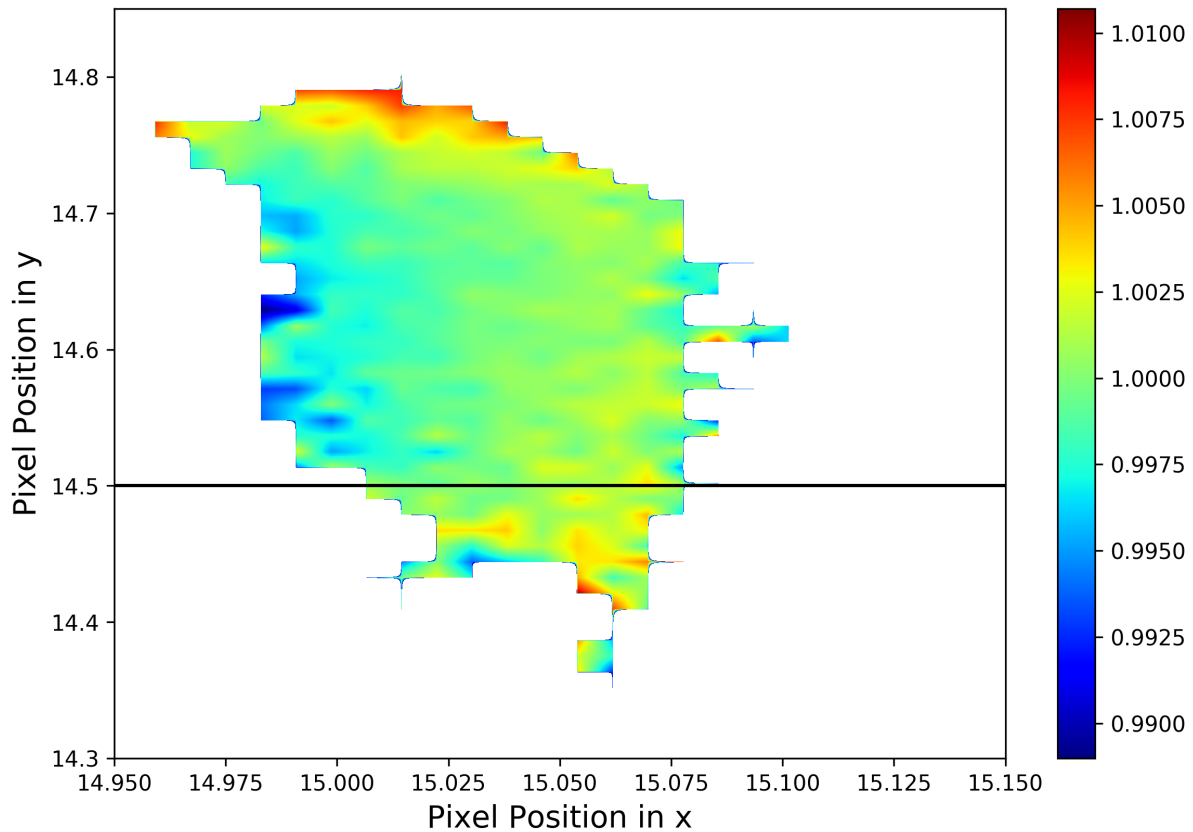
Figure 1.1: An example BiLinearly Interpolated Subpixel Sensitivity map. This map shows the gain variation of the *Spitzer* InfraRed Array Camera as a function of subpixel position.

pixel maps (e.g., Charbonneau et al. 2008), measured pixel maps (Ingalls et al. 2012), BiLinearly Interpolated Subpixel Sensitivity maps (Figure 1.1, Stevenson et al. 2012), Pixel-Level Decorrelation (Deming et al. 2015), Independent Component Analysis (Morello et al. 2015), and Gaussian Processes (Evans et al. 2015). These techniques made many detections possible, but there were still uncorrected effects in the data (e.g., Stevenson et al. 2017, Jenkins et al. 2019).

In this work, I characterized the orbits and atmospheres of several exoplanets using *Spitzer* eclipse observations. I developed an elliptical-photometry data-analysis technique that corrects for false positives due to telescope vibration. This method dynamically adjusts to telescope motion to avoid losing flux, minimizing correlated and non-correlated noise, which is necessary for many exoplanet observations that push the boundary of detectability. In Chapter 2, I present this new method, with application to a *Spitzer* search for transits of Proxima Centauri b. In Chapter 3, I apply elliptical photometry to weak eclipse observations of WASP-29b in order to characterize the planet, with a focus on differences between light-curve modeling techniques. Similarly, in Chapter 4 I analyze *Spitzer* eclipses of WASP-34b, employing a modified light-curve model to account for the planet's grazing orbit. Lastly, in Chapter 5 I apply these techniques to an analysis of *Spitzer* eclipses of GJ 436b.

1.3   List of References

Anglada-Escudé, G., Amado, P. J., Barnes, J., Berdiñas, Z. M., Butler, R. P., Coleman, G. A. L., de La Cueva, I., Dreizler, S., Endl, M., Giesers, B., Jeffers, S. V., Jenkins, J. S., Jones, H. R. A., Kiraga, M., Kürster, M., López-González, M. J., Marvin, C. J., Morales, N., Morin, J., Nelson, R. P., Ortiz, J. L., Ofir, A., Paardekooper, S.-J., Reiners, A., Rodríguez, E., Rodríguez-López, C., Sarmiento, L. F., Strachan, J. P., Tsapras, Y., Tuomi, M., & Zechmeister, M. 2016, Nature, 536, 437

Bakos, G. Á., Lázár, J., Papp, I., Sári, P., & Green, E. M. 2002, PASP, 114, 974

Basri, G., Borucki, W. J., & Koch, D. 2005, New A Rev., 49, 478

Benneke, B. & Seager, S. 2012, ApJ, 753, 100

Benz, W., Ehrenreich, D., & Isaak, K. CHEOPS: CHaracterizing ExOPlanets Satellite, 84

Blecic, J., Harrington, J., Cubillos, P. E., Bowman, M. O., Rojo, P., Stemm, M. M., Challener, R. C., Foster, A. J., Dobbs-Dixon, I., Foster, A. S., Lust, N. B., Blumenthal, S. D., Bruce, D., Himes, M. D., & Loredo, T. J. 2020, ApJ, in prep

Burrows, A., Hubeny, I., Budaj, J., Knutson, H. A., & Charbonneau, D. 2007, ApJ, 668, L171

Charbonneau, D., Brown, T. M., Latham, D. W., & Mayor, M. 2000, ApJ, 529, L45

Charbonneau, D., Brown, T. M., Noyes, R. W., & Gilliland, R. L. 2002, ApJ, 568, 377

Charbonneau, D., Knutson, H. A., Barman, T., Allen, L. E., Mayor, M., Megeath, S. T., Queloz, D., & Udry, S. 2008, ApJ, 686, 1341

Cowan, N. B., Agol, E., & Charbonneau, D. 2007, MNRAS, 379, 641

Cowan, N. B., Machalek, P., Croll, B., Shekhtman, L. M., Burrows, A., Deming, D., Greene, T., & Hora, J. L. 2012, ApJ, 747, 82

Crossfield, I. J. M., Barman, T., Hansen, B. M. S., Tanaka, I., & Kodama, T. 2012, ApJ, 760, 140

Crossfield, I. J. M., Hansen, B. M. S., Harrington, J., Cho, J. Y. K., Deming, D., Menou, K., & Seager, S. 2010, ApJ, 723, 1436

Cubillos, P. E., Harrington, J., Blecic, J., Himes, M. D., Rojo, P. M., Loredo, T. J., Lust, N. B., Challener, R. C., Foster, A. J., Stemm, M. M., Foster, A. S., & Blumenthal, S. D. 2020, ApJ, in prep

de Wit, J., Gillon, M., Demory, B. O., & Seager, S. 2012, A&A, 548, A128

Deeg, H. J., Garrido, R., & Claret, A. 2001, New A, 6, 51

Deming, D., Knutson, H., Kammer, J., Fulton, B. J., Ingalls, J., Carey, S., Burrows, A., Fortney, J. J., Todorov, K., Agol, E., Cowan, N., Desert, J.-M., Fraine, J., Langton, J., Morley, C., & Showman, A. P. 2015, ApJ, 805, 132

Deming, D., Seager, S., Richardson, L. J., & Harrington, J. 2005, Nature, 434, 740

Deming, D., Wilkins, A., McCullough, P., Burrows, A., Fortney, J. J., Agol, E., Dobbs-Dixon, I., Madhusudhan, N., Crouzet, N., Desert, J.-M., Gilliland, R. L., Haynes, K., Knutson, H. A., Line, M., Magic, Z., Mand ell, A. M., Ranjan, S., Charbonneau, D., Clampin, M., Seager, S., & Showman, A. P. 2013, ApJ, 774, 95

Evans, T. M., Aigrain, S., Gibson, N., Barstow, J. K., Amundsen, D. S., Tremblin, P., & Mourier, P. 2015, MNRAS, 451, 680

Evans, T. M., Sing, D. K., Kataria, T., Goyal, J., Nikolov, N., Wakeford, H. R., Deming, D., Marley, M. S., Amundsen, D. S., Ballester, G. E., Barstow, J. K., Ben-Jaffel, L., Bourrier, V., Buchhave, L. A., Cohen, O., Ehrenreich, D., García Muñoz, A., Henry, G. W., Knutson, H., Lavvas, P., Lecavelier Des Etangs, A., Lewis, N. K., López-Morales, M., Mandell, A. M., Sanz-Forcada, J., Tremblin, P., & Lupu, R. 2017, Nature, 548, 58

Fazio, G. G., Hora, J. L., Allen, L. E., Ashby, M. L. N., Barmby, P., Deutsch, L. K., Huang, J. S., Kleiner, S., Marengo, M., Megeath, S. T., Melnick, G. J., Pahre, M. A., Patten, B. M., Polizotti, J., Smith, H. A., Taylor, R. S., Wang, Z., Willner, S. P., Hoffmann, W. F., Pipher, J. L., Forrest, W. J., McMurty, C. W., McCreight, C. R., McKelvey, M. E., McMurray, R. E., Koch, D. G., Moseley, S. H., Arendt, R. G., Mentzell, J. E., Marx, C. T., Losch, P., Mayman, P., Eichhorn, W., Krebs, D., Jhabvala, M., Gezari, D. Y., Fixsen, D. J., Flores, J., Shakoorzadeh, K., Jungo, R., Hakun, C., Workman, L., Karpati, G., Kichak, R., Whitley, R., Mann, S., Tollestrup, E. V., Eisenhardt, P., Stern, D., Gorjian, V., Bhattacharya, B., Carey, S., Nelson, B. O., Glaccum, W. J., Lacy, M., Lowrance, P. J., Laine, S., Reach, W. T., Stauffer, J. A., Surace, J. A., Wilson, G., Wright, E. L., Hoffman, A., Domingo, G., & Cohen, M. 2004, ApJS, 154, 10

Fulton, B. J., Petigura, E. A., Howard, A. W., Isaacson, H., Marcy, G. W., Cargile, P. A., Hebb, L.,
Weiss, L. M., Johnson, J. A., Morton, T. D., Sinukoff, E., Crossfield, I. J. M., & Hirsch, L. A.
2017, AJ, 154, 109

Gillon, M., Triaud, A. H. M. J., Demory, B.-O., Jehin, E., Agol, E., Deck, K. M., Lederer, S. M., de
Wit, J., Burdanov, A., Ingalls, J. G., Bolmont, E., Leconte, J., Raymond, S. N., Selsis, F., Turbet,
M., Barkaoui, K., Burgasser, A., Burleigh, M. R., Carey, S. J., Chaushev, A., Copperwheat,
C. M., Delrez, L., Fernand es, C. S., Holdsworth, D. L., Kotze, E. J., Van Grootel, V., Almleaky,
Y., Benkhaldoun, Z., Magain, P., & Queloz, D. 2017, Nature, 542, 456

Harrington, J., Hansen, B. M., Luszcz, S. H., Seager, S., Deming, D., Menou, K., Cho, J. Y. K., &
Richardson, L. J. 2006, Science, 314, 623

Harrington, J., Himes, M. D., Cubillos, P. E., Blecic, J., Rojo, P. M., Challener, R. C., Lust, N. B.,
Bowman, M. O., Blumenthal, S. D., Dobbs-Dixon, I., Foster, A. S., Foster, A. J., Green, M.,
Loredo, T. J., McIntyre, K. J., & Stemm, M. M. 2020, ApJ, in prep

Henry, G. W., Marcy, G. W., Butler, R. P., & Vogt, S. S. 2000, ApJ, 529, L41

Howell, S. B., Sobeck, C., Haas, M., Still, M., Barclay, T., Mullally, F., Troeltzsch, J., Aigrain, S.,
Bryson, S. T., Caldwell, D., Chaplin, W. J., Cochran, W. D., Huber, D., Marcy, G. W., Miglio,
A., Najita, J. R., Smith, M., Twicken, J. D., & Fortney, J. J. 2014, PASP, 126, 398

Huang, C. X., Burt, J., Vanderburg, A., Günther, M. N., Shporer, A., Dittmann, J. A., Winn, J. N.,
Wittenmyer, R., Sha, L., Kane, S. R., Ricker, G. R., Vand erspek, R. K., Latham, D. W., Seager,
S., Jenkins, J. M., Caldwell, D. A., Collins, K. A., Guerrero, N., Smith, J. C., Quinn, S. N.,
Udry, S., Pepe, F., Bouchy, F., Ségransan, D., Lovis, C., Ehrenreich, D., Marmier, M., Mayor,
M., Wohler, B., Haworth, K., Morgan, E. H., Fausnaugh, M., Ciardi, D. R., Christiansen, J.,

Charbonneau, D., Dragomir, D., Deming, D., Glidden, A., Levine, A. M., McCullough, P. R., Yu, L., Narita, N., Nguyen, T., Morton, T., Pepper, J., Pál, A., Rodriguez, J. E., Stassun, K. G., Torres, G., Sozzetti, A. r., Doty, J. P., Christensen-Dalsgaard, J., Laughlin, G., Clampin, M., Bean, J. L., Buchhave, L. A., Bakos, G. Á., Sato, B., Ida, S., Kaltenegger, L., Palle, E., Sasselov, D., Butler, R. P., Lissauer, J., Ge, J., & Rinehart, S. A. 2018, ApJ, 868, L39

Ingalls, J. G., Krick, J. E., Carey, S. J., Laine, S., Surace, J. A., Glaccum, W. J., Grillmair, C. C., & Lowrance, P. J. Society of Photo-Optical Instrumentation Engineers (SPIE) Conference Series, Vol. 8442, Intra-pixel gain variations and high-precision photometry with the Infrared Array Camera (IRAC), 84421Y

Jenkins, J. S., Harrington, J., Challener, R. C., Kurtovic, N. T., Ramirez, R., Peña, J., McIntyre, K. J., Himes, M. D., Rodríguez, E., Anglada-Escudé, G., Dreizler, S., Ofir, A., Peña Rojas, P. A., Ribas, I., Rojo, P., Kipping, D., Butler, R. P., Amado, P. J., Rodríguez-López, C., Kempton, E. M. R., Palle, E., & Murgas, F. 2019, MNRAS, 487, 268

Jha, S., Charbonneau, D., Garnavich, P. M., Sullivan, D. J., Sullivan, T., Brown, T. M., & Tonry, J. L. 2000, ApJ, 540, L45

Knutson, H. A., Charbonneau, D., Allen, L. E., Burrows, A., & Megeath, S. T. 2008, ApJ, 673, 526

Knutson, H. A., Charbonneau, D., Allen, L. E., Fortney, J. J., Agol, E., Cowan, N. B., Showman, A. P., Cooper, C. S., & Megeath, S. T. 2007, Nature, 447, 183

Knutson, H. A., Charbonneau, D., Cowan, N. B., Fortney, J. J., Showman, A. P., Agol, E., Henry, G. W., Everett, M. E., & Allen, L. E. 2009, ApJ, 690, 822

Kreidberg, L., Koll, D. D. B., Morley, C., Hu, R., Schaefer, L., Deming, D., Stevenson, K. B., Dittmann, J., Vanderburg, A., Berardo, D., Guo, X., Stassun, K., Crossfield, I., Charbonneau, D., Latham, D. W., Loeb, A., Ricker, G., Seager, S., & Vand erspek, R. 2019, Nature, 573, 87

Kreidberg, L., Line, M. R., Bean, J. L., Stevenson, K. B., Désert, J.-M., Madhusudhan, N., Fortney, J. J., Barstow, J. K., Henry, G. W., Williamson, M. H., & Showman, A. P. 2015, ApJ, 814, 66

Lallo, M. D. 2012, Optical Engineering, 51, 011011

Line, M. R., Knutson, H., Wolf, A. S., & Yung, Y. L. 2014, ApJ, 783, 70

Line, M. R., Stevenson, K. B., Bean, J., Desert, J.-M., Fortney, J. J., Kreidberg, L., Madhusudhan, N., Showman, A. P., & Diamond-Lowe, H. 2016, AJ, 152, 203

Line, M. R., Wolf, A. S., Zhang, X., Knutson, H., Kammer, J. A., Ellison, E., Deroo, P., Crisp, D., & Yung, Y. L. 2013, ApJ, 775, 137

Madhusudhan, N., Harrington, J., Stevenson, K. B., Nymeyer, S., Campo, C. J., Wheatley, P. J., Deming, D., Blecic, J., Hardy, R. A., Lust, N. B., Anderson, D. R., Collier-Cameron, A., Britt, C. B. T., Bowman, W. C., Hebb, L., Hellier, C., Maxted, P. F. L., Pollacco, D., & West, R. G. 2011, Nature, 469, 64

Madhusudhan, N. & Seager, S. 2009, ApJ, 707, 24

Majeau, C., Agol, E., & Cowan, N. B. 2012, ApJ, 747, L20

Marcy, G. W. & Butler, R. P. 1996, ApJ, 464, L147

Mayor, M., Pepe, F., Queloz, D., Bouchy, F., Rupprecht, G., Lo Curto, G., Avila, G., Benz, W., Bertaux, J. L., Bonfils, X., Dall, T., Dekker, H., Delabre, B., Eckert, W., Fleury, M., Gilliotte, A., Gojak, D., Guzman, J. C., Kohler, D., Lizon, J. L., Longinotti, A., Lovis, C., Megevand, D., Pasquini, L., Reyes, J., Sivan, J. P., Sosnowska, D., Soto, R., Udry, S., van Kesteren, A., Weber, L., & Weilenmann, U. 2003, The Messenger, 114, 20

Mayor, M. & Queloz, D. 1995, Nature, 378, 355

Morello, G., Waldmann, I. P., Tinetti, G., Howarth, I. D., Micela, G., & Allard, F. 2015, ApJ, 802, 117

Morley, C. V., Kreidberg, L., Rustamkulov, Z., Robinson, T., & Fortney, J. J. 2017, ApJ, 850, 121

Oreshenko, M., Lavie, B., Grimm, S. L., Tsai, S.-M., Malik, M., Demory, B.-O., Mordasini, C., Alibert, Y., Benz, W., Quanz, S. P., Trotta, R., & Heng, K. 2017, ApJ, 847, L3

Petigura, E. A., Marcy, G. W., Winn, J. N., Weiss, L. M., Fulton, B. J., Howard, A. W., Sinukoff, E., Isaacson, H., Morton, T. D., & Johnson, J. A. 2018, AJ, 155, 89

Pollacco, D. L., Skillen, I., Collier Cameron, A., Christian, D. J., Hellier, C., Irwin, J., Lister, T. A., Street, R. A., West, R. G., Anderson, D. R., Clarkson, W. I., Deeg, H., Enoch, B., Evans, A., Fitzsimmons, A., Haswell, C. A., Hodgkin, S., Horne, K., Kane, S. R., Keenan, F. P., Maxted, P. F. L., Norton, A. J., Osborne, J., Parley, N. R., Ryans, R. S. I., Smalley, B., Wheatley, P. J., & Wilson, D. M. 2006, PASP, 118, 1407

Queloz, D., Mayor, M., Weber, L., Blécha, A., Burnet, M., Confino, B., Naef, D., Pepe, F., Santos, N., & Udry, S. 2000, A&A, 354, 99

Ricker, G. R., Winn, J. N., Vanderspek, R., Latham, D. W., Bakos, G. Á., Bean, J. L., Berta-Thompson, Z. K., Brown, T. M., Buchhave, L., Butler, N. R., Butler, R. P., Chaplin, W. J., Charbonneau, D., Christensen-Dalsgaard, J., Clampin, M., Deming, D., Doty, J., De Lee, N., Dressing, C., Dunham, E. W., Endl, M., Fressin, F., Ge, J., Henning, T., Holman, M. J., Howard, A. W., Ida, S., Jenkins, J., Jernigan, G., Johnson, J. A., Kaltenegger, L., Kawai, N., Kjeldsen, H., Laughlin, G., Levine, A. M., Lin, D., Lissauer, J. J., MacQueen, P., Marcy, G., McCullough, P. R., Morton, T. D., Narita, N., Paegert, M., Palle, E., Pepe, F., Pepper, J., Quirrenbach, A., Rinehart, S. A., Sasselov, D., Sato, B., Seager, S., Sozzetti, A., Stassun, K. G., Sullivan, P., Szentgyorgyi, A., Torres, G., Udry, S., & Villasenor, J. Society of Photo-Optical Instrumentation Engineers (SPIE) Conference Series, Vol. 9143, Transiting Exoplanet Survey Satellite (TESS), 914320

Sing, D. K., Fortney, J. J., Nikolov, N., Wakeford, H. R., Kataria, T., Evans, T. M., Aigrain, S., Ballester, G. E., Burrows, A. S., Deming, D., Désert, J.-M., Gibson, N. P., Henry, G. W., Huitson, C. M., Knutson, H. A., Lecavelier Des Etangs, A., Pont, F., Showman, A. P., Vidal-Madjar, A., Williamson, M. H., & Wilson, P. A. 2016, Nature, 529, 59

Stevenson, K. B., Bean, J. L., Madhusudhan, N., & Harrington, J. 2014, ApJ, 791, 36

Stevenson, K. B., Harrington, J., Fortney, J. J., Loredo, T. J., Hardy, R. A., Nymeyer, S., Bowman, W. C., Cubillos, P., Bowman, M. O., & Hardin, M. 2012, ApJ, 754, 136

Stevenson, K. B., Line, M. R., Bean, J. L., Désert, J.-M., Fortney, J. J., Showman, A. P., Kataria, T., Kreidberg, L., & Feng, Y. K. 2017, AJ, 153, 68

Swain, M., Deroo, P., Tinetti, G., Hollis, M., Tessenyi, M., Line, M., Kawahara, H., Fujii, Y., Showman, A. P., & Yurchenko, S. N. 2013, Icarus, 225, 432

Vanderspek, R., Huang, C. X., Vanderburg, A., Ricker, G. R., Latham, D. W., Seager, S., Winn, J. N., Jenkins, J. M., Burt, J., Dittmann, J., Newton, E., Quinn, S. N., Shporer, A., Charbonneau, D., Irwin, J., Ment, K., Winters, J. G., Collins, K. A., Evans, P., Gan, T., Hart, R., Jensen, E. L. N., Kielkopf, J., Mao, S., Waalkes, W., Bouchy, F., Marmier, M., Nielsen, L. D., Ottoni, G., Pepe, F., Ségransan, D., Udry, S., Henry, T., Paredes, L. A., James, H.-S., Hinojosa, R. H., Silverstein, M. L., Palle, E., Berta-Thompson, Z., Crossfield, I., Davies, M. D., Dragomir, D., Fausnaugh, M., Glidden, A., Pepper, J., Morgan, E. H., Rose, M., Twicken, J. D., Villaseñor, J. N. S., Yu, L., Bakos, G., Bean, J., Buchhave, L. A., Christensen-Dalsgaard, J., Christiansen, J. L., Ciardi, D. R., Clampin, M., De Lee, N., Deming, D., Doty, J., Jernigan, J. G., Kaltenegger, L., Lissauer, J. J., McCullough, P. R., Narita, N., Paegert, M., Pal, A., Rinehart, S., Sasselov, D., Sato, B., Sozzetti, A., Stassun, K. G., & Torres, G. 2019, ApJ, 871, L24

Vidal-Madjar, A., Lecavelier des Etangs, A., Désert, J. M., Ballester, G. E., Ferlet, R., Hébrard, G., & Mayor, M. 2003, Nature, 422, 143

Waldmann, I. P., Tinetti, G., Rocchetto, M., Barton, E. J., Yurchenko, S. N., & Tennyson, J. 2015, ApJ, 802, 107

Werner, M. W., Roellig, T. L., Low, F. J., Rieke, G. H., Rieke, M., Hoffmann, W. F., Young, E., Houck, J. R., Brandl, B., Fazio, G. G., Hora, J. L., Gehrz, R. D., Helou, G., Soifer, B. T., Stauffer, J., Keene, J., Eisenhardt, P., Gallagher, D., Gautier, T. N., Irace, W., Lawrence, C. R., Simmons, L., Van Cleve, J. E., Jura, M., Wright, E. L., & Cruikshank, D. P. 2004, ApJS, 154, 1

Wolszczan, A. 1994, Science, 264, 538

CHAPTER 2: IDENTIFICATION AND MITIGATION OF A VIBRATIONAL TELESCOPE SYSTEMATIC WITH APPLICATION TO SPITZER

Ryan C. Challener[1]**, Joseph Harrington**[1]**, James Jenkins**[2,3]**, Nicolás T. Kurtovic**[2]**, Ricardo Ramirez**[2]**, Jose Peña**[2]**, Kathleen J. McIntyre**[1]**, Michael D. Himes**[1]**, Eloy Rodríguez**[4]**, Guillem Anglada-Escudé**[5]**, Stefan Dreizler**[6]**, Aviv Ofir**[7]**, Ignasi Ribas**[8,9]**, Patricio Rojo**[2]**, David Kipping**[10]**, R. Paul Butler**[11]**, Pedro J. Amado**[4]**, Cristina Rodríguez-López**[4]**, Eliza M.-R. Kempton**[12,13]**, Enric Palle**[14,15]**, Felipe Murgas**[14,15]

[1] *Planetary Sciences Group, Department of Physics, University of Central Florida, Orlando, FL 32816-2385*

[2] *Departamento de Astronoma, Universidad de Chile, Camino El Observatorio 1515, Las Condes, Santiago, Chile*

[3] *Centro de Astrofísica y Tecnologías Afines (CATA), Casilla 36-D, Santiago, Chile*

[4] *Instituto de Astrofísica de Andalucía (IAA, CSIC) Glrorieta de la Astronomía, s/n E-18008 Granada, Spain*

[5] *School of Physics and Astronomy, Queen Mary University of London, 327 Mile End Road, London E1 4NS, UK*

[6] *Institut für Astrophysik, Georg-August-Universität Göttingen Friedrich-Hund-Platz 1, 37077 Göttingen, Germany*

[7] *Department of Earth and Planetary Sciences, Weizmann Institue of Science, 234 Herzl Street, Rehovot 76100, Israel*

[8] *Institut de Ciéncies de l'Espai (ICE, CSIC), C/Can Magrans s/n, Campus UAB, 08193 Bellaterra, Spain*

[9] *Institut d'Estudis Espacials de Catalunya (IEEC), 08034 Barcelona, Spain*

[10] *Department of Astronomy, Columbia University, 550 W 120th Street, New York, NY 10027*

[11] *Department of Terrestrial Magnetism, Carnegie Institution of Washington, 5241 Broad Branch Road NW, Washington D.C. USA 20015-1305*

[12] *Department of Physics, Grinnell College, 1116 8th Ave., Grinnell, IA 50112, USA*

[13] *Department of Astronomy, University of Maryland, College Park, MD 20742, USA*

[14] *Instituto de Astrofísica de Canarias (IAC), E-38205 La Laguna, Tenerife, Spain*

[15] *Departamenta de Astrofísica, Universidad de La Laguna (ULL), E-38206 La Laguna, Tenerife, Spain*

In preparation for submission to *The Planetary Science Journal*.

2.1 Abstract

We observed Proxima Centauri with the *Spitzer Space Telescope* InfraRed Array Camera (IRAC) five times in 2016 and 2017 to search for transits of Proxima Centauri b. Following standard analysis procedures, we found three asymmetric transit-like events that are now understood to be vibrational systematics. This systematic is correlated with the width of the point-response function (PRF), which we measure with rotated and non-rotated Gaussian fits. We show that the systematic can be removed with a novel application of an adaptive elliptical-aperture photometry technique, and compare the performance of this technique with fixed and variable, circular-aperture photometry, using both BiLinearly Interpolated Subpixel Sensitivity (BLISS) maps and non-binned Pixel-Level Decorrelation (PLD). With BLISS maps, elliptical photometry results in a lower standard deviation of normalized residuals, and reduced or similar correlated noise when compared to circular apertures. PLD prefers variable, circular apertures, but generally results in more correlated noise than BLISS. This vibrational effect is likely present in other *Spitzer* observations, where correction could improve results, as well as other telescopes. Our elliptical apertures can be applied to any photometry observations, and may be even more effective when applied to more circular PRFs than *Spitzer's*.

2.2 Introduction

Exoplanet science has pushed the *Spitzer Space Telescope* (Werner et al. 2004) far beyond its initial design. Transiting and eclipsing exoplanet signals are on the order of 1% and 0.1% of their host star, respectively, far below expected performance of the InfraRed Array Camera (IRAC, Fazio et al. 2004). Soon, the *James Webb Space Telescope* (JWST) will provide an unprecedented combination of spectral resolution, spectral reach, collecting area, and stability for exoplanet science

(Deming & Seager 2017). The field will move from rough 1D characterization of the hottest giant exoplanets (e.g., Stevenson et al. 2017, Kreidberg et al. 2018) to 3D mapping of many hot Jupiters (de Wit et al. 2012, Majeau et al. 2012), starting with the Early Release Science targets (ERS, Bean et al. 2018). Small and cold planets will still be a challenge. Hotter terrestrial targets, like TRAPPIST-1b (Gillon et al. 2016, 2017), will require $\sim$10 eclipses for a confident detection (Morley et al. 2017), but temperate Earth-like targets will be difficult, if not impossible (Rauer et al. 2011, Rugheimer et al. 2015, Batalha et al. 2018, Beichman & Greene 2018). We must take advantage of every technique available if we hope to characterize these planets.

Spitzer IRAC suffers from two primary systematic effects: an easily-removed "ramp" that causes measured flux to vary with time, and an intrapixel gain variation that creates correlations between flux and target position on the detector at a subpixel level (e.g., Charbonneau et al. 2005). These effects are present in all 3.6 and 4.5 μm observations, although the ramp is sometimes weak enough to be ignored. Several independent modeling techniques, such as BiLinearly Interpolated Subpixel Sensitivity (BLISS, Stevenson et al. 2012), Pixel-Level Decorrelation (PLD, Deming et al. 2015), and Independent Component Analysis (Morello 2015), have successfully removed the position-correlated noise, enabling transiting exoplanet observations with uncertainties <100 ppm and retrieving accurate planetary parameters (Ingalls et al. 2016).

A third, much less common effect creates light-curve features that resemble transiting exoplanets. This effect has been linked to activity in the "noise pixel" parameter (Lewis et al. 2013), a measurement of the number of pixels that contribute to centering and photometry, or the size of the point-response function (PRF). Spikes in the noise pixels are known to correlate with transit-like signals, and are likely caused by high-frequency telescope oscillations of unknown origin (see irachpp.spitzer.caltech.edu/page/np_spikes).

We observed Proxima Centauri (hereafter Proxima) in 2016 and 2017 with *Spitzer* IRAC to search for transits of the planet Proxima b (Anglada-Escudé et al. 2016). Jenkins et al. (2019), hereafter J19, presented the results from the first observation. When following standard data reduction procedures, these observations contain three transit-like events (see Figure 2.1) that resemble the asymmetric shapes created by transits of disintegrating planets (e.g., Rappaport et al. 2014, Sanchis-Ojeda et al. 2015, Vanderburg et al. 2015) or comets (e.g., Rappaport et al. 2018). We now know, conclusively, that these events are localized systematic effects due to high-frequency telescopic vibration. When the telescope vibrates, the PRF smears along the direction of the vibration. During the vibration, fixed-radius photometry apertures spill light, resulting in lower measured flux with larger vibrational amplitudes.

In this work, we present evidence that the systematic is due to vibration, several new methods to identify when this vibrational systematic occurs, and a new aperture photometry method to correct it. The paper is organized as follows: in Section 2.3 we describe our observations, in Section 2.6 we discuss how to identify this systematic, in Section 2.7 we present our elliptical photometry method, in Section 2.8 we interpret our findings, and in Section 2.9 we lay out our conclusions.

2.3 Observations

Table 2.1: Observations

	Nov. 2016	May 2017	June 2017	July 2017	Nov. 2017
Wavelength (μm)	4.5	4.5	3.6	3.6	4.5
Obs. Start (MBJD[a])	7707.01325	7898.72171	7932.29024	7943.47907	8087.38757
Obs. Duration (hours)	48.04	7.07	7.34	7.34	12.52
Frame Time (s)	0.02	0.02	0.02	0.02	0.02

[a]MBJD = Modified Barycentric Julian Date = BJD - 2450000.
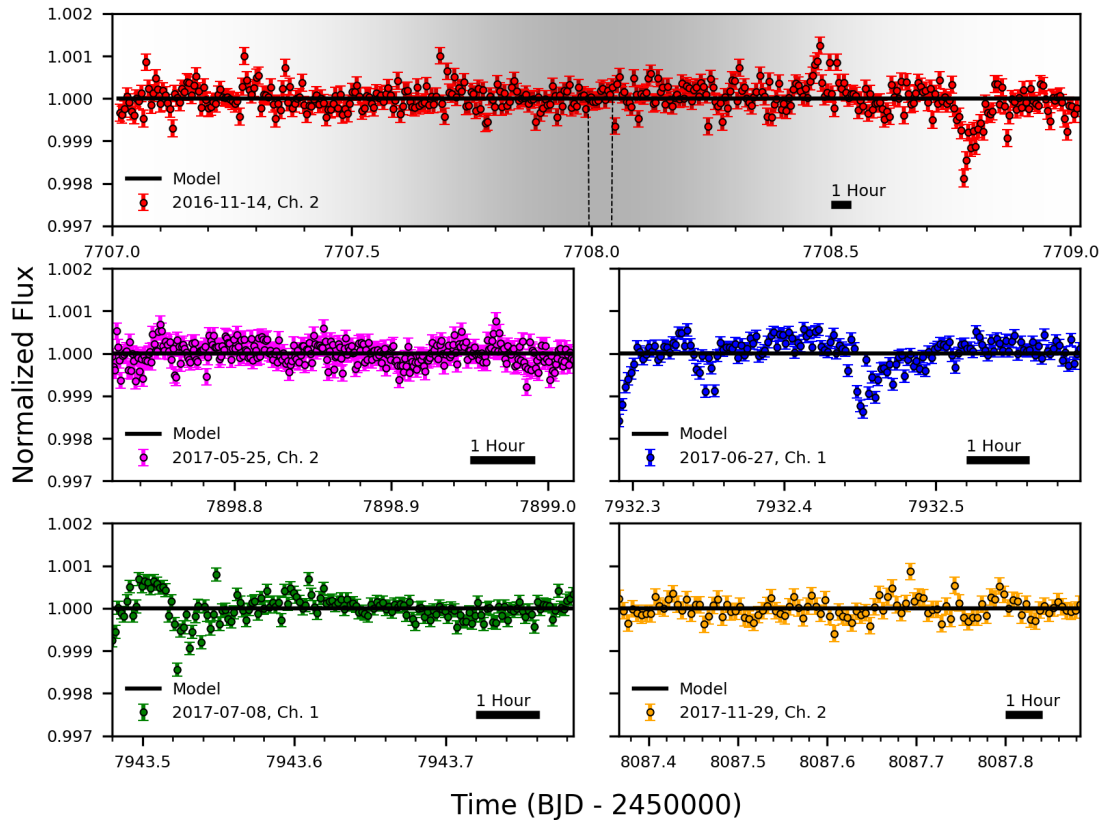
Figure 2.1: The five *Spitzer* IRAC observations of Proxima, using fixed circular apertures and a BLISS map, binned to 1500 frames per data point. We divided out the BLISS map and ramp model where appropriate, so ideally the resulting light curve should be flat (matching the black model line). Observation dates and channels appear on each plot. The dashed line in the top panel marks the nominal Proxima b transit and the shaded region denotes the uncertainty on transit time (at the time of observation).

We observed Proxima with the *Spitzer* InfraRed Array Camera, with both the 3.6 and 4.5 μm filters, for a total of > 80 hours (Table 2.1). The 48-hour stare bracketed the predicted transit time of Proxima b, and shorter observations occurred at times when further transits should occur, if the feature in the stare was caused by Proxima b (Anglada-Escudé et al. 2016). All observations were in 32×32 subarray mode and centered on the IRAC "sweet spot", at (-0.352″, 0.064″) and (-0.511′, 0.039″) for 3.6 μm and 4.5 μm, respectively. We bracketed each science observation with an initial 30-minute observation to minimize telescope pointing settling and a final 10-minute observation, for those who wish to generate their own dark frames, per *Spitzer* Science Center recommendations.

Notably, due to the brightness of the target, our observations utilized the shortest frame time, 0.02 seconds, which allows temporal resolution of high-frequency effects. To handle the large data volume from this cadence, our observations have data gaps. The 48 hour 4.5 μm stare has 17-second gaps between 64-frame subarray chunks, 24 second gaps between Astronomical Observation Requests (AORs), and ~ 4 minute gaps every 16 hours for data downlink and target reacquisition. Both 3.6 μm observations have 6-second gaps between subarray chunks and 14-second gaps between AORs. The shortest 4.5 μm observation has $2 - 2.5$-second gaps between subarray chunks, and only one AOR. The November 2017 observation has the same gaps as the 48-hour stare, without the downlink and target reacquisition.

The telescope's heater, which introduces motion on the detector in ~ 40-minute cycles, was turned off for the duration of all five observations, following then-current *Spitzer* procedures for exoplanet observations. This minimizes the impact of the intrapixel systematic, allowing closer study of other effects.

2.4 Centering and Photometry

We use our Photometry for Orbits, Eclipses, and Transits code (POET, e.g. Stevenson et al. 2012, Blecic et al. 2013, Cubillos et al. 2013, Blecic et al. 2014, Cubillos et al. 2014, Hardy et al. 2017) for all analyses herein. The steps in producing light curves are bad pixel identification, determining the location of the target (centering), and measuring its brightness (photometry). This work relies heavily on different centering and photometry methods, so we describe our implementations in detail.

2.4.1 Centering Methods

We apply four centering methods: Gaussian fitting, rotated-Gaussian fitting, center-of-light, and least asymmetry (Lust et al. 2014). Our Gaussian fitting includes parameters for x and y position, widths in both dimensions, a height, and a constant background level. Center-of-light calculates an average position, weighted by the brightness of each pixel, much like a center-of-mass calculation. Least asymmetry computes an asymmetry value for each pixel by considering the symmetry of surrounding flux values and then fitting an inverted Gaussian to determine the point of least asymmetry. Our rotated-Gaussian fitting is described further in Section 2.6. Unless stated otherwise, we perform centering on a 17×17 pixel box around the target. Least asymmetry uses a 9×9 pixel box to calculate the asymmetry of a given pixel in the 17×17 centering box.

2.4.2 Photometry Methods

Since the IRAC point-spread function (PSF) is undersampled, we bilinearly interpolate all images to $5\times$ resolution, ensuring that flux is conserved. We then perform aperture photometry on the interpolated images, increasing all relevant length scales by the interpolation factor (aperture radius, background annulus radii, etc.), so the apertures include subpixels. We calculate the background level as a mean of the pixels in a $7-15$-pixel annulus around the centering position.

We use three aperture photometry methods: fixed, variable (Lewis et al. 2013), and elliptical (see Section 2.7). Fixed photometry uses a constant-size aperture throughout a given observation. We use apertures with a fixed radius from $1.5-4.5$ pixels, in steps of 0.25 pixels. Variable photometry derives aperture radii from the same 17×17 pixel box used for centering, as described by Lewis et al. (2013). Our variable aperture radii are calculated as

$$R_{\mathrm{var}} = a\sqrt{N} + b \tag{2.1}$$

where a is a scaling factor from $0.5-1.5$ in steps of 0.25, b is an offset from $-1.0-2.0$ pixels in steps of 0.5, N is the noise-pixel parameter, defined as

$$N = \frac{\sum_i \left(I(i)^2\right)}{\left(\sum_i I(i)\right)^2}, \tag{2.2}$$

where $I(i)$ is the intensity at pixel i, considering all pixels within the centering aperture. $\sqrt{N}$ is ~ 2 pixels on average and varies by ~ 0.2 pixels throughout an observation. Calculation of N should be done after background subtraction, as this significantly reduces scatter in the aperture radii and noise in the light curve.

24

Elliptical apertures vary in size similarly to variable apertures, but use the 1σ widths of the Gaussian centering fit as the base, rather than $\sqrt{N}$. Then, the elliptical apertures are calculated as

$$R_{\text{ell},x} = a\sigma_x + b$$

$$R_{\text{ell},y} = a\sigma_y + b \qquad (2.3)$$

where σ_x and σ_y are the ellipse widths in x and y (which vary in time), a ranges from $3 - 7$ in steps of 1, and b again covers -1.0 – 2.0 pixels in steps of 0.5 pixels. The ellipse widths typically range from 0.5 – 0.6 pixels during an observation. See Section 2.7 for a more in-depth description of elliptical photometry.

We use small apertures to avoid additional noise from background pixels, but they necessitate an aperture correction to account for lost light. With fixed apertures, we rescale the final photometry based on the fraction of the interpolated PSF in the aperture. For variable and elliptical photometry, we rescale on the same principle, using an average aperture size and shape. It is possible to rescale the photometry using time-variable apertures, but this negates the correction made by the photometry methods. The interpolated PSF, provided by the *Spitzer* Science Center, is constant, but we suspect the true PSF stretches on short timescales, making accurate rescaling on a frame-by-frame basis impossible (see Section 2.7 for further discussion). Regardless, we are interested in the relative photometry, not the absolute, so whether or not we scale by a constant factor has little bearing on this work.

We choose the best centering and photometry methods by minimizing the binned-σ χ^2 (hereafter χ^2_{bin}; Deming et al. 2015) of a best-fit light-curve model. In brief, this metric searches for model residuals that behave like white noise. White noise, measured by the standard deviation of normalized residuals (SDNR), predictably scales as $1/\sqrt{n}$, where n is the number of items in each bin. Therefore, we fit a line with a slope of $-1/2$ to log(SDNR) *vs.* log(bin size) anchored to the log(SDNR) of the unbinned residuals ($n = 1$), where the χ^2 of this fit is the χ^2_{bin}. We repeat this process for every light curve produced by each unique combination of centering and photometry methods, and take the best fit (lowest χ^2_{bin}) as optimal. See Deming et al. 2015 and Appendix A for a complete description of the calculation.

2.5   Light-curve Modeling

We modeled our light curves with both PLD and BLISS to correct the intrapixel systematic and to assess each model's ability to address the vibrational systematic. BLISS maps correct for intrapixel sensitivity variations by gridding the detector into fine subpixels. We assign each frame to a subpixel based on the target position from centering, compute the sensitivity of each subpixel based on the average flux of all frames associated with them, once all other models (astrophysical or otherwise) have been removed, and bilinearly interpolate the sensitivity grid to find a correction factor for each frame. The generic full model formula is

$$F(x, y, t) = F_s A(t) M(x, y) R(t), \tag{2.4}$$

where x and y are the target positions in each frame, t is time, A is the astrophysical model, M is the BLISS map, and R is the time-dependent ramp. In a typical transiting exoplanet analysis, $A(t)$ would be a combination of transits, eclipses, and phase curve variation models, but in this case, there are no modeled astrophysical variations.

PLD removes the same effect by treating the data as a weighted sum of normalized pixel values, where the weights are free parameters of the model. The model is

$$F(t) = F_s \left(\sum_{j}^{n_p} c_j \hat{P}_j + A(t) + R(t) \right), \tag{2.5}$$

where n_p is the number of pixels considered, c_j are pixel weights, and $\hat{P}_j$ are time-dependent normalized pixel values. See Stevenson et al. (2012) and Deming et al. (2015) for in-depth descriptions of BLISS and PLD, respectively.

Figure 2.1 shows the fixed-aperture light curves, modeled with BLISS, to highlight the vibrational systematic. The systematic is present in the November 2016, June 2017, and July 2017 light curves, so we focus on these observations going forward.

2.6   Systematics Diagnostics

Past works used the noise pixel measurement (Equation 2.2) to identify activity in the PRF, and correct for it with variable-aperture photometry (e.g., Lewis et al. 2013, Deming et al. 2015, Garhart et al. 2018, Jenkins et al. 2019). Effectively, noise pixels measure the number of pixels above the background (contributing to centering and photometry). A wider (narrower) PRF should result in a larger (smaller) noise-pixel value. Since noise pixels measure an area, the radius of the photometry aperture required for the PRF is the root of the noise pixels, commonly with additional multiplicative and/or additive scaling (see Section 2.4.2). Thus, as the PRF size varies throughout the observation, so does the photometry aperture radius.

J19 found that, using common techniques, centering and photometry selection criteria selected against variable photometry apertures. We have improved the variable-aperture photometry by calculating the aperture radii after background subtraction, which reduces uncertainty introduced by unimportant pixels. With this improvement, variable-aperture radii are preferred over fixed-aperture radii, although they still introduce noise to the light curve.

Oscillations in the telescope, if higher frequency than the exposure time, could be hidden from centering, but they would be evident in a widening of the PRF in the direction of the vibration. By fitting a Gaussian to the PRF, we determine 1σ widths in x and y (see Figure 2.2, second and third rows) and notice a prominent widening in the PRF at the time of the systematic. This widening is even more evident in a measure of the 3σ area of the Gaussian, which we compute as an ellipse with axes along the x and y directions (see Figure 2.2, fourth row). We also measure the variance in this elliptical area, on a 64-frame basis, to look for PRF activity (see Figure 2.2, fifth row).
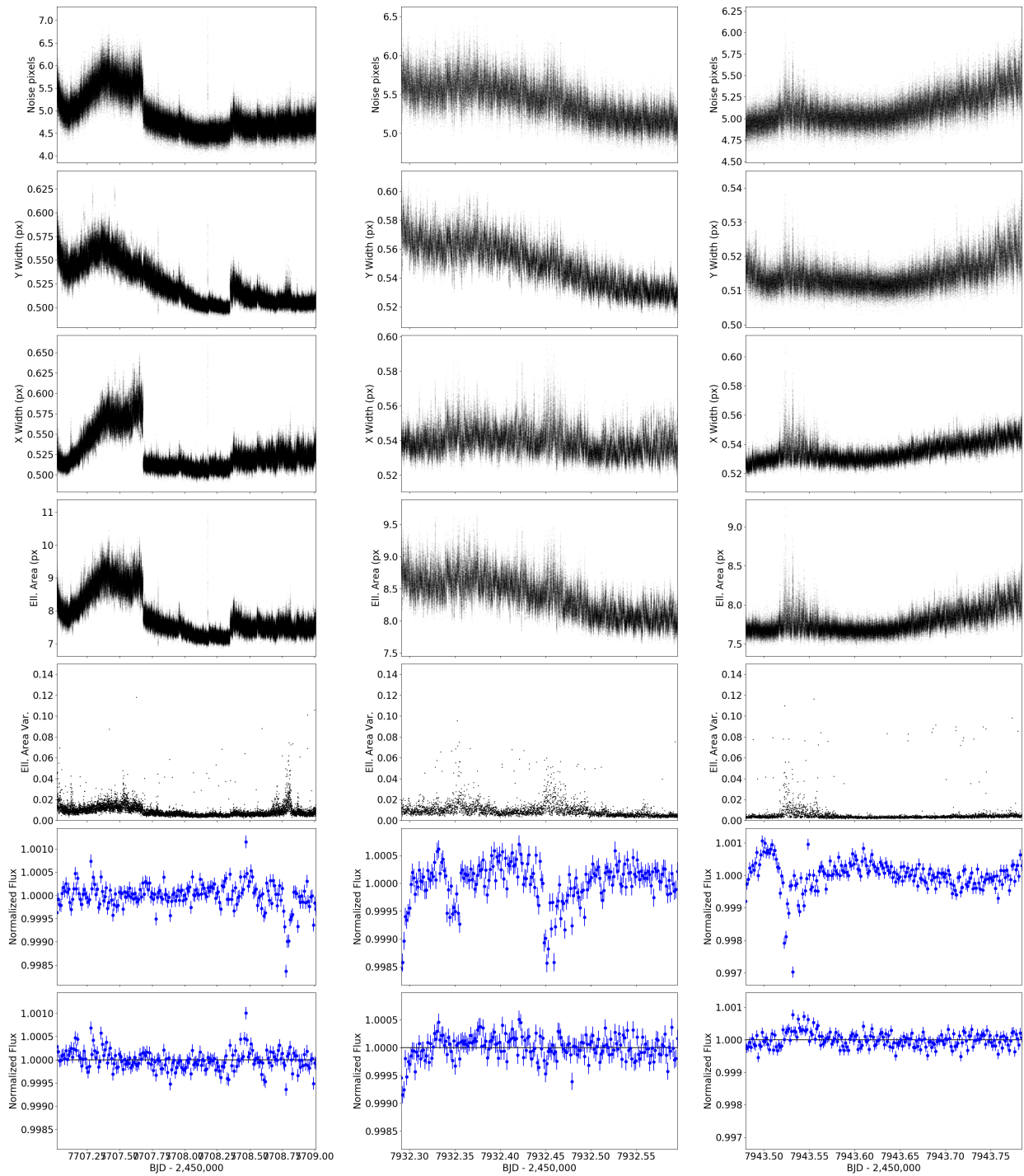
Figure 2.2: Systematic identification methods for the three observations that contain the systematic. Columns from left to right are the November 2016, June 2017, and July 2017 observations. From top to bottom, rows are noise pixels, PRF y width, PRF x width, elliptical area, elliptical area variance, the best fixed-aperture light curve, and the best elliptical-aperture light curve.
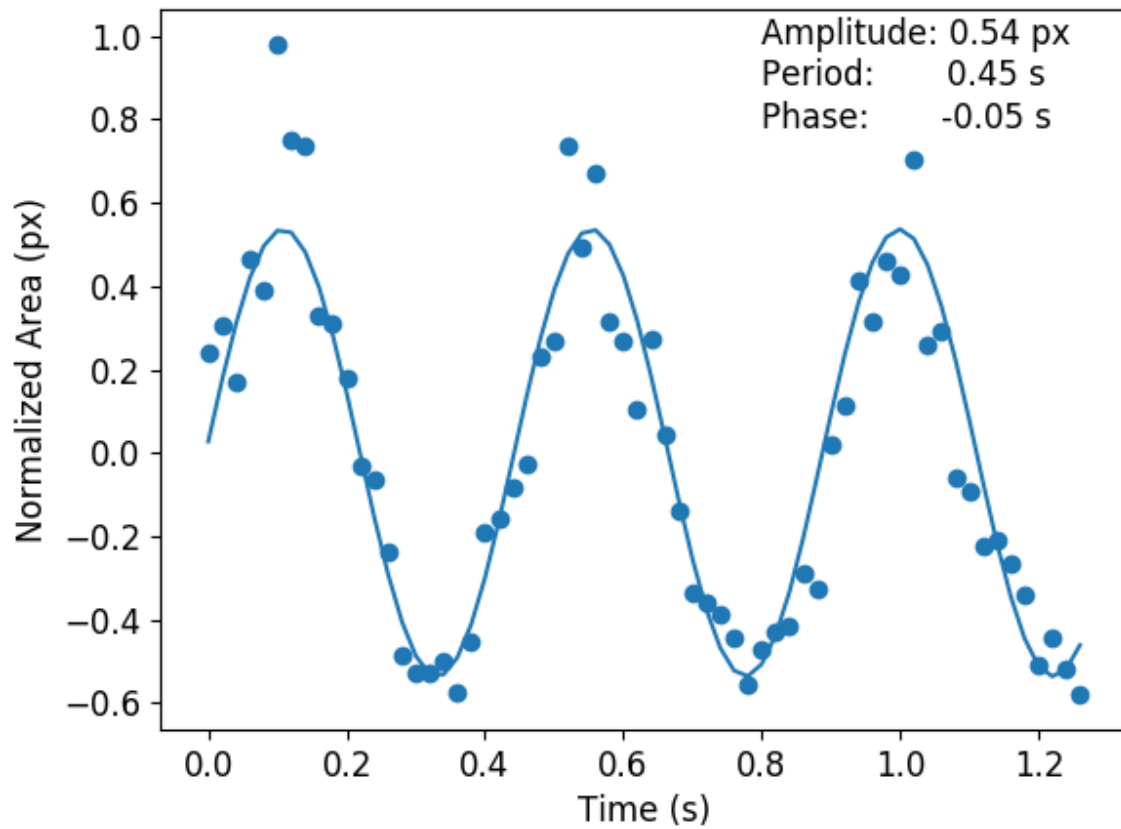
Figure 2.3: Mean-subtracted Gaussian elliptical area of a single chunk of 64 frames during the peak of the systematic in the July 2017 observation. We fit a simple sinusoid and determined a 0.45 second periodicity.

Our short exposures (0.02 seconds) allow temporal resolution of high-frequency effects. Figure 2.3 shows the 3σ elliptical area of a single set of 64 frames during the peak of the systematic in the July 2017 observation. We find a clear sinusoidal pattern with a period of 0.45 seconds, evidence for telescope oscillation.

The periodicity is localized in time, so we apply a continuous Morlet wavelet transform, using the `pywavelets` (Lee et al. 2019) Python package (see Figure 2.4). Wavelet transforms assume a uniform sampling, but our observations are sets of 64 short-cadence frames separated by relatively long gaps, to work around data storage limits. This results in spurious periodicity in the wavelet transforms. Despite this limitation, a wavelet transform reveals periodic activity in the elliptical area of the PRF at the time that the systematic occurred.

Lomb-Scargle periodograms are well-suited to finding periodicity in non-uniformly sampled data, but unlike wavelet transforms, they provide no temporal resolution of localized activity (see Figure 2.5). The periodogram shows a strong peak at ~ 2 Hz (as well as several weaker resonances), which matches the periodic behavior seen in Figure 2.3.
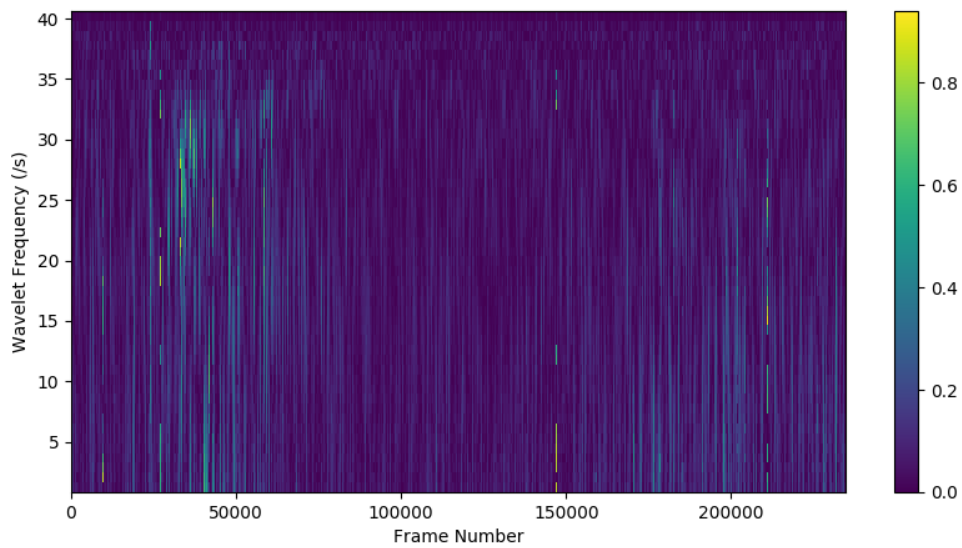
Figure 2.4: Continuous Morlet wavelet transform of the Gaussian elliptical area of the July 2017 Proxima observation using a fixed 2.5-pixel aperture radius and non-rotated Gaussian centering. The high-frequency activity near frame 40,000 indicates periodic behavior corresponding with the systematic. The top and bottom 0.1% amplitudes have been masked out for visual clarity. This transform assumes the frames are evenly distributed in time, but the observations were taken in 64-frame chunks with relatively large separations.
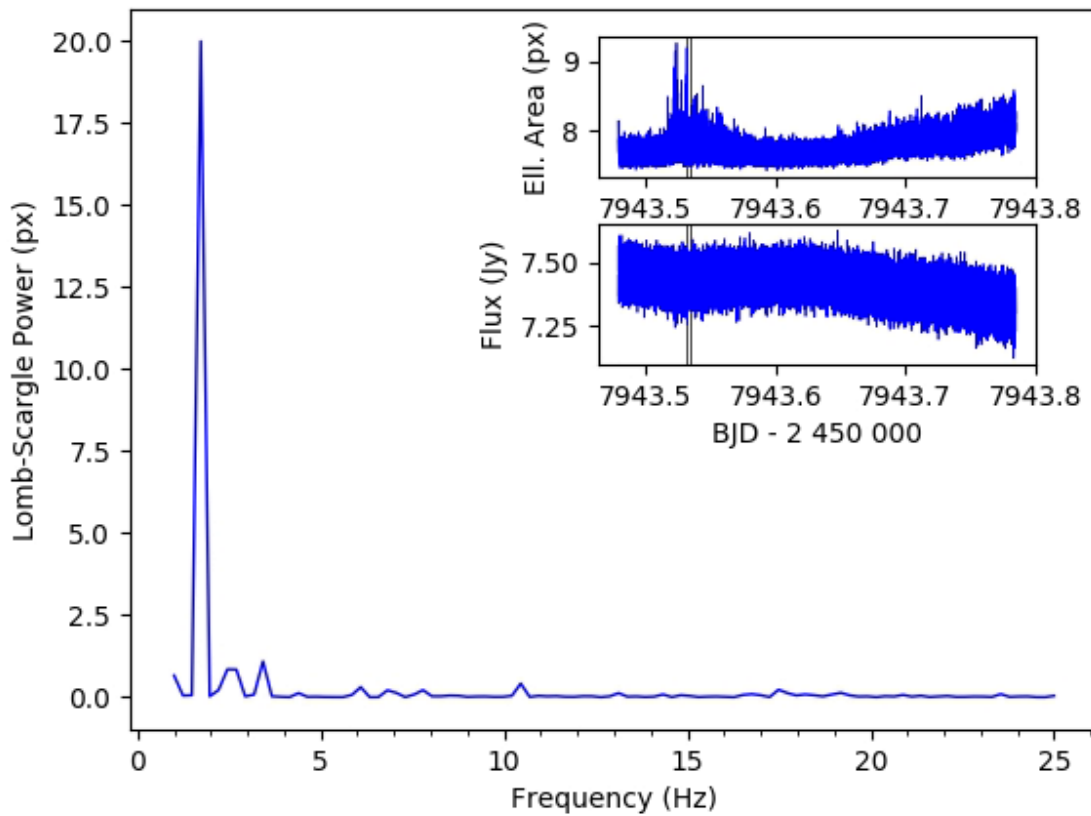
Figure 2.5: Windowed Lomb-Scargle periodogram of the elliptical area of the PRF during the July 2017 observation. The insets show the elliptical area of the PRF and flux vs. time, with vertical black lines bracketing the five minute window used in the periodogram. The peak in power at ~ 2 Hz, near the 0.45 second periodicity, appears during the systematic. Videos of this plot, using a sliding window, are available in the compendium.

Until now, we calculated elliptical area from the x and y widths of the PRF. However, this measure of area is only accurate if vibrations are oriented along those axes. To more accurately measure the shape of the PRF, we rotate a Gaussian clockwise from the x axis. This detaches the x and y widths from their respective axes, instead measuring the semimajor and semiminor axes of the ellipse. A rotated 2D Gaussian is described by

$$
\begin{aligned}
G(x, y, \sigma_x, \sigma_y, \theta, H) = H\exp(\,-\, & g_1(x - x_0)^2 \\
& + 2g_2(x - x_0)(y - y_0) \\
& + g_3(y - y_0)^2) \\
& + C,
\end{aligned}
\tag{2.6}
$$

where

$$
\begin{aligned}
g_1 &= \frac{\cos^2 \theta}{2\sigma_x^2} + \frac{\sin^2 \theta}{2\sigma_y^2}, \\
g_2 &= -\frac{\sin^2 2\theta}{4\sigma_x^2} + \frac{\sin^2 2\theta}{4\sigma_y^2}, \\
g_3 &= \frac{\sin^2 \theta}{2\sigma_x^2} + \frac{\cos^2 \theta}{2\sigma_y^2},
\end{aligned}
$$
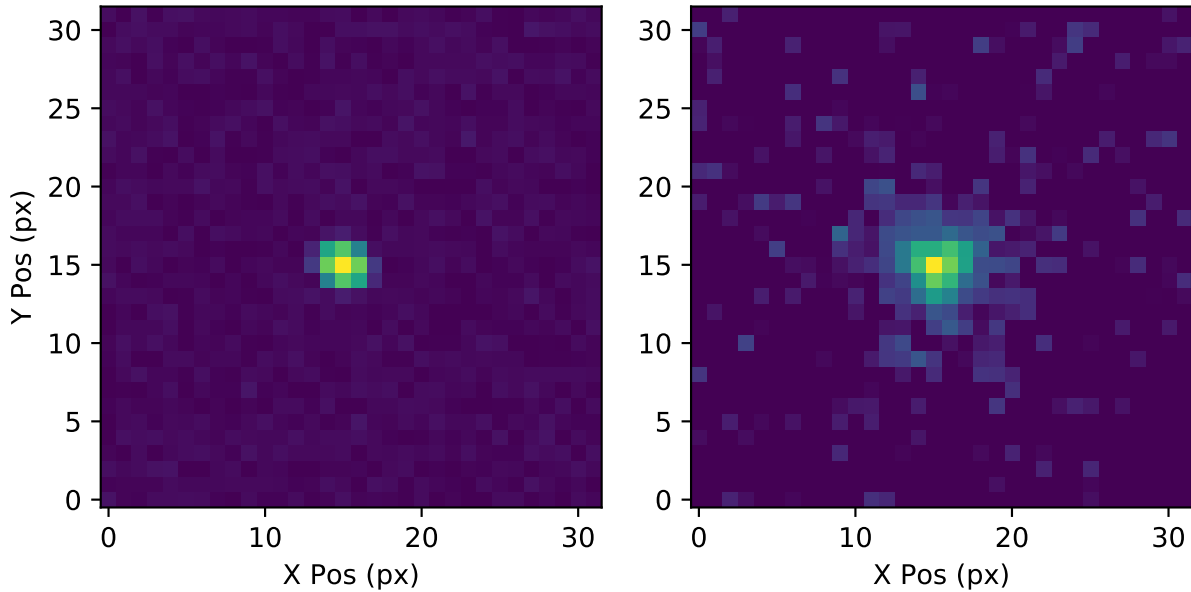
Figure 2.6: Log-scaled test images for the rotated, elliptical Gaussian centering. **Left:** A synthetic image computed from Equation 2.6 with Poisson noise. **Right:** A real *Spitzer* image of Proxima from AOR 63273472.

H is the height of the Gaussian, θ is the angle of rotation clockwise from the x axis, x_0 is the x position of the peak, y_0 is the y position of the peak, σ_x is the width along θ, σ_y is the width along $\theta + 90°$, and C is a constant background level. We fit to all seven parameters to determine the orientation and shape of the PRF. We tested this algorithm on both a synthetic rotated, elliptical Gaussian and an image from our observations (see Figure 2.6). The results are listed in Table 2.2. The difference in retrieved star position is small but differences in the measured PRF widths are more significant.

Table 2.2: Rotated Gaussian Tests

Method	σ_x	σ_y	x_0	y_0	H	θ	Background
Synthetic Image							
Truth	0.600	0.500	15.000	15.000	87000	$\pi/6$ (0.524)	100.0
Std. Gaussian	0.570	0.521	15.004	15.000	87135	—	101.2
Rot. Gaussian	0.599	0.499	15.004	15.000	87187	0.526	100.2
Spitzer Image from AOR 63273472							
Std. Gaussian	0.568	0.527	15.107	14.892	82175	—	32.7
Rot. Gaussian	0.585	0.502	15.103	14.883	84120	0.508	32.9

We applied this rotated-Gaussian centering method to the observations affected by the systematic. The results are displayed in the first seven rows of Figure 2.7. They match the non-rotated Gaussian fits in elliptical area and elliptical area variance. These systematic identification methods perform nearly equivalently when using the non-rotated Gaussian. However, the rotated Gaussian has implications for elliptical photometry, which is discussed in Section 2.7.

There are bimodalities in the fitted y position, the axes lengths, and rotation of the ellipse when the center of the PRF passes below the center of a pixel. This behavior may be due to the asymmetry of the IRAC PRF, which has a roughly-triangular shape (e.g., the second panel of Figure 2.6). The ellipse is swapping between the asymmetric edges of the triangle (Figure 2.8). We see this behavior in the Proxima images and the synthetic images created with IRACSIM for the *Spitzer* data challenge (Ingalls et al. 2016), but not with simple synthetic Gaussians (Figure 2.6), suggesting it is a real effect of the complex PRF.
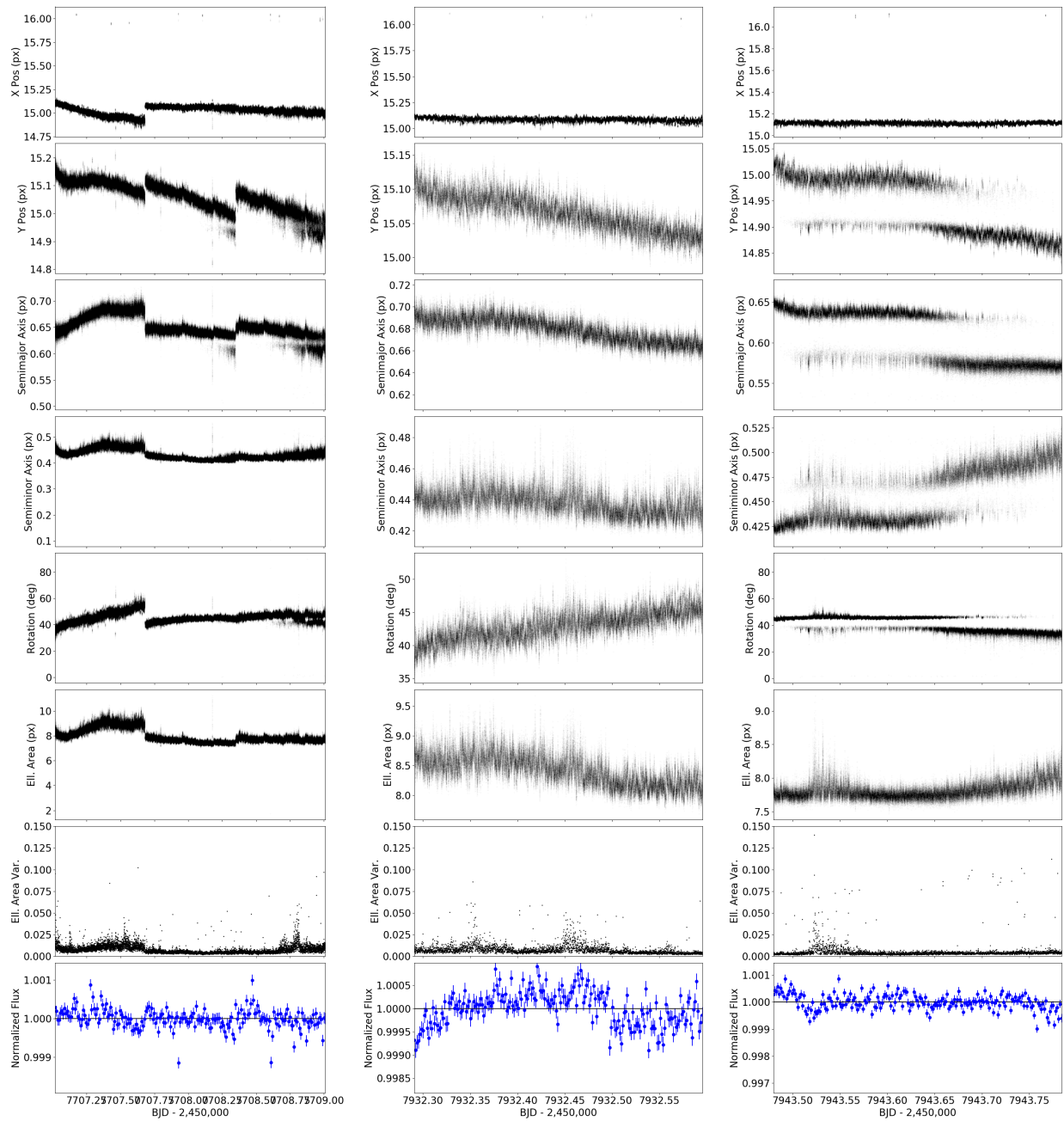
Figure 2.7: Results of rotated elliptical centering and photometry. Columns from left to right are the November 2016, June 2017, and July 2017 observations. From top to bottom, rows are x position, y position, semimajor axis, semiminor axis, rotation, elliptical area, elliptical area variance, and the light curve.

37
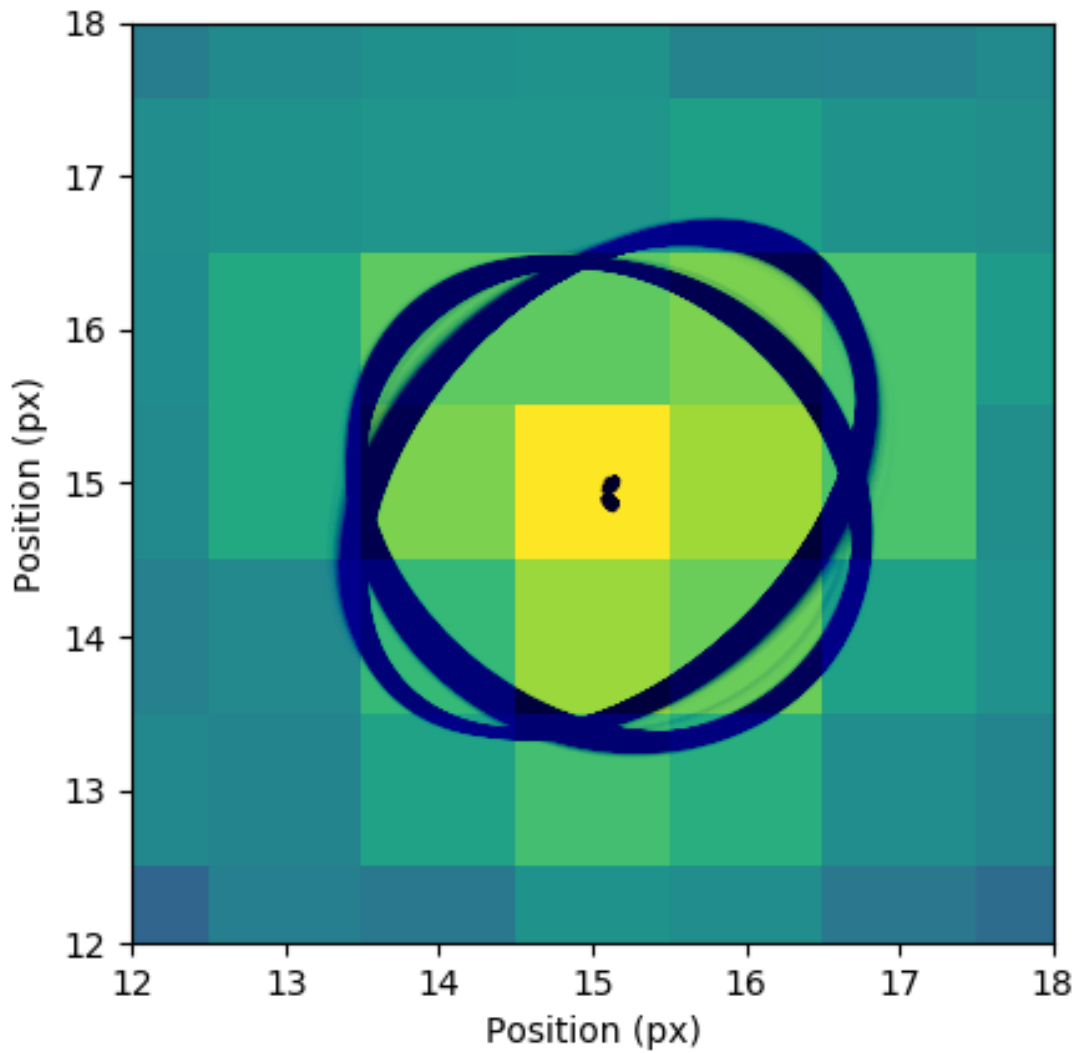
Figure 2.8: All 3σ rotated elliptical apertures for the July 2017 observation and their centers, overlaid on a log-scaled *Spitzer* image from the same observation. The ellipses toggle between two rotational modes corresponding with the bimodal distribution in centering position.

2.7 Systematic Removal through Elliptical Photometry

Past works have removed this vibrational systematic prior to modeling with variable, circular apertures (e.g., Lewis et al. 2013, Deming et al. 2015, Garhart et al. 2018, Jenkins et al. 2019). These apertures attempt to adjust to avoid spilling light. However, due to their circular shape, they must either spill flux from the aperture or overcompensate in size for the elliptically-smeared PRF to capture all the important pixels; thus, they include unnecessary background noise.

Instead we use elliptical photometry, where we use an elliptical aperture described by the fitted parameters from the non-rotated Gaussian or rotated Gaussian centering methods described in Section 2.6. With rotated Gaussian centering, we apply the rotation to the elliptical aperture. Similar to using variable-aperture photometry, elliptical apertures attempt to remove the effects of PRF activity prior to modeling, but only including the most important pixels, resulting in less noise. Several elliptical photometry packages exist (e.g., Laher et al. 2012, Barbary 2016, Merlin et al. 2019), although application has been limited to correcting atmospheric effects in ground-based observations (Bowman & Holdsworth 2019), measuring the radial surface brightness profiles of physically elliptical galaxies (e.g., Davis et al. 1985, Djorgovski 1985, Cornell 1989, Ryder 1992, McNamara & O'Connell 1992, Hayes et al. 2005), and measuring photometry of comets that move significantly during each exposure (Miles 2009). To our knowledge, none have used elliptical apertures to correct for vibrational effects.

Qualitatively, we find that elliptical photometry almost entirely removes the vibrational systematic from the light curve, with the non-rotated ellipses outperforming the rotated ones (see Figures 2.2 and 2.7, last rows). To assess performance quantitatively, we fit BLISS and PLD models to the three observations which include the vibrational systematic. PLD performs poorly when applied to observations longer than typical eclipses and transits (Deming et al. 2015), so for the 48-hour observation, we only consider the final 16 hours (after the final data downlink). Many PLD

implementations also bin the data (e.g., Deming et al. 2015, Wong et al. 2015, Buhler et al. 2016), which can reduce short-period correlated noise. We choose not to bin to isolate each model's ability to address correlated noise. Table 2.3 lists the results: $\chi^2_{\mathrm{b}in}$-minimized photometry aperture sizes for each combination of centering and photometry methods, as well as the $\chi^2_{\mathrm{b}in}$ (lowest in bold) and SDNR for each combination, both for BLISS and PLD fits.

Table 2.3: Optimal Photometry Methods

Photometry	Centering	Ap. Size[a] (pixels)	$\chi^2_{\mathrm{b}in}$	SDNR (ppm)
November 2016				
BLISS (last 16 hours of observation)				
Fixed	Gaus.	3.00	21.8	7630
	L. Asym.	3.00	22.1	7641
	C. of L.	4.00	293.2	8758
Variable	Gaus.	0.50+1.0	7.7	7583
	L. Asym.	0.50+1.0	9.0	7475
	C. of L.	1.50+0.5	200.3	8324
Elliptical	Gaus.	4.00+0.5	**5.1**	7438
	Rot. Gaus.	3.00+1.0	5.1	7727
PLD (last 16 hours of observation)				
Fixed	Gaus.	3.50	62.1	8173
	L. Asym.	3.25	61.2	7909
	C. of L.	3.50	61.4	8169
Variable	Gaus.	0.75+2.0	**34.7**	8506
	L. Asym.	0.75+2.0	37.0	8509
	C. of L.	0.75+1.5	35.6	7932
Elliptical	Gaus.	3.00+2.0	42.5	8216
	Rot. Gaus.	5.00+1.5	60.3	8858
June 2017				
BLISS				
Fixed	Gaus.	3.25	58.8	5511
	L. Asym.	3.75	124.3	5778
	C. of L.	4.50	1440.0	6642
Variable	Gaus.	0.75+0.5	12.5	5632
	L. Asym.	1.00+0.0	21.0	5657
	C. of L.	0.50+0.5	150.0	6627
Elliptical	Gaus.	4.00+0.0	**3.1**	5295

Photometry	Centering	Ap. Size[a] (pixels)	χ^2_{bin}	SDNR (ppm)
	Rot. Gaus.	3.00+0.0	7.7	5808
PLD				
Fixed	Gaus.	3.00	74.2	5375
	L. Asym.	2.75	76.4	5286
	C. of L.	3.25	73.2	5490
Variable	Gaus.	0.75+1.0	36.6	5417
	L. Asym.	0.75+0.5	33.6	5503
	C. of L.	0.75+0.5	**28.8**	5375
Elliptical	Gaus.	5.00-0.5	29.3	5232
	Rot. Gaus.	6.00-0.5	31.3	5332
July 2017				
BLISS				
Fixed	Gaus.	4.50	87.8	5926
	L. Asym.	4.50	30.0	5889
	C. of L.	4.50	1175.9	6295
Variable	Gaus.	1.50-0.5	2.6	5585
	L. Asym.	1.00+0.5	**2.5**	5437
	C. of L.	0.50+0.0	45.3	8682
Elliptical	Gaus.	7.00-1.0	4.9	5229
	Rot. Gaus.	5.00+0.0	23.7	5225
PLD				
Fixed	Gaus.	4.00	159.0	5763
	L. Asym.	4.00	159.3	5754
	C. of L.	4.50	161.9	5982
Variable	Gaus.	1.50-0.5	55.3	5582
	L. Asym.	1.00+0.5	56.9	5443
	C. of L.	0.75+0.5	**36.9**	5577
Elliptical	Gaus.	7.00-1.0	71.1	5223
	Rot. Gaus.	7.00+0.5	93.2	5803

[a] Aperture sizes for variable and elliptical photometry are listed as $a + b$ (see Equations 2.1 and 2.3)

2.8 Discussion

We draw several conclusions from the results in Table 2.3. First, we find elliptical photometry superior or equivalent to variable, circular apertures when using BLISS maps. The vibrational systematic is not correlated with position, especially if the vibration occurs at a period shorter than the exposure time, and thus cannot be corrected by a BLISS map. By removing the vibrational systematic with elliptical photometry, the accuracy of the BLISS map improves for the entire observation.

The PLD model is more flexible in its noise removal. It assumes that flux variations are tied to fluctuations in the pixel brightnesses. As the target moves on the detector, pixels brighten and dim. Likewise, if the PRF is smeared, pixels near the center of the target dim and pixels along the vibration axis brighten. Thus, the PLD model is able to correct for the vibrational systematic without explicit knowledge of the vibration, minimizing the advantage gained by using elliptical photometry. This is convenient, but we achieve much lower correlated noise in the BLISS models where the systematics are corrected with a physical description of their effects (see χ^2_{bin} values in Table 2.3). We do not use binning in our application of PLD, which would reduce correlated noise, but again without explicit knowledge of the vibration.

The rotated ellipse is never preferred over the non-rotated case. As mentioned above, the *Spitzer* PRF is highly asymmetric, and slightly triangular in shape (see Figure 2.6, right panel), which creates a challenge when fitting a rotated ellipse. The vibration-induced elliptical shape is less prominent than the already-present asymmetry in the PRF, as evidenced by the bimodal distribution in rotation (Figure 2.7). We suspect the rotated elliptical Gaussian is fitting to the sides of the triangular PRF, which creates additional noise in the resulting light curve. Rotated elliptical photometry may be useful for other telescopes that have more circular PRFs.

Since the *Spitzer* PRF is a complex shape, ideally we would determine flux by directly fitting the PRF, but that has proven challenging. The *Spitzer* PRF is underresolved, especially at shorter wavelengths, and the true PSF is not known at a high resolution, only as a map of a point source at a 5×5 grid of positions within a central pixel. Hence, we recommend overresolved PRFs for high-precision point-source instruments like exoplanet telescopes, or a high-resolution lab-measured PRF tested in comparison to real data with a routine to accurately bin to the native pixel level. One could also fit a shape more representative of the PRF, like a tri-lobed Gaussian with a radial scale, rotation, stretching factor, and stretching axis. However, that is beyond the scope of this work.

In general, we find that PLD is agnostic to the centering method used. In two observations, we prefer center-of-light centering, and in the third there is no strong preference for any of the methods. This would suggest that, when using PLD models, it is acceptable to only apply center-of-light centering, although we recommend always applying all methods available.

BLISS maps, on the other hand, are extremely sensitive to the centering method because 1) target position is an input to the model, and 2) we use BLISS map x and y grid sizes equal to the RMS of the point-to-point x and y target position motion, respectively. Thus, higher precision centering methods result in maps with finer structure. Compared to Gaussian and least-asymmetry centering, center-of-light centering results in high RMS of point-to-point x and y target position motion and, thus, poor maps, at least for 3.6 and 4.5 µm observations (Table 2.3). Therefore, center-of-light can be ignored with BLISS maps, although applying all analysis methods will ensure the best is chosen.

Finally, in nearly all cases, non-rotated elliptical photometry results in the lowest SDNR. With BLISS, elliptical photometry improves SDNR by up to 11.2% over fixed, circular apertures and up to 6.0% over variable, circular apertures. With PLD, we see up to 9.4% improvement over fixed apertures and up to 6.3% improvement over variable apertures. These statistics are for the entire modeled light curve; the improvement is even more pronounced if we only consider data when the systematic is present.

The optimal light curves presented here are available, in machine- and human-readable formats, in a compendium archive available at `https://doi.org/10.5281/zenodo.3759914`. The compendium also includes best-fit models and correlated noise diagnostics.

2.9   Results

We have identified a vibrational systematic in *Spitzer* photometry that mimics planetary or cometary transits. With our short exposure times, we were able to resolve this vibration in the size and shape of the PRF, both on sub-second timescales and with periodograms. We caution against false positive detections of planets, and recommend applying the techniques described here to identify and correct the systematic.

"Noise pixels" can occasionally identify this systematic, but they can be misleading, as noise pixel activity does not always correspond with the systematic, and can frequently be hidden in the baseline activity. Several other metrics are better suited to identifying this vibration:

1. x and y widths from Gaussian centering, both rotated and non-rotated.

2. Elliptical area of Gaussian centering, both rotated and non-rotated.

3. Variance of noise pixels.

4. Variance of elliptical area.

5. Wavelet amplitude over a variety of frequencies.

6. Lomb-Scargle periodograms of elliptical area.

For our observations, variance of the PRF area most accurately identifies the systematic. However, in most IRAC time-series observations, identification of this systematic is more challenging, as the pointing wander induced by temperature fluctuation in the telescope reduces the clarity of our diagnostics.

To correct this vibrational systematic, we developed an adaptive elliptical-photometry technique. We fit an asymmetric Gaussian to the PRF to determine target position and PRF shape, and use this parameterization to create an elliptical aperture that adapts its shape to the PRF as it changes with time. We applied elliptical photometry to three observations known to include the vibrational systematic, with both BLISS and PLD models to assess relative performance. With BLISS models, elliptical photometry results in reduced correlated noise in two of our three observations, and reduced SDNR in all observations. PLD prefers variable, circular apertures over elliptical apertures, but, without binning, is less capable of removing correlated noise compared to BLISS. We also used a rotated elliptical aperture, but found that the complex shape of the *Spitzer* PRF created bimodalities in the orientation of the ellipse and noise in the resulting light curve. Other shapes, like a tri-lobed Gaussian, are an area of potential future study.

We cannot determine the source of the vibration, though we speculate that it could be micrometeorite impacts or wear-and-tear on the telescope, such as a defect in the gyroscopes. If the source is micrometeorites, this systematic should be present in many past observations, at roughly the same rate as in our observations (four instances in 80 hours). Reanalyses with our techniques may be able to rescue data sets deemed unsalvageable, or at least improve the uncertainties on measured

planetary transmission, emission, and phase curve variation. If wear-and-tear is the source of the systematic, then older observations may be unaffected, but more recent observations would still be affected. *Spitzer* produced high-profile exoplanet science for 16 years (e.g., Gillon et al. 2017, Kreidberg et al. 2019), much of which is done at the limit of detection. Elliptical photometry could make the difference between speculation and discovery.

Elliptical photometry is not limited to *Spitzer*. *TESS* and *Kepler* (and K2) are purely photometric observatories that may suffer from the same systematic. JWST also has photometric modes which will surely be used to push transiting exoplanet photometry to the smallest and coldest objects possible. Optimistically assuming that we reach the noise floor, we will need large amounts of JWST time to study these planets (e.g., Morley et al. 2017), and require the absolute best data reduction and noise removal techniques.

2.10   Acknowledgments

2.11   List of References

Anglada-Escudé, G., Amado, P. J., Barnes, J., Berdiñas, Z. M., Butler, R. P., Coleman, G. A. L., de La Cueva, I., Dreizler, S., Endl, M., Giesers, B., Jeffers, S. V., Jenkins, J. S., Jones, H. R. A., Kiraga, M., Kürster, M., López-González, M. J., Marvin, C. J., Morales, N., Morin, J., Nelson, R. P., Ortiz, J. L., Ofir, A., Paardekooper, S.-J., Reiners, A., Rodríguez, E., Rodríguez-López, C., Sarmiento, L. F., Strachan, J. P., Tsapras, Y., Tuomi, M., & Zechmeister, M. 2016, Nature, 536, 437

Barbary, K. 2016, The Journal of Open Source Software, 1, 58

Batalha, N. E., Lewis, N. K., Line, M. R., Valenti, J., & Stevenson, K. 2018, ApJ, 856, L34

Bean, J. L., Stevenson, K. B., Batalha, N. M., Berta-Thompson, Z., Kreidberg, L., Crouzet, N., Benneke, B., Line, M. R., Sing, D. K., Wakeford, H. R., Knutson, H. A., Kempton, E. M.-R., Désert, J.-M., Crossfield, I., Batalha, N. E., de Wit, J., Parmentier, V., Harrington, J., Moses, J. I., Lopez-Morales, M., Alam, M. K., Blecic, J., Bruno, G., Carter, A. L., Chapman, J. W., Decin, L., Dragomir, D., Evans, T. M., Fortney, J. J., Fraine, J. D., Gao, P., García Muñoz, A., Gibson, N. P., Goyal, J. M., Heng, K., Hu, R., Kendrew, S., Kilpatrick, B. M., Krick, J., Lagage, P.-O., Lendl, M., Louden, T., Madhusudhan, N., Mandell, A. M., Mansfield, M., May, E. M., Morello, G., Morley, C. V., Nikolov, N., Redfield, S., Roberts, J. E., Schlawin, E., Spake, J. J., Todorov, K. O., Tsiaras, A., Venot, O., Waalkes, W. C., Wheatley, P. J., Zellem, R. T.,

Angerhausen, D., Barrado, D., Carone, L., Casewell, S. L., Cubillos, P. E., Damiano, M., de Val-Borro, M., Drummond, B., Edwards, B., Endl, M., Espinoza, N., France, K., Gizis, J. E., Greene, T. P., Henning, T. K., Hong, Y., Ingalls, J. G., Iro, N., Irwin, P. G. J., Kataria, T., Lahuis, F., Leconte, J., Lillo-Box, J., Lines, S., Lothringer, J. D., Mancini, L., Marchis, F., Mayne, N., Palle, E., Rauscher, E., Roudier, G., Shkolnik, E. L., Southworth, J., Swain, M. R., Taylor, J., Teske, J., Tinetti, G., Tremblin, P., Tucker, G. S., van Boekel, R., Waldmann, I. P., Weaver, I. C., & Zingales, T. 2018, PASP, 130, 114402

Beichman, C. A. & Greene, T. P. Observing Exoplanets with the James Webb Space Telescope (Springer International Publishing), 85

Blecic, J., Harrington, J., Madhusudhan, N., Stevenson, K. B., Hardy, R. A., Cubillos, P. E., Hardin, M., Bowman, O., Nymeyer, S., Anderson, D. R., Hellier, C., Smith, A. M. S., & Collier Cameron, A. 2014, ApJ, 781, 116

Blecic, J., Harrington, J., Madhusudhan, N., Stevenson, K. B., Hardy, R. A., Cubillos, P. E., Hardin, M., Campo, C. J., Bowman, W. C., Nymeyer, S., Loredo, T. J., Anderson, D. R., & Maxted, P. F. L. 2013, ApJ, 779, 5

Bowman, D. M. & Holdsworth, D. L. 2019, A&A, 629, A21

Buhler, P. B., Knutson, H. A., Batygin, K., Fulton, B. J., Fortney, J. J., Burrows, A., & Wong, I. 2016, ApJ, 821, 26

Charbonneau, D., Allen, L. E., Megeath, S. T., Torres, G., Alonso, R., Brown, T. M., Gilliland, R. L., Latham, D. W., Mandushev, G., O'Donovan, F. T., & Sozzetti, A. 2005, ApJ, 626, 523

Cornell, M. E. 1989, PhD thesis, Arizona Univ., Tucson.

Cubillos, P., Harrington, J., Madhusudhan, N., Foster, A. S. D., Lust, N. B., Hardy, R. A., & Bowman, M. O. 2014, ApJ, 797, 42

Cubillos, P., Harrington, J., Madhusudhan, N., Stevenson, K. B., Hardy, R. A., Blecic, J., Anderson, D. R., Hardin, M., & Campo, C. J. 2013, ApJ, 768, 42

Davis, L. E., Cawson, M., Davies, R. L., & Illingworth, G. 1985, AJ, 90, 169

de Wit, J., Gillon, M., Demory, B. O., & Seager, S. 2012, A&A, 548, A128

Deming, D., Knutson, H., Kammer, J., Fulton, B. J., Ingalls, J., Carey, S., Burrows, A., Fortney, J. J., Todorov, K., Agol, E., Cowan, N., Desert, J.-M., Fraine, J., Langton, J., Morley, C., & Showman, A. P. 2015, ApJ, 805, 132

Deming, L. D. & Seager, S. 2017, Journal of Geophysical Research (Planets), 122, 53

Djorgovski, S. B. 1985, PhD thesis, California Univ., Berkeley.

Fazio, G. G., Hora, J. L., Allen, L. E., Ashby, M. L. N., Barmby, P., Deutsch, L. K., Huang, J.-S., Kleiner, S., Marengo, M., Megeath, S. T., Melnick, G. J., Pahre, M. A., Patten, B. M., Polizotti, J., Smith, H. A., Taylor, R. S., Wang, Z., Willner, S. P., Hoffmann, W. F., Pipher, J. L., Forrest, W. J., McMurty, C. W., McCreight, C. R., McKelvey, M. E., McMurray, R. E., Koch, D. G., Moseley, S. H., Arendt, R. G., Mentzell, J. E., Marx, C. T., Losch, P., Mayman, P., Eichhorn, W., Krebs, D., Jhabvala, M., Gezari, D. Y., Fixsen, D. J., Flores, J., Shakoorzadeh, K., Jungo, R., Hakun, C., Workman, L., Karpati, G., Kichak, R., Whitley, R., Mann, S., Tollestrup, E. V., Eisenhardt, P., Stern, D., Gorjian, V., Bhattacharya, B., Carey, S., Nelson, B. O., Glaccum, W. J., Lacy, M., Lowrance, P. J., Laine, S., Reach, W. T., Stauffer, J. A., Surace, J. A., Wilson, G., Wright, E. L., Hoffman, A., Domingo, G., & Cohen, M. 2004, ApJS, 154, 10

Garhart, E., Deming, D., Mandell, A., Knutson, H., & Fortney, J. J. 2018, A&A, 610, A55

Gillon, M., Jehin, E., Lederer, S. M., Delrez, L., de Wit, J., Burdanov, A., Van Grootel, V., Burgasser, A. J., Triaud, A. H. M. J., Opitom, C., Demory, B.-O., Sahu, D. K., Bardalez Gagliuffi, D., Magain, P., & Queloz, D. 2016, Nature, 533, 221

49

Gillon, M., Triaud, A. H. M. J., Demory, B.-O., Jehin, E., Agol, E., Deck, K. M., Lederer, S. M., de Wit, J., Burdanov, A., Ingalls, J. G., Bolmont, E., Leconte, J., Raymond, S. N., Selsis, F., Turbet, M., Barkaoui, K., Burgasser, A., Burleigh, M. R., Carey, S. J., Chaushev, A., Copperwheat, C. M., Delrez, L., Fernandes, C. S., Holdsworth, D. L., Kotze, E. J., Van Grootel, V., Almleaky, Y., Benkhaldoun, Z., Magain, P., & Queloz, D. 2017, Nature, 542, 456

Hardy, R. A., Harrington, J., Hardin, M. R., Madhusudhan, N., Loredo, T. J., Challener, R. C., Foster, A. S. D., Cubillos, P. E., & Blecic, J. 2017, ApJ, 836, 143

Hayes, M., Östlin, G., Mas-Hesse, J. M., Kunth, D., Leitherer, C., & Petrosian, A. 2005, A&A, 438, 71

Ingalls, J. G., Krick, J. E., Carey, S. J., Stauffer, J. R., Lowrance, P. J., Grillmair, C. J., Buzasi, D., Deming, D., Diamond-Lowe, H., Evans, T. M., Morello, G., Stevenson, K. B., Wong, I., Capak, P., Glaccum, W., Laine, S., Surace, J., & Storrie-Lombardi, L. 2016, AJ, 152, 44

Jenkins, J. S., Harrington, J., Challener, R. C., Kurtovic, N. T., Ramirez, R., Peña, J., McIntyre, K. J., Himes, M. D., Rodríguez, E., Anglada-Escudé, G., Dreizler, S., Ofir, A., Peña Rojas, P. A., Ribas, I., Rojo, P., Kipping, D., Butler, R. P., Amado, P. J., Rodríguez-López, C., Kempton, E. M.-R., Palle, E., & Murgas, F. 2019, arXiv e-prints

Kreidberg, L., Koll, D. D. B., Morley, C., Hu, R., Schaefer, L., Deming, D., Stevenson, K. B., Dittmann, J., Vanderburg, A., Berardo, D., Guo, X., Stassun, K., Crossfield, I., Charbonneau, D., Latham, D. W., Loeb, A., Ricker, G., Seager, S., & Vand erspek, R. 2019, Nature

Kreidberg, L., Line, M. R., Thorngren, D., Morley, C. V., & Stevenson, K. B. 2018, ApJ, 858, L6

Laher, R. R., Gorjian, V., Rebull, L. M., Masci, F. J., Fowler, J. W., Helou, G., Kulkarni, S. R., & Law, N. M. 2012, PASP, 124, 737

Lee, G. R., Gommers, R., Wasilewski, F., Wohlfahrt, K., & O'Leary, A. 2019, J. Open Source Soft., 4, 1237

Lewis, N. K., Knutson, H. A., Showman, A. P., Cowan, N. B., Laughlin, G., Burrows, A., Deming, D., Crepp, J. R., Mighell, K. J., Agol, E., Bakos, G. Á., Charbonneau, D., Désert, J.-M., Fischer, D. A., Fortney, J. J., Hartman, J. D., Hinkley, S., Howard, A. W., Johnson, J. A., Kao, M., Langton, J., & Marcy, G. W. 2013, ApJ, 766, 95

Lust, N. B., Britt, D., Harrington, J., Nymeyer, S., Stevenson, K. B., Ross, E. L., Bowman, W., & Fraine, J. 2014, PASP, 126, 1092

Majeau, C., Agol, E., & Cowan, N. B. 2012, ApJ, 747, L20

McNamara, B. R. & O'Connell, R. W. 1992, ApJ, 393, 579

Merlin, E., Pilo, S., Fontana, A., Castellano, M., Paris, D., Roscani, V., Santini, P., & Torelli, M. 2019, A&A, 622, A169

Miles, R. 2009, Society for Astronomical Sciences Annual Symposium, 28, 51

Morello, G. 2015, ApJ, 808, 56

Morley, C. V., Kreidberg, L., Rustamkulov, Z., Robinson, T., & Fortney, J. J. 2017, The Astrophysical Journal, 850, 121

Rappaport, S., Barclay, T., DeVore, J., Rowe, J., Sanchis-Ojeda, R., & Still, M. 2014, The Astrophysical Journal, 784, 40

Rappaport, S., Vanderburg, A., Jacobs, T., LaCourse, D., Jenkins, J., Kraus, A., Rizzuto, A., Latham, D. W., Bieryla, A., & Lazarevic, M. 2018, MNRAS, 474, 1453

Rauer, H., Gebauer, S., Paris, P. V., Cabrera, J., Godolt, M., Grenfell, J. L., Belu, A., Selsis, F., Hedelt, P., & Schreier, F. 2011, A&A, 529, A8

Rugheimer, S., Kaltenegger, L., Segura, A., Linsky, J., & Mohanty, S. 2015, ApJ, 809, 57

Ryder, S. 1992, Australian Journal of Physics, 45, 395

Sanchis-Ojeda, R., Rappaport, S., Pallè, E., Delrez, L., DeVore, J., Gandolfi, D., Fukui, A., Ribas, I., Stassun, K. G., Albrecht, S., Dai, F., Gaidos, E., Gillon, M., Hirano, T., Holman, M., Howard, A. W., Isaacson, H., Jehin, E., Kuzuhara, M., Mann, A. W., Marcy, G. W., Miles-Páez, P. A., Montañés-Rodríguez, P., Murgas, F., Narita, N., Nowak, G., Onitsuka, M., Paegert, M., Van Eylen, V., Winn, J. N., & Yu, L. 2015, The Astrophysical Journal, 812, 112

Stevenson, K. B., Harrington, J., Fortney, J. J., Loredo, T. J., Hardy, R. A., Nymeyer, S., Bowman, W. C., Cubillos, P., Bowman, M. O., & Hardin, M. 2012, ApJ, 754, 136

Stevenson, K. B., Line, M. R., Bean, J. L., Désert, J.-M., Fortney, J. J., Showman, A. P., Kataria, T., Kreidberg, L., & Feng, Y. K. 2017, AJ, 153, 68

Vanderburg, A., Johnson, J. A., Rappaport, S., Bieryla, A., Irwin, J., Lewis, J. A., Kipping, D., Brown, W. R., Dufour, P., Ciardi, D. R., Angus, R., Schaefer, L., Latham, D. W., Charbonneau, D., Beichman, C., Eastman, J., McCrady, N., Wittenmyer, R. A., & Wright, J. T. 2015, Nature, 526, 546

Werner, M. W., Roellig, T. L., Low, F. J., Rieke, G. H., Rieke, M., Hoffmann, W. F., Young, E., Houck, J. R., Brandl, B., Fazio, G. G., Hora, J. L., Gehrz, R. D., Helou, G., Soifer, B. T., Stauffer, J., Keene, J., Eisenhardt, P., Gallagher, D., Gautier, T. N., Irace, W., Lawrence, C. R., Simmons, L., Van Cleve, J. E., Jura, M., Wright, E. L., & Cruikshank, D. P. 2004, ApJS, 154, 1

Wong, I., Knutson, H. A., Lewis, N. K., Kataria, T., Burrows, A., Fortney, J. J., Schwartz, J., Agol, E., Cowan, N. B., Deming, D., Désert, J.-M., Fulton, B. J., Howard, A. W., Langton, J., Laughlin, G., Showman, A. P., & Todorov, K. 2015, ApJ, 811, 122

CHAPTER 3: BLISS VS. PLD: APPLICATION TO WASP-29b ECLIPSES

Ryan C. Challener[1]**, Joseph Harrington**[1]**, Patricio E. Cubillos**[1,2]**, Jasmina Blecic**[1,3]**, Drake Deming**[4]**, and Coel Hellier**[5]

[1] *Planetary Sciences Group, Department of Physics, University of Central Florida, Orlando, FL 32816-2385*
[2] *Space Research Institute, Austrian Academy of Sciences, Graz, Austria*
[3] *New York University Abu Dhabi, Abu Dhabi, United Arab Emirates*
[4] *University of Maryland, College Park, MD*
[5] *Astrophysics Group, Keele University, Staffordshire ST5 5BG, UK*

3.1 Abstract

We present an analysis of four low-signal *Spitzer* secondary-eclipse observations of the Saturn-sized exoplanet WASP-29b. We measured eclipse depths and midpoints using two methods within our Photometry for Orbits, Eclipses, and Transits (POET) code. The first is BiLinearly Interpolated Subpixel Sensitivity (BLISS) mapping, and the second is our new Zen Eliminates Noise (ZEN) module, which implements binned Pixel-Level Decorrelation (PLD). We also examine two methods for determining the optimal centering algorithm and photometry aperture size: minimum standard deviation of normalized residuals (SDNR, applies only to BLISS due to PLD's use of binning) and Deming's minimum χ^2_{bin}. We find that some of the presumed benefit of PLD actually derives from the improved ability of χ^2_{bin} to select against correlated noise. The resulting eclipse depths are inconsistent, with BLISS finding a deeper eclipse at 3.6 μm and a shallower eclipse at 4.5 μm. Using the eclipse timings, along with previous transit observations and radial-velocity data, we further refine the orbit of WASP-29b, and find an eccentricity between 0.021 and 0.035, depending on the decorrelation method. We also detect significant apsidal precession, although this requires an implausibly large perturbing companion. We performed atmospheric retrieval with our Bayesian Atmospheric Radiative Transfer (BART) code and find that the BLISS light curves demand a CO-dominated atmosphere, whereas the PLD eclipses are consistent with a non-inverted thermal structure, and molecular abundances cannot be constrained. Due to the unlikely physical scenarios suggested by the BLISS light curves, we cautiously prefer PLD, although poor data quality makes a methodology comparison challenging.

3.2   Introduction

The *Spitzer Space Telescope* (*Spitzer*, Werner et al. 2004) Infrared Array Camera (IRAC, Fazio et al. 2004) is the primary mid-infrared instrument for characterization of transiting exoplanets. IRAC photometry requires careful treatment of numerous systematic effects that are on-par or stronger than the signals of interest. Methods to address these systematics have evolved significantly since the first exoplanet observations (Charbonneau et al. 2002, Deming et al. 2005, Charbonneau et al. 2005), from simple polynomial positional sensitivity models to BiLinearly Interpolated Subpixel Sensitivity (BLISS, Stevenson et al. 2012) and Pixel-Level Decorrelation (PLD, Deming et al. 2015), to name a few. PLD and BLISS in particular are applied widely to *Spitzer* light curves, and PLD is now used to decorrelate *Kepler* data.

Some *Spitzer* exoplanet analyses use multiple decorrelation methods. Ingalls et al. (2016) assessed the accuracy of seven methods, both on real and simulated data, and found that three methods retrieved true eclipse depths within three times the photon limit: BLISS, PLD, and Independent Component Analysis (ICA, Morello et al. 2015). Kilpatrick et al. (2017) compared Pixel Variation Gain Maps (Ingalls et al. 2012), Nearest Neighbor (Lewis et al. 2013), and PLD, finding Nearest Neighbor and PLD in statistical agreement. Still, most analyses use just one of these many methods. In this work, we correct for the position-dependent systematic with both PLD and BLISS for four *Spitzer* IRAC observations of the exoplanet WASP-29b. The methods provide checks for each other, and inform us of confidence in the results.

The aforementioned tests of the decorrelation methods focus solely on modeling. We find that the centering and photometry methods used, which produce the light curves that are later modeled, can strongly impact the amount of correlated noise in the data, perhaps moreso than the choice of decorrelation method. To that end, we compare two different selection metrics for optimizing centering and photometry. The first is minimum standard deviation of normalized residuals (SDNR), which only applies to BLISS since PLD bins the data, and SDNR is implicitly dependent on the number of data points. The second is minimum binned-σ χ^2 (hereafter χ^2_{bin}), defined by Deming et al. (2015), which looks for a solution with uncorrelated residuals across all residual bin sizes.

Combining the modeling methods and optimization metrics, we have three cases: BLISS with minimum SDNR, BLISS with χ^2_{bin}, and PLD with χ^2_{bin}. We run orbital and atmospheric models and the retrieved parameters for all three cases, and address how the light-curve analysis methods impact the final results.

This paper is structured as follows: Section 3.3 lists the observations; Section 3.4 describes the light curve modeling techniques and results; Section 3.5 shows our orbital analyses, with discussion of the impact of methodology on the results; Section 3.6 presents the atmospheric analyses, with similar discussion; and Section 3.7 lays out our conclusions.

3.3   Observations

We analyzed data from four *Spitzer* IRAC visits to WASP-29 during planetary secondary eclipse: two observations in the 3.6 μm channel (Program 60003, PI Harrington; Program 70084, PI Harrington) and two in the 4.5 μm channel (Program 70084, PI Harrington; Program 10054, PI Knutson; see Table 3.1).

Table 3.1: Observation Information

Wavel. (μm)	Observation Date	Duration (hours)	Exp. time (seconds)
3.6	2010 Aug 27	8.79	0.4
3.6	2011 Jan 11	9.43	0.4
4.5	2011 Jan 27	9.43	0.4
4.5	2014 Aug 29	7.80	2.0

3.4 Data Analysis

We used our Photometry for Orbits, Eclipses, and Transits (POET) pipeline (Stevenson et al. 2010, Campo et al. 2011, Nymeyer et al. 2011, Stevenson et al. 2012, Cubillos et al. 2013) to analyze *Spitzer* Basic Calibrated Data (BCD). In brief, the POET pipeline removes bad pixels, finds the center of the target, performs interpolated aperture photometry, and fits a BLISS light-curve model (see Section 3.4.2).

We also used Zen Eliminates Noise (ZEN), our implementation of PLD, to fit a light-curve model to POET photometry (see Section 3.4.3). In Section 3.4.1 we describe the centering and photometry techniques common to POET and ZEN. Then, in Sections 3.4.4 - 3.4.7, we compare the light-curve modeling results of POET using BLISS and ZEN using PLD.

57

3.4.1 Centering and Photometry

We compared three centering methods: Gaussian fitting, center of light, and least-asymmetry Gaussian. Gaussian centering fits a Gaussian profile to the point spread function (PSF) and takes the location of the peak as the center of the target. Center-of-light centering weighs the location of each pixel by its brightness and calculates the center location, akin to a center-of-mass calculation. The least-asymmetry Gaussian method transforms each frame to asymmetry space and fits a Gaussian profile to the transformed image (Lust et al. 2014). We used a 16 pixel wide box for the Gaussian and center-of-light methods, and a 14 pixel wide box for the least-asymmetry method, with an 8 pixel wide box for the symmetry transformation.

POET performed flux-conserving interpolated aperture photometry with fixed-radius apertures, variable-radius apertures (Lewis et al. 2013), and elliptical apertures. The fixed-aperture radii range from 1.5 – 4.0 pixels in 0.25 pixel increments. Variable-aperture radii are defined by

$$R_{\mathrm{var}} = a\sqrt{N} + b, \tag{3.1}$$

where a ranges from 0.5 – 1.5 in increments of 0.25, b ranges from -1.0 – 2.0 in 0.5 pixel increments, and N is the "noise pixel" parameter (Lewis et al. 2013). Elliptical-aperture radii are described by

$$R_x = a\sigma_x + b,$$
$$R_y = a\sigma_y + b, \tag{3.2}$$

where σ_x and σ_y are the 1σ widths of a Gaussian fit to the star, a ranged from $3 - 7$ in steps of 1, and b again ranges from -1 – 2.0 in 0.5 pixel increments. Variable apertures can remove effects caused by variations in the size of the *Spitzer* PSF, but introduce white noise, increasing the standard deviation of the normalized residuals (SDNR) of light-curve models. Elliptical apertures also correct for variations but aim to keep apertures smaller to reduce noise.

When modeling with a subpixel map, previous works (Stevenson et al. 2010, Campo et al. 2011, Nymeyer et al. 2011, Stevenson et al. 2012, Cubillos et al. 2013, Blecic et al. 2013, Cubillos et al. 2014, Blecic et al. 2014, Hardy et al. 2017) used the SDNR to choose the optimal centering and photometry combinations. This minimizes white noise, and results in lower uncertainties on the eclipse depth, but does not account for correlated (red) noise. Thus, we also minimize the binned-σ χ^2 (hereafter χ^2_{bin}) described in Deming et al. (2015) to find the centering and photometry combination which results in the least red noise.

We use the same centering and photometry results as input to our PLD code, ZEN. Since PLD uses data binning, and binning naturally reduces the SDNR, we cannot also optimize with SDNR, as that would choose the largest bin size we allow. Thus, we also follow the methods of Deming et al. (2015), and use χ^2_{bin} to choose the best photometry, centering, and bin size combination (see Section 3.4.3). Table 3.2 lists the optimal centering and photometry methods for each case considered: SDNR-minimized BLISS, χ^2_{bin}-minimized BLISS, and χ^2_{bin}-minimized PLD.

Table 3.2: Centering and Photometry Parameters

Wavelength (µm)	Visit	Centering Method	Aper. Radius[a] (pixels)
BLISS, min. SDNR			
3.6	1	Gaussian	F2.25
3.6	2	Least-asymmetry	F2.25
4.5	1	Gaussian	F2.25
4.5	2	Least-asymmetry	F2.25
BLISS, min. χ^2_{bin}			
3.6	1	Gaussian	E6.00+1.00
3.6	2	Gaussian	E6.00-1.00
4.5	1	Gaussian	F2.00
4.5	2	Gaussian	E1.50+1.50[b]
PLD			
3.6	1	Center-of-light	V0.50+1.00
3.6	2	Gaussian	E7.00-1.00
4.5	1	Gaussian	V1.25+2.00
4.5	2	Gaussian	F1.75

[a]Letters indicate fixed (F), variable (V), or elliptical (E) photometry. Aperture radii for variable and elliptical photometry are listed as $a + b$ (see Equations 3.1 and 3.2).

[b]Due to high PSF variability in this observation, we allowed elliptical aperture scaling from 1.5 – 7.0 in 0.5 increments (a in Equation 3.2) and elliptical aperture offsets from -1.0 – 2.0 in 0.25 pixel increments (b in Equation 3.2).

3.4.2 Light-curve Modeling with BLISS

As mentioned above, the measured flux with IRAC can vary due to response variations at the subpixel level (Charbonneau et al. 2005). We included this systematic as a factor $M(x, y)$ on the system's flux. While the time-dependent ramp systematic, thought to be the result of charge trapping, is more prominent in the 8.0 μm band, it has also been observed in the 3.6 and 4.5 μm bands. We included this systematic as a factor $R(t)$ on the system's flux. With the eclipse function $E(t)$ (Mandel & Agol 2002), we modeled the light curve $F(x, y, t)$ as

$$F(x, y, t) = F_s M(x, y) R(t) E(t), \tag{3.3}$$

where F_s is the flux of the total system (star and exoplanet). The eclipse term is described by the eclipse depth, phase, duration, ingress time, and egress time. In all cases, eclipse phase is defined relative to the transit ephemeris reported by Hellier et al. (2010). Due to the low signal-to-noise ratio of these eclipses, we fixed the eclipse duration to 0.028 orbital phase and ingress/egress time to 0.00264 orbital phase, predicted values from the orbital fit in Hellier et al. (2010).

We used our Bi-Linearly Interpolated Subpixel Sensitivity (BLISS) mapping method to calculate $M(x, y)$ (Stevenson et al. 2012). BLISS assumes that, after dividing out the eclipse and ramp models, any remaining variation is due to sensitivity variations. We divide the pixels into bins with width and height equal to the root-mean-square (RMS) deviations of the x and y centering positions, respectively. The sensitivity of each bin is calculated from the mean sensitivity of the frames assigned to the bin. We discard any frames that do not fall into a bin with at least four total frames. The sensitivity of each frame is interpolated from this grid.

We model the ramp effect, $R(t)$, with one of the following models:

61

$$R(t) = 1 \tag{3.4}$$

$$R(t) = r_1(t - t_0) + r_0 \tag{3.5}$$

$$R(t) = r_2(t - t_0)^2 + r_1(t - t_0) + r_0 \tag{3.6}$$

where r_i are ramp parameters and t_0 is a phase offset. We fixed the constant offset r_0 to 1 and t_0 to 0.5, roughly corresponding to the middle of our datasets. Since the ramp function can vary in strength and shape over data sets, we tested every ramp function on each eclipse observation. We determined the best function by comparing the Bayesian Information Criterion (BIC, Schwarz 1978),

$$\text{BIC} = \chi^2 + k \ln N_{\text{data}}, \tag{3.7}$$

of the model for each ramp function, where k is the number of free parameters and N_{data} is the number of data points. Unlike SDNR, the BIC penalizes a model with additional free parameters, so we can compare ramp models with differing numbers of parameters. A lower BIC indicates a better fit, and the probability ratio of two models is given by

$$P_{21} = \exp\left(-\frac{\text{BIC}_2 - \text{BIC}_1}{2}\right), \tag{3.8}$$

where model 2 is a worse fit than model 1, following Raftery (1995). BIC comparison is done without uncertainty rescaling (described below) and without binning the data when using PLD (see Section 3.4.3).

62

We used a χ^2 minimizer to determine the best-fitting model parameters, and we rescale the photometry uncertainties such that reduced χ^2 is 1. To estimate parameter uncertainties, we used the Multi-Core Markov Chain Monte Carlo package (MC[3], Cubillos et al. 2017) to explore the parameter space, performing Bayesian posterior sampling. For these and all other Markov-chain Monte Carlo (MCMC) in this work, we require convergence of the Gelman-Rubin test within 1% of unity (Gelman & Rubin 1992). We also visually inspect trace plots, chain autocorrelations, parameter pair correlations, and posterior distributions for anomalous behavior. For all free parameters, we use non-informative (uniform) priors.

The results for all BLISS fits are summarized in Table 3.3.

Table 3.3: Light-curve Modeling Results

Wavelength (μm)	Visit	Depth (ppm)	Midpoint (phase)	Midpoint (BJD$_{TDB}$)	Temperature (K)
BLISS, min. SDNR					
3.6	1	957 ± 96	0.5133 ± 0.0007	$2455435.00729 \pm 0.00298$	1518 ± 61
3.6	2	648 ± 98	0.5150 ± 0.0008	$2455573.31308 \pm 0.00153$	1330 ± 68
4.5	1	105 ± 67	0.5055 ± 0.0102	$2455588.96315 \pm 0.04292$	645 ± 120
4.5	2	486 ± 96	0.5008 ± 0.0027	$2456899.13567 \pm 0.00967$	1018 ± 67
BLISS, min. χ^2_{bin}					
3.6	1	680 ± 124	0.5081 ± 0.0011	$2455435.98719 \pm 0.00390$	1349 ± 83
3.6	2	740 ± 102	0.5159 ± 0.0004	$2455573.31308 \pm 0.00255$	1389 ± 68
4.5	1	99 ± 68	0.5055 ± 0.0111	$2455588.96337 \pm 0.05115$	651 ± 119
4.5	2	393 ± 101	0.5007 ± 0.0023	$2456899.13518 \pm 0.00705$	951 ± 79
PLD					
3.6	1	532 ± 149	0.5125 ± 0.0026	$2455436.00427 \pm 0.00427$	1207 ± 127
3.6	2	533 ± 104	0.5148 ± 0.0010	$2455573.30863 \pm 0.00410$	1263 ± 77
4.5	1	533 ± 187	0.5055 ± 0.0037	$2455588.96317 \pm 0.01442$	1005 ± 151
4.5	2	701 ± 94	0.5007 ± 0.0005	$2456899.13509 \pm 0.00201$	1154 ± 56

3.4.3 Light-curve Modeling with PLD

PLD is a method to remove intrapixel effects without requiring precise subpixel centering (Deming et al. 2015). Here we describe the method in full, clarify the techniques introduced by Deming et al. (2015), and improve upon them.

We assume that the photometry S of the system (the flux) at any given time is a generalized function F of the sum of the pixel values at that same time. Then, applying a Taylor series expansion, the variations on photometry are given by Equation 2 of Deming et al. (2015),

$$\delta S^t = \sum_{i=1}^{n_p} \frac{\partial F}{\partial P_i^t} \delta P_i^t,$$

(3.9)

where P_i^t represents pixel i at time t.

To remove any real astrophysical effects, we normalize each pixel according to the sum of the pixels being considered at each time t (per frame), such that the eclipse is removed from the pixel values. Then the value of each pixel is given by Equation 3 of Deming et al. (2015),

$$\hat{P}_i^t = \frac{P_i^t}{\sum_{i=1}^{n_p} P_i^t},$$

(3.10)

where $\hat{P}$ is the normalized pixel value.

We model the eclipse $E(t)$ as an additive variation in these normalized pixel values, again following Mandel & Agol (2002). The ramp effect is included using the same functions as in BLISS but with $r_0 = 0$ since PLD is an additive model, and we find this parameter is degenerate with the other free parameters. We denote the Taylor series partial derivatives (see Equation 3.9) as c_i, such that the full PLD model is

$$S^t = \sum_{i=1}^{n_p} c_i \hat{P}_i^t + E(t) + R(t). \tag{3.11}$$

PLD depends heavily on binning in two ways: binning the residuals to quantify correlated noise and binning the data in time. Rather than using a simple SDNR or χ^2 minimization, we choose a "broad-bandwidth solution" (Deming et al. 2015, Wong et al. 2015, Buhler et al. 2016) following these steps:

1. Fit the model to the unbinned photometry via χ^2 minimization and calculate the SDNR of this model, which will be used later.

2. Bin the data. We try bin sizes of 1, 2, 4, 8, etc. points per bin up to 258, as per Deming et al. (2015).

3. For each bin size, use a minimization to determine best-fitting parameters.

4. Use the best-fitting parameters (fit to the *binned* data) to calculate the model and residuals on the *unbinned* data.

5. Bin these residuals at 2, 4, 8, 16, etc. points per bin, and calculate the SDNR at each bin size. This creates an evenly-separated distribution in log space, so that the following calculation is not biased toward short- or long-period correlated noise.

6. Calculate χ^2 of the logarithm of these SDNR *vs.* logarithm of the residuals bin sizes against a line of slope $-1/2$, anchored to the unbinned SDNR calculated in step 1, similar to RMS *vs.* bin size plots used in previous papers (e.g., Cubillos et al. 2014, Blecic et al. 2014, Hardy et al. 2017). Using the unbinned SDNR is crucial. If instead the SDNR from step 4 is used, the algorithm will prefer significantly larger bin sizes.

7. Choose the data bin size that results in the lowest χ^2 of the binned-σ relation.

We repeat these steps over all combinations of centering methods and photometry aperture sizes.

We use our implementation of the PLD algorithm, ZEN, to model the WASP-29b light curves. ZEN uses MC^3 (Multi-Core Markov Chain Monte Carlo, `https://github.com/pcubillos/MCcubed`, Cubillos et al. 2017) to explore parameter space and accurately determine parameter uncertainties. As with the BLISS models, we rescale photometry uncertainties such that reduced χ^2 is 1, and determine the best-fitting parameters with a χ^2 minimization.

We extensively tested ZEN against the original PLD code (Deming et al. 2015), written in IDL, to be certain our code behaved identically. As a test case, we compared the measured eclipse depth and optimal bin size of the WASP-14b data presented in Deming et al. (2015) and Blecic et al. (2013). We used matrix inversion for the light-curve fitting and used photometry from Deming et al. (2015) to limit testing to the PLD method itself. We reproduced the WASP-14b eclipse depth result at the 1 ppm level, well within ~ 100 ppm uncertainties.

The original PLD used a regression algorithm which is limited to fitting coefficients of time series, forcing one to determine all eclipse parameters except depth before fitting the light curve. We instead use the Trust Region Reflective χ^2 minimization algorithm which solves systems of equations with additional terms to prevent steps out of bounds (Branch et al. 1999). Thus, we both fit to all model parameters simultaneously and prevent nonphysical fits by enforcing boundary conditions.

In all of the following fits, we find that the h parameter, the constant offset, creates a degeneracy with the c_i parameters that prevents convergence, so we eliminate this term. We also fix the ingress and egress time of the eclipse model to 0.00264 orbital periods, and the eclipse width to 0.0280 orbital periods, the values predicted by orbital parameters in the literature (Hellier et al. 2010). We leave all c_i, eclipse midpoint, eclipse depth, linear ramp coefficient f, and quadratic ramp coefficient g as free parameters in the Markov Chain Monte Carlo (MCMC).

The results for all PLD fits are summarized in Table 3.3.

3.4.4   Channel 1, Visit 1

In the first visit at 3.6 µm, we discard the first 10,000 frames of the observation due to telescope settling ($\sim13.8\%$). We also find significant residual correlated noise, not corrected by our light curve models or our photometry techniques. It may be an unknown telescope systematic effect, or astrophysical, such as stellar activity. Since this effect occurs during the eclipse, we discard frames 30,086 – 34,047 (orbital phase 0.500 – 0.505) to avoid biasing our results. We also remove frames 64,305 – 64,335 for significant telescope motion, when *Spitzer* transferred angular momentum between its reaction wheels.

A BIC comparison (Equation 3.7) shows that a quadratic ramp function gives the best fit for all three modeling cases (Table 3.4). ZEN chooses a bin size of 256 frames. The light curves are shown in Figure 3.1. The SDNR-minimized BLISS fit results in a much deeper eclipse than either the χ^2_{bin}-minimized BLISS or PLD fits, likely due to correlated noise in the fixed-radius aperture photometry (see Figure 3.2).

68

For this and the following observations, we perform an MCMC calculation of the band-integrated brightness temperature using the MC^3 posterior distribution of eclipse depths. We use an ATLAS9 stellar spectrum and assume the planet is a blackbody. The light-curve fitting results and subsequent temperature calculations are listed in Table 3.3.

Table 3.4: Ramp Model Comparison

	BLISS min. SDNR		BLISS min. χ^2_{bin}		PLD min. χ^2_{bin}	
Ramp	ΔBIC	P_{21}	ΔBIC	P_{21}	ΔBIC	P_{21}
3.6 μm, visit 1						
Quadratic	0.0	—	0.0	—	0.0	—
Linear	120.0	8.76×10^{-27}	25.4	3.05×10^{-6}	126.9	$2.78-28$
None	732.7	7.87×10^{-160}	43.4	3.77×10^{-10}	605.1	4.02×10^{-132}
3.6 μm, visit 2						
Quadratic	0.0	—	0.0	—	0.0	—
Linear	2.8	2.47×10^{-1}	10.2	6.10×10^{-3}	97.9	5.51×10^{-22}
None	236.5	4.41×10^{-52}	326.5	1.26×10^{-71}	368.3	1.06×10^{-80}
4.5 μm, visit 1						
Quadratic	18.1	1.17×10^{-4}	11.1	3.89×10^{-3}	0.0	—
Linear	7.2	2.73×10^{-2}	0.0	—	26.3	1.95×10^{-6}
None	0.0	—	12.7	1.75×10^{-3}	38.2	5.07×10^{-9}
4.5 μm, visit 2						
Quadratic	17.5	1.58×10^{-4}	17.2	1.84×10^{-4}	21.8	1.85×10^{-5}
Linear	9.3	9.56×10^{-3}	9.5	8.65×10^{-3}	5.9	5.23×10^{-2}
None	0.0	—	0.0	—	0.0	—

3.4.5   Channel 1, Visit 2

For the second 3.6 μm observation, we again see significant telescope settling so we clip the first 10,000 frames ($\sim 12.6\%$). As in Section 3.4.4, we note flare-like activity, so we discard frames 49,664 – 57,580 (0.515 – 0.525 orbital phase). Again, we prefer a quadratic ramp function (Table 3.4) in all three cases. ZEN chooses a bin size of 4 frames. The resulting light curves are shown in Figure 3.3.

Figure 3.1: Normalized light curves from channel 1, visit 1, using each combination of modeling method and centering/photometry selection metric. The light curves are vertically offset by 0.4% for visual clarity.
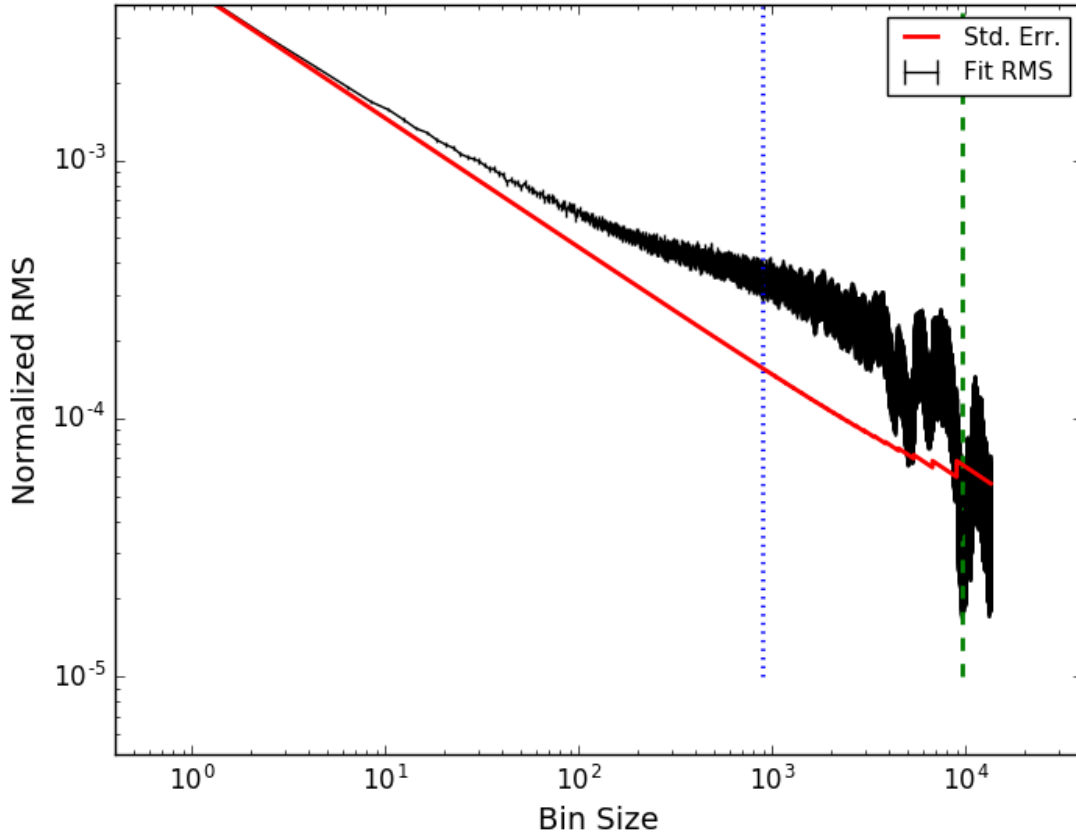
Figure 3.2: Correlated noise in the 3.6 μm, visit 1 data. The blue dashed line indicates the ingress/egress scale and the green dashed line indicates the eclipse duration scale. Correlated noise is present (at the corresponding scale) if the black line is above the red line.
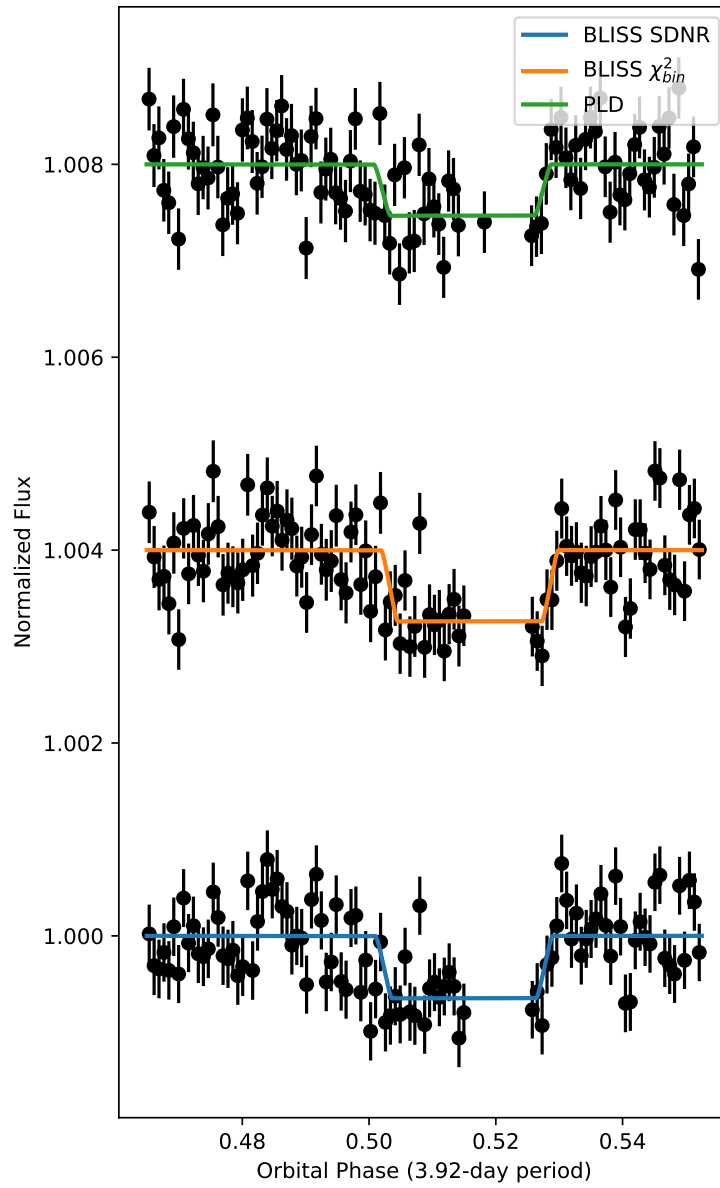
Figure 3.3: Normalized light curves from channel 1, visit 2, using each combination of modeling method and centering/photometry selection metric. The light curves are vertically offset by 0.4% for visual clarity.

3.4.6 Channel 2, Visit 1

With the first 4.5 μm observation, we discard the first 15,000 frames ($\sim 18.9\%$) to account for telescope settling. From a BIC comparison (Table 3.4) we note that the choice of BLISS *vs.* PLD and the choice of minimization metric impacts the optimal ramp model. This may explain the difference in eclipse depth and brightness temperature between the BLISS and PLD model results, as the quadratic ramp used with PLD can create an inverted eclipse-like shape, increasing the eclipse depth. ZEN chooses a bin size of 4 frames. The optimized light curves are shown in Figure 3.4.

3.4.7 Channel 2, Visit 2

In the final observation, telescope settling and the ramp effect is minimal, so we choose to not use a ramp function (see Table 3.4) or discard any frames at the start of the observation. However, we remove frames 11,400 – 11,600 as these images suffer from a telescope error that shifts the image by one pixel. There is significant PSF activity in this observation starting at approximately 0.5 orbital phase (see Figure 3.6), so we extend the limits of our variable-aperture and elliptical-aperture photometry parameterization for this observation only (see note in Table 3.2). ZEN chooses a bin size of 8 frames. The final light curves are shown in Figure 3.5 and the model results are listed in Table 3.3.
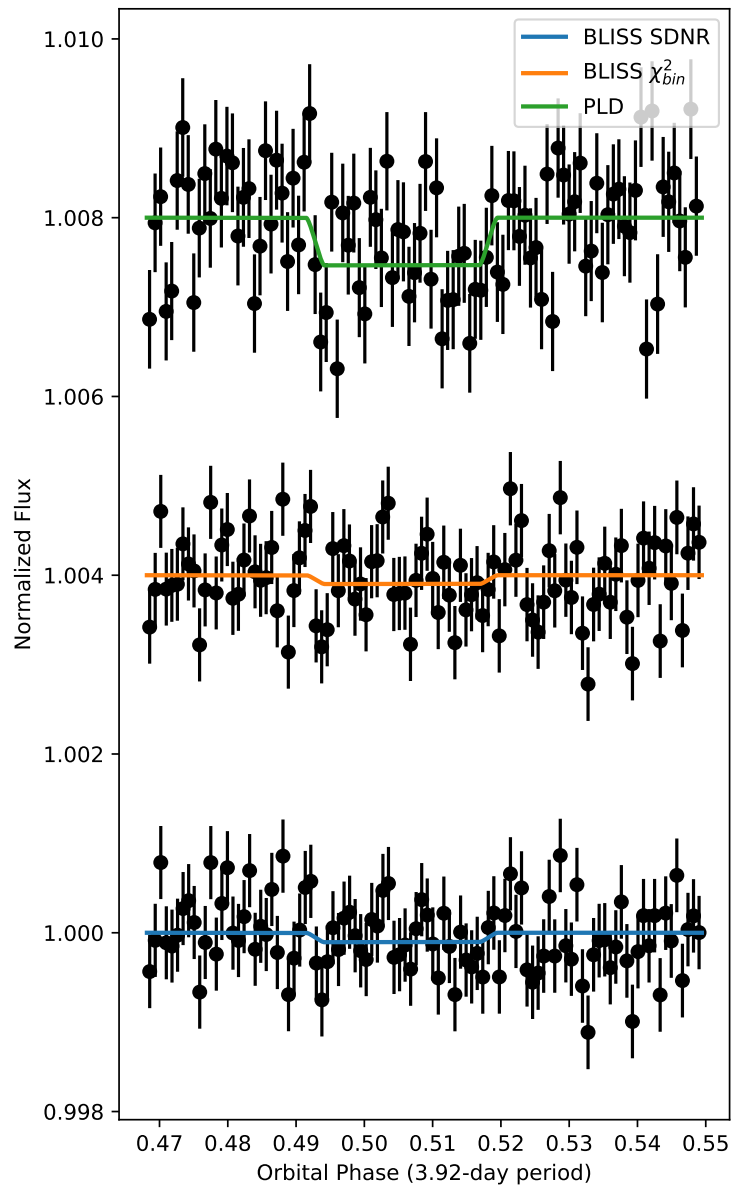
Figure 3.4: Normalized light curves from channel 2, visit 1, using each combination of modeling method and centering/photometry selection metric. The light curves are vertically offset by 0.4% for visual clarity.
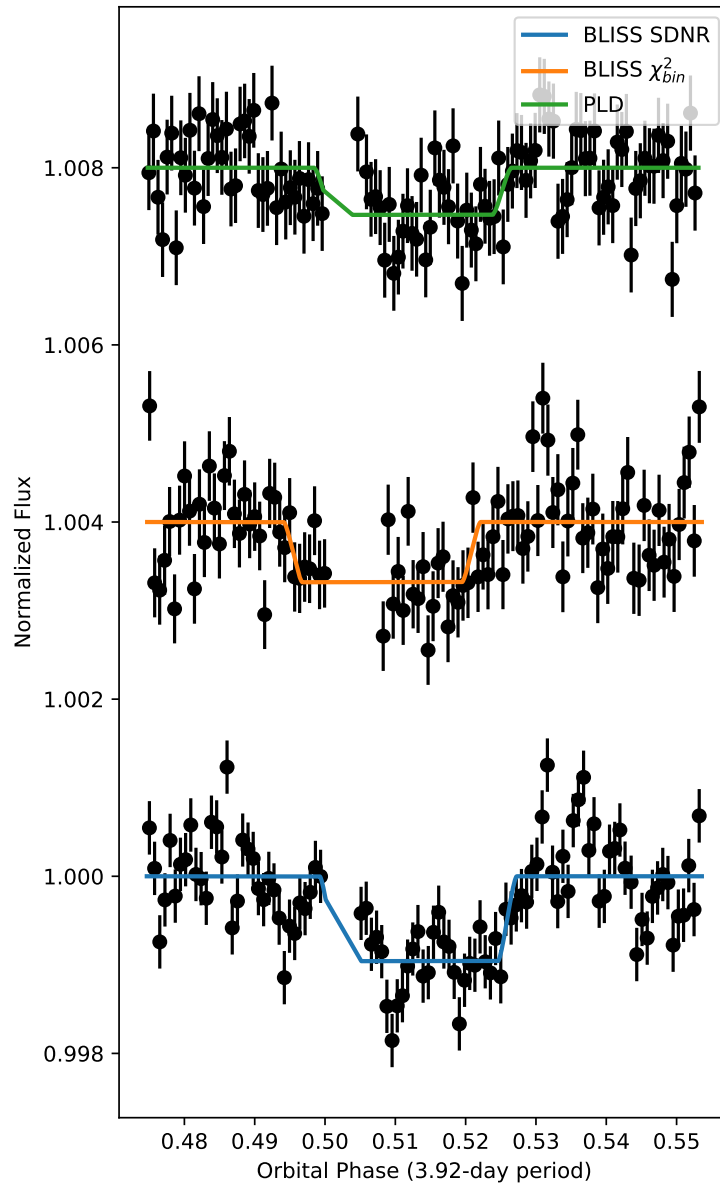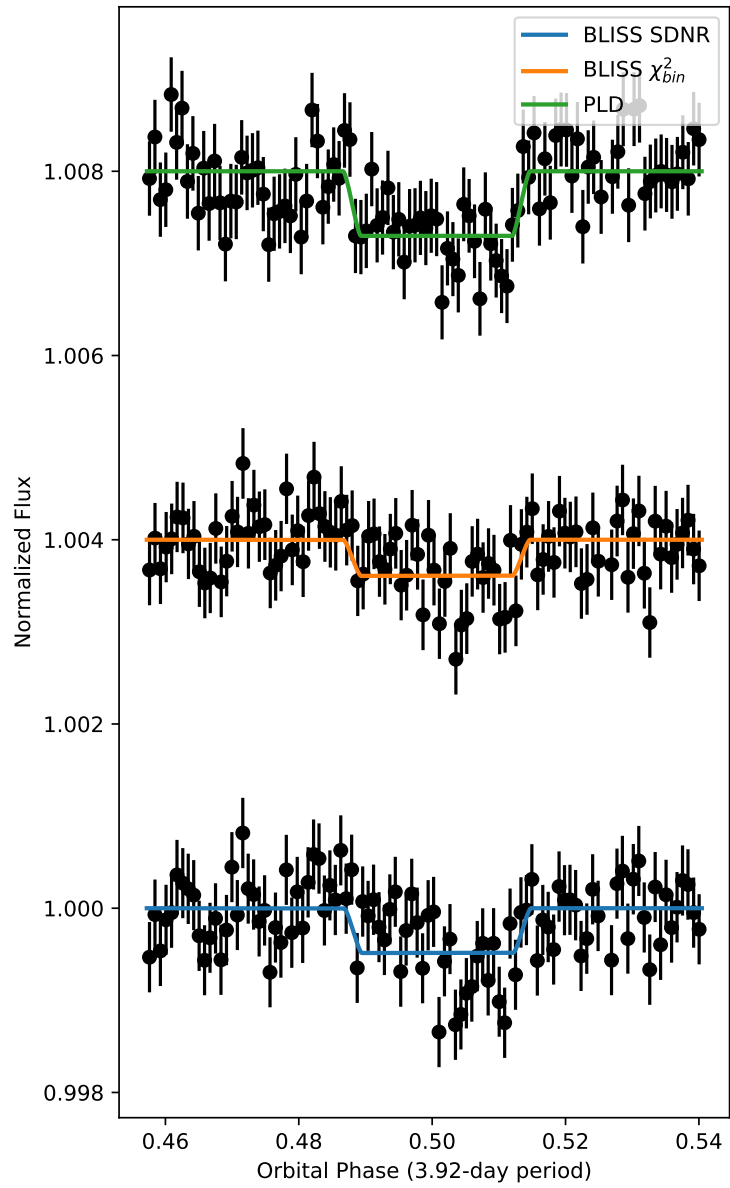
Figure 3.5: Normalized light curves from channel 2, visit 2, using each combination of modeling method and centering/photometry selection metric. The light curves are vertically offset by 0.4% for visual clarity.
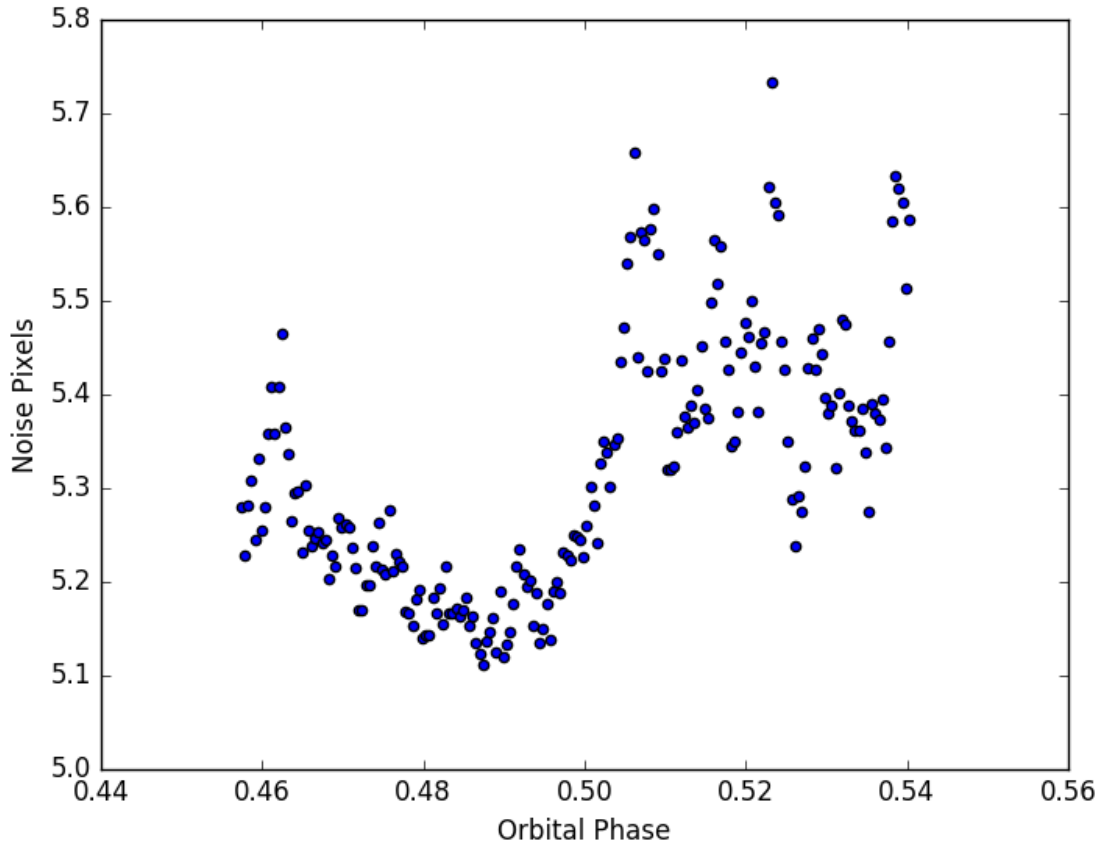
Figure 3.6: Noise pixel parameter for the second visit with channel 2, using an 8 pixel half-width square aperture. Values have been binned to 200 frames per bin for clarity. Note that the increase at ~ 0.50 orbital phase coincides with the sharp decrease in flux of the system.

3.4.8   Joint Light-Curve Fits

We also fit our light curves simultaneously, which allows us to share parameters between models. In our case, we share eclipse depths between the two 3.6 μm observations and between the two 4.5 μm observations. This significantly improves the signal-to-noise ratios of our measurements (see Table 3.5).

Table 3.5: Jointly Fit Eclipse Depths in Parts-Per-Million

Observations	PLD	BLISS, minimum χ^2_{bin}	BLISS, minimum SDNR
All Eclipses			
3.6 μm	434 ± 72	715 ± 78	807 ± 67
4.5 μm	567 ± 63	247 ± 75	301 ± 72

We should expect the eclipse midpoint to not vary between observations, but there are no acceptable fits where all observation share a single midpoint in orbital phase, as evidenced by the individual light curve fits in Table 3.3. Therefore, we let all the eclipses have separate orbital phases and investigate this behavior further with orbital fits.

3.5   Orbit

Arras et al. (2012) showed that tidally-induced stellar radial velocity measurements can be confused with orbital radial velocity, creating a false nonzero eccentricity measurement. By combining our eclipse midpoints with past observations, we can check for false positives in eccentricity and reduce the uncertainty on such measurements. We used an MCMC algorithm described in Campo et al. (2011) to jointly fit a Keplerian orbit to our eclipse timings (Table 3.3), published transit timings (Table 3.6), and CORALIE radial velocity data (Table 3.7, Hellier et al. 2010).

Table 3.6: WASP-29b Transit Events

Transit Midpoint Date BJD(TDB)	Error	Source
2455445.76245	0.00073	Dragomir et al. 2011
2454249.3305	0.0015	Hellier et al. 2010

Table 3.7: WASP-29b Radial-velocity Data

Date BJD(TDB)	RV (km s^{-1})	Error (km s^{-1})
2455071.8814	24.5671	0.0068
2455073.8810	24.4924	0.0068
2455074.8740	24.5118	0.0066
2455076.9032	24.5391	0.0180
2455092.6724	24.5422	0.0092
2455093.7263	24.4889	0.0066
2455094.7205	24.5298	0.0061
2455095.7121	24.5518	0.0070
2455097.7176	24.4844	0.0067
2455098.7330	24.5243	0.0061
2455116.7063	24.5058	0.0076
2455118.7652	24.5577	0.0078
2455129.6706	24.5188	0.0065
2455168.6361	24.4957	0.0049

Hellier et al. 2010

Our orbit model fits to $e\cos\omega$, $e\sin\omega$, apsidal precession rate $\dot{\omega}$, RV semi-amplitude k, orbital period P, transit ephemeris time t_0, system radial velocity $\dot{v}$, and system radial acceleration γ. The precession term is necessary since our data span 7.3 years, or 676 orbits, and a BIC comparison (see Equation 3.7) shows models which include apsidal precession are greatly preferred.

We fit, separately, to each set of results in Table 3.3 to study the impact each method has on retrieved orbital parameters. We discard the RV measurement at 2455094.7205 BJD$_{\text{TDB}}$ due to the Rossiter-Mclaughlin effect. The retrieved orbital parameters and the fits to transit and eclipse ephemerides are shown in Table 3.8 and Figure 3.7, respectively.

Table 3.8: Orbital Fit Results

Parameter	PLD	BLISS, minimum χ^2_{bin}	BLISS, minimum SDNR
Fitted Parameters			
$e\sin\omega$	0.017 ± 0.038	0.026 ± 0.001	0.006 ± 0.019
$e\cos\omega$	0.011 ± 0.011	-0.023 ± 0.004	0.020 ± 0.008
$\dot{\omega}$(°/orbit)	-0.258 ± 0.099	-0.330 ± 0.004	-0.134 ± 0.078
P (days)	3.922733 ± 0.000099	3.922646 ± 0.000020	3.922698 ± 0.000061
t_0 (BJD$_{\mathrm{TDB}}$)	2454649.411 ± 0.014	2454649.465 ± 0.008	2454649.428 ± 0.011
K (km/s)	36.3 ± 2.8	35.4 ± 2.5	36.3 ± 2.8
$\dot{v}$ (m/s/yr)	9.8 ± 23.9	-5.0 ± 23.8	6.9 ± 23.8
γ (m/s)	24513 ± 30	24529 ± 30	24517 ± 30
Derived Parameters			
e	$0.021^{+0.012}_{-0.005}$	$0.035^{+0.003}_{-0.003}$	$0.021^{+0.002}_{-0.002}$
ω_0(°)	56^{+24}_{-14}	132^{+6}_{-4}	17^{+63}_{-13}

The orbital parameters retrieved from the fit to the SDNR-minimized BLISS and PLD light curves are consistent within $\sim 1\sigma$. However, we note a significant different between the χ^2_{bin}-minimized BLISS fits and the other two cases, particularly in $e\cos\omega$ and t_0 (and, thus, e and ω_0). This difference is primarily driven by the eclipse midpoint of the first visit in the 3.6 μm channel. There are clear differences in the light curves produced by each model, which raises concerns about the accuracy of the methods. However, this observation has the most significant correlated noise (see Figure 3.1), and we had to discard most of the ingress due to possible stellar activity. Both factors likely contribute to the differences in the measured midpoints. Given that the eclipse timings of the other three observations are very consistent between the methods, we suspect that this discrepancy is a result of poor data quality.
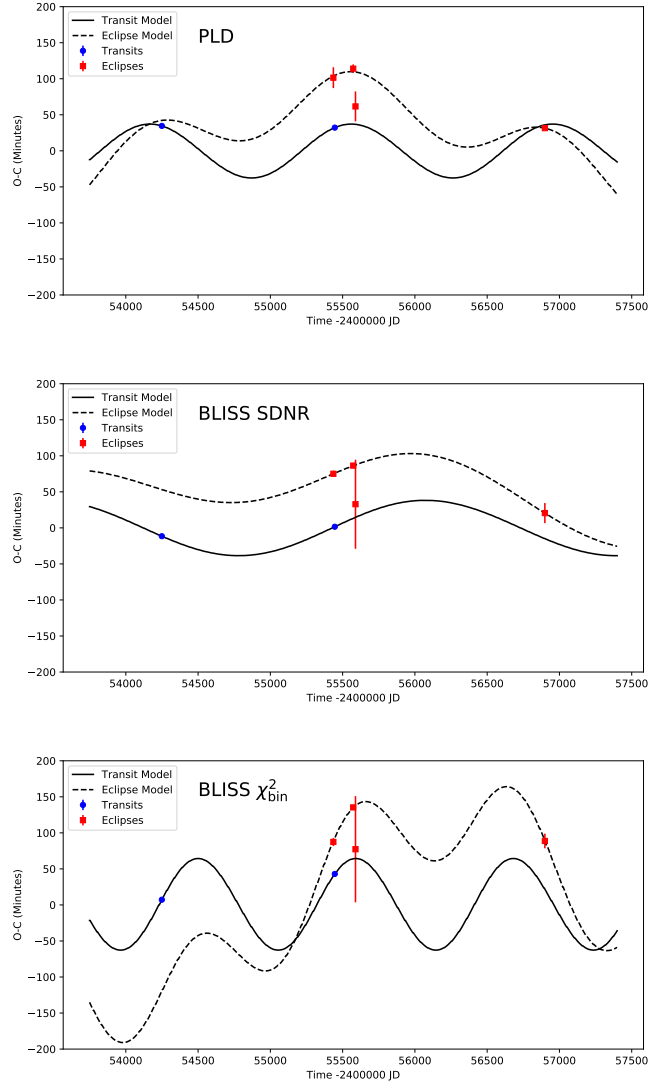
Figure 3.7: Timing residuals for the transit and eclipse midpoints, relative to predictions for a circular orbit. The dashed line and solid lines show the best-fitting models for transit and eclipse data, respectively. Red points are eclipse midpoints from this work, and blue points are transit midpoints from previous works (see Table 3.6). Labels indicate light-curve modeling method. These fits also include the 13 data points in Table 3.7 (one discarded due to the Rossiter-McLaughlin effect), but plots of these data are similar for all three cases.

We derived the MCMC eccentricity and angle of periastron distributions from posterior distributions of $e\cos\omega$ and $e\sin\omega$, and the asymmetric eccentricity distribution from the 1σ widths of this new distribution. We significantly improve the eccentricity over the previously-measured $0.03^{+0.05}_{-0.03}$ (Hellier et al. 2010).

Since we have a non-zero eccentricity detection in several fits, we investigate the planet's orbital circularization timescale. This timescale, from Goldreich & Soter (1966), is given by

$$\tau_e = \frac{4}{63} Q \left(\frac{a^3}{GM} \right)^{1/2} \left(\frac{m}{M} \right) \left(\frac{a}{R_{\mathrm{p}}} \right)^5, \tag{3.12}$$

where Q is a factor related to tidal dissipation, typically $\sim 10^6$ for a gas giant (Wu 2005), a is orbital radius, M is the mass of the star, m is the mass of the planet, and R_p is the radius of the planet. Taking $a = 0.0457 \pm 0.0006$ AU, $M = 0.825 \pm 0.033$ M$_\odot$, $m = 0.244 \pm 0.020$ M$_{\mathrm{J}}$, and $R_p = 0.792 \pm 0.046$ R$_{\mathrm{J}}$ (Hellier et al. 2010), we find a circularization timescale of ~ 1.1 Gyr. Hellier et al. (2010) estimate the age of the system to be 15 ± 8 Gyr, which does not rule out a young system that has yet to circularize. Even an old system could host eccentric orbits, however, through perturbations by another planet in the system (Mardling 2007, Zhang et al. 2013) or the planet could have migrated to its current position.

All our orbital fits suggest a significant apsidal precession due to the changes in orbital phase of the eclipse ephemerides. Jordán & Bakos (2008) state that general relativistic precession rate of hot Jupiters can be considerable due to their low orbital semimajor axes, such that it may be detectable in $\lesssim 10$ years. Assuming the system parameters as above, a period of 3.922646 days, an eccentricity of 0.035, a sun-like quadrupole moment of 10^{-6}, a planetary apsidal motion constant of

0.25, and a stellar apsidal motion constant of 0.01, we estimate a general relativistic precession rate of $\dot{\omega}_{\mathrm{GR}} = 1.79$ °/century, a stellar quadrupole moment precession rate of $\dot{\omega}_{\mathrm{quad}} = 0.04$ °/century, and a tidal deformation precession rate of $\dot{\omega}_{\mathrm{tide}} = 1.70$ °/century This is a total apsidal precession rate of $\dot{\omega} = 3.54$ °/century, several orders of magnitude lower than our maximum fitted $\dot{\omega}$ of 3070 °/century.

An outer companion planet could induce significant apsidal precession, but such a planet would need to be extremely massive. Applying Equation 8 of Jordán & Bakos (2008), a perturbing planet with twice WASP-29b's semimajor axis would need to have a mass $> 8M_{\mathrm{J}}$ to cause precession of this magnitude; a companion with a 1 AU orbit similar to the $> 15M_{\mathrm{J}}$ HAT-P-13c (Bakos et al. 2009) would need a mass $> 10M_{\odot}$. Given the implausibility of these scenarios, we are skeptical of this precession detection. Further eclipse and transit observations, or RV measurements with more sensitive instruments could pin down WASP-29b's orbit and determine if a companion is present.

3.6 Atmosphere

We used our Bayesian Atmospheric Radiative Transfer (BART) code (Harrington et al. 2020, Cubillos et al. 2020, Blecic et al. 2020, https://github.com/exosports/BART) to retrieve the atmosphere of WASP-29b. This code consists of three independent modules: Transit (Rojo 2006), which calculates planetary emission and transmission spectra; Thermochemical Equilibrium Abundances (TEA, Blecic et al. 2016), which determines molecular abundances from input atomic species and atmospheric thermal structure; and MC^3 (Cubillos et al. 2017), which varies input parameters to determine atmospheric temperature-pressure profiles and molecular composi-

tions. The framework was tested on retrieving temperature profiles and abundances of secondary eclipse observations of WASP-43b and transit observations of HAT-P-11b, confirming results from the literature (Blecic 2016, Cubillos 2016). However, with two photometric channels of WASP-29b, we cannot tightly constrain its atmosphere. Still, the Bayesian methods of BART show us what the data can tell us.

BART, using TEA, can create atmospheres in chemical equilibrium and scale these abundance profiles. However, this makes any resulting fit a function of the initial thermal profile and our limited data only constrain a small portion of the planet's atmosphere. Also, photochemistry and quenching can drive atmospheres away from chemical equilibrium (Moses 2014). Therefore, we choose to use molecular abundance profiles that are constant with pressure.

For all the following fits, we use the thermal profile function of Line et al. (2013), which has five parameters: γ_1 and γ_2, the ratios of Planck mean opacities in the two visible streams to the infrared stream; α, a parameter that divides flux between the visible streams; β, which represents the albedo, emissivity, and thermal redistribution of the planet; and κ_{IR}, the infrared Planck mean opacity. We fit to logarithmic scaling factors on constant abundance profiles for CO, CO_2, CH_4, and H_2O, for a total of 9 free parameters. All parameters have uniform, non-informative priors with large boundaries to allow full exploration of parameter space. All molecular abundance parameters have an upper limit of 10% of the atmosphere. Opacity sources include the aforementioned four molecules and H_2-H_2 collision-induced absorption.

We fit to all three sets of eclipse depths in Table 3.5, using several cases, and choose the best with a BIC comparison:

1. All parameters free (κ_{IR}, γ_1, γ_2, α, β, and logarithmic scaling factors for CO, CO_2, CH_4, and H_2O abundances).

2. Same as case 1, but with CO_2 and CH_4 abundances fixed to 2.8×10^{-4} and 1.4×10^{-4}, respectively. These are TEA-computed abundances at 0.1 bars pressure and 1000K. These molecules are not expected to be abundant at the temperatures and pressures probed in hot Jupiters.

3. Same as case 2, but with the H_2O abundance fixed to 5.2×10^{-4}, computed with TEA under the same conditions as above. Our tests show that the H_2 abundance is unconstrained, meaning that the parameter can fixed without compromising goodness-of-fit.

4. Same as case 3, but with $\alpha = 0$ and $\gamma_2 = 1$, removing on visible stream from the thermal profile.

5. Same as case 4, but with $\beta = 1$, which sets the irradiation temperature equal to the planet's equilibrium temperature, assuming an albedo of zero and perfect day-night heat redistribution.

6. An isothermal atmosphere, with only temperature as a free parameter.

7. Same as case 5, but with the CO abundance fixed to 3.2×10^{-4}, computed with TEA as done in cases 2 and 3. We only use this case for the PLD eclipse depths, since the CO abundance is unconstrained when using those data.

Case 1 represents the most flexible model. Cases 2 and 3 simplify the atmospheric composition. Cases 4 to 6 represent a range from complex to simple thermal structures. Case 7 is a simplified version of case 5 that we use with the PLD eclipse depths. In all cases but case 7 we keep the CO abundance as a free parameter because the relatively shallow BLISS eclipse depth at 4.5 μm requires an absorber.

Table 3.9: Convergence Criteria

Light-curve Model	SPEIS	ESS	3σ Accuracy
PLD	65	615	0.0021
BLISS SDNR	180	556	0.0022
BLISS χ^2_{bin}	300	333	0.0028

With the SDNR-minimized and χ^2_{bin}-minimized BLISS eclipse depths, a BIC comparison prefers case 4, with a non-inverted atmosphere and an implausibly large 10% CO abundance. The low eclipse depth at 4.5 μm requires a cold upper atmosphere with significant absorption, and the strong emission at 3.6 μm demands a hot lower atmosphere. It is possible that the atmosphere contains other molecules with opacity at 4.5 μm, such that in combination they produce a low eclipse depth, but we cannot fit more complex models with our limited broadband photometry. Also, given that the 4.5 μm eclipse is much deeper, we are skeptical of any inferences made from this single data point. With the PLD eclipse depths, we prefer case 7 with a non-inverted thermal structure and molecular abundances in thermochemical equilibrium at 0.1 bars pressure and 1000 K. Figures 3.8 and 3.9 show the retrieved temperature-pressure profiles and spectra, respectively.

We ensure convergence of the BIC-optimized models by assessing MCMC Steps Per Effectively-Independent Sample (SPEIS) and Effective Sample Size (ESS), and computing the accuracy of the posterior (Harrington et al. 2020). Briefly, SPEIS is the number of MCMC iterations required to become independent from the starting position, and ESS is the number of independent samples in the total MCMC sample. We convert the ESS to a relative accuracy in the 3σ credible region of the posterior. The results are listed in Table 3.9.

The code used to produce these results, the inputs, outputs, and commands to run the code are included in a reproducible-research compendium at `https://doi.org/10.5281/zenodo.3759974`. This compendium also includes digital versions of the data shown in the figures and the light curves used to derive the inputs to our atmopsheric retrieval. We also supply the best-fit models and the (nominal) correlated noise diagnostics.

3.7   Conclusions

We have presented light-curve, orbital, and atmospheric analyses of four *Spitzer* eclipse observations of WASP-29b, using a variety of centering, photometry, and light-curve modeling methodologies.

We modeled the light curves with both BLISS and PLD. With BLISS, in an effort to account for correlated noise, we separately chose the centering and photometry methods that minimized the SDNR and χ^2_{bin}. While minimizing χ^2_{bin} leads to larger or equivalent uncertainties on eclipse depth, we prefer this criterion because it more effectively removes correlated noise.

The PLD and χ^2_{bin}-minimized BLISS results agree within $\sim 1\sigma$ on eclipse midpoints, except the first 3.6 µm observation, which has significant correlated noise and possible stellar activity. However, the χ^2_{bin}-minimized BLISS eclipse depths and PLD eclipse depths differ by $> 3.3\sigma$ at 4.5 µm. These modeling methods chose different photometry aperture shapes and sizes, so the discrepancies between the light curves may be a result of photometry techniques rather than the differences in the light-curve models.

Figure 3.8: From top left to bottom: BART-retrieved thermal profiles from the PLD results, from the SDNR-optimized BLISS results, and from the χ^2_{bin}-optimized BLISS results. The shaded regions reflect the 68% and 95% boundaries. Note that the thermal profile is only constrained in a small region near $\sim$0.1 bars, and hence the best fit line must fall within the shaded region at that pressure. At other pressures, the temperature does not affect the spectral fit and thus, nothing keeps the best fit from traveling outside the shaded region. The dashed lines show the normalized emission contribution functions for each *Spitzer* filter.

We used these eclipse observations to further constrain the orbit of WASP-29b. All fits detect a non-zero eccentricity (Table 3.8). The fits are consistent except in transit time and $e\cos\omega$ due to differences in eclipse times in the first observation, which suffers from poor data quality. Our fits also suggest significant apsidal precession, but we rule this out because relativistic, tidal, and stellar quadrupole precession are negligible, and a perturbing body would have to be implausibly large to induce such precession.

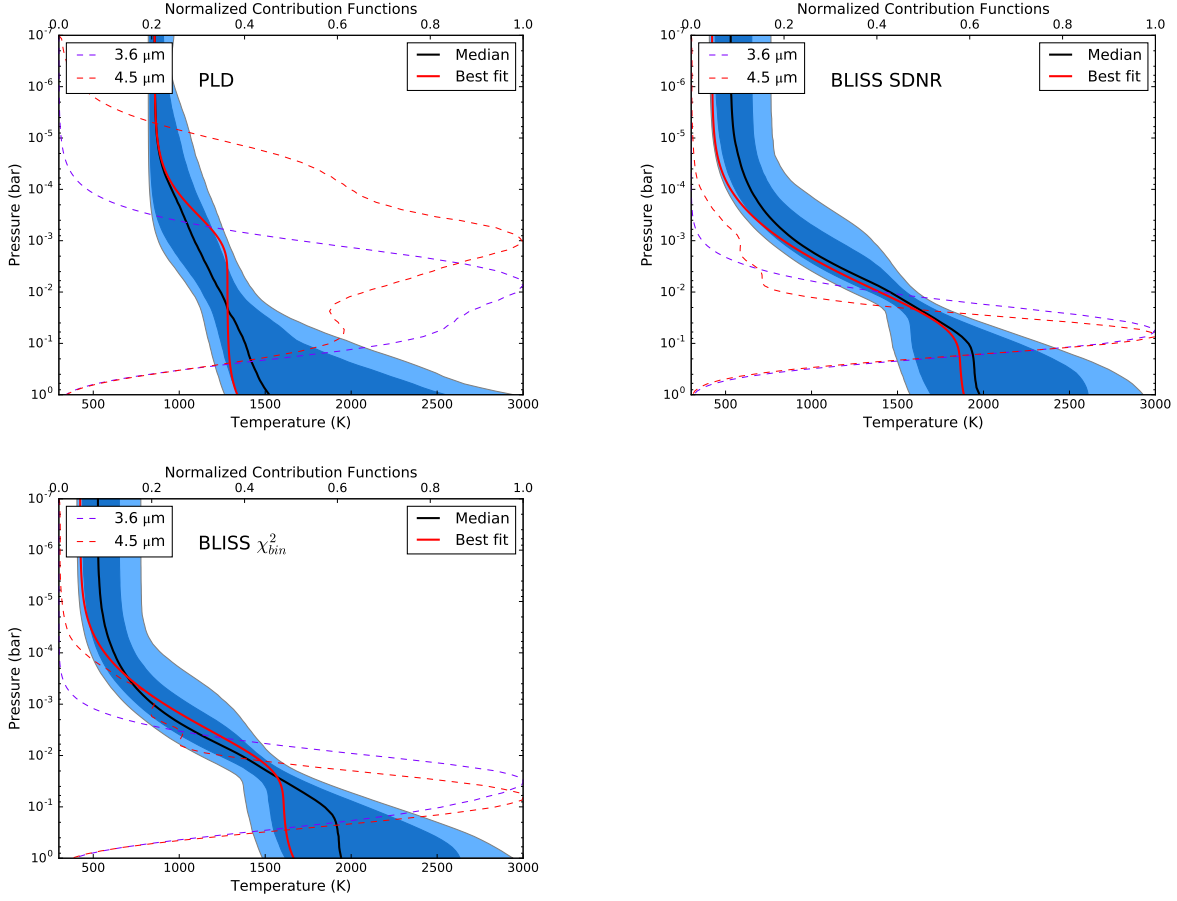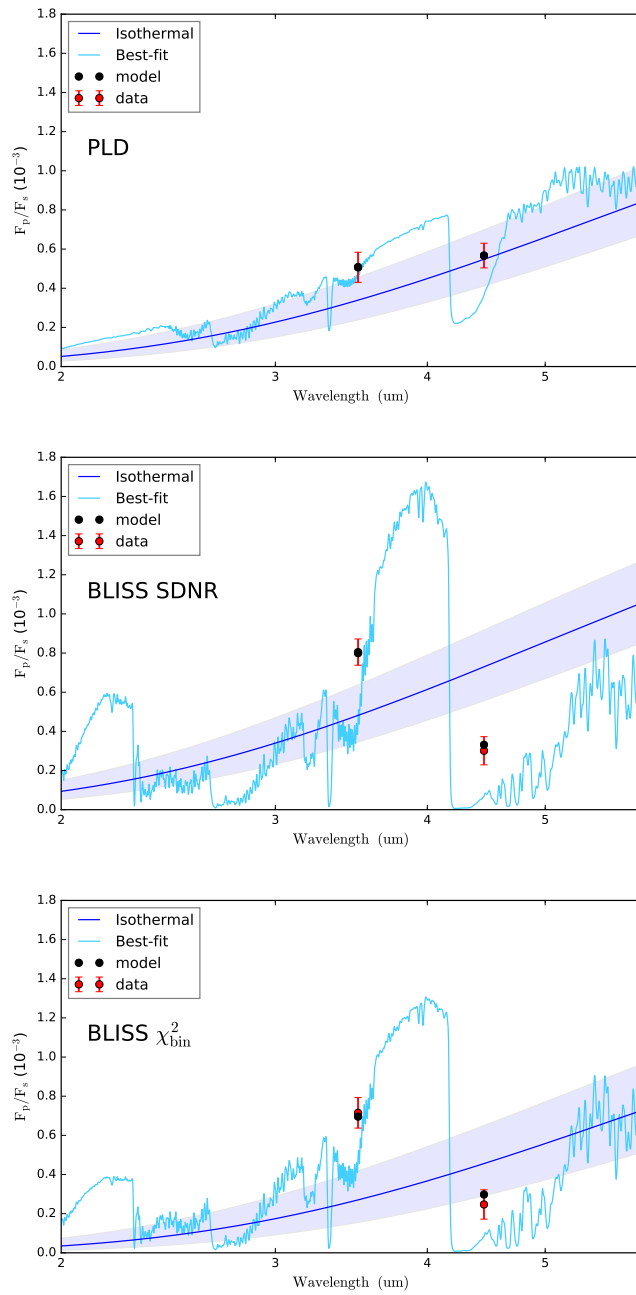Figure 3.9: From top to bottom: BART-retrieved spectrum from the PLD results, from the SDNR-optimized BLISS results, and from the χ^2_{bin}-optimized BLISS results. The black model points are the best-fit spectrum integrated over the IRAC filters. Note that due to overfitting, the binned model points entirely overlap the data. We also include the isothermal model fits with a shaded 3σ region.

Similarly, we performed day-side atmospheric retrieval with BART on jointly-fit eclipse depths in each channel. The shallow BLISS eclipse depth at 4.5 μm requires an unlikely CO-dominated atmosphere, far outside thermochemical equilibrium. The PLD eclipse depths suggest a more expected atmosphere, with a non-inverted thermal structure and molecular abundances near thermochemical equilibrium.

Choosing between BLISS and PLD is a non-trivial question, and the answer is beyond the scope of this work. BLISS is a physical model which is unable to remove astrophysical effects, as long as they are not correlated with target position. However, it is only able to remove gain-variation effects and is dependent on pixel bin size, which is difficult to optimize (Schwartz & Cowan 2017). Although the PLD model has a physical motivation, it has mathematical origins, which may hide behavior. It might be prone to overfitting, as it uses many more free parameters than BLISS. However, PLD only implicitly depends on the centering method, in the sense that the photometry depends on centering.

Given the physical scenarios required to explain the BLISS models, we cautiously prefer the PLD light curves. However, neither method is clearly superior, and without knowledge of the true planetary parameters, we cannot know which model gives the most accurate results. We stress the importance of applying multiple modeling methods, and carefully choosing the photometry and centering methods, to best address correlated noise.

The low S/N of WASP-29b *Spitzer* eclipses prohibits strong constraints on both the planet's orbit and its atmosphere. Additional eclipse timings, transit timings, and radial velocity data could constrain the orbit and determine the truth of the possible precession, but constraining atmosphere will require a higher S/N and additional wavelength coverage such as will be provided by the *James Webb Space Telescope*.

3.8 List of References

Arras, P., Burkart, J., Quataert, E., & Weinberg, N. N. 2012, MNRAS, 422, 1761

Bakos, G. Á., Howard, A. W., Noyes, R. W., Hartman, J., Torres, G., Kovács, G., Fischer, D. A., Latham, D. W., Johnson, J. A., Marcy, G. W., Sasselov, D. D., Stefanik, R. P., Sipőcz, B., Kovács, G., Esquerdo, G. A., Pál, A., Lázár, J., Papp, I., & Sári, P. 2009, ApJ, 707, 446

Blecic, J. 2016, ArXiv e-prints

Blecic, J., Harrington, J., & Bowman, M. O. 2016, ApJS, 225, 4

Blecic, J., Harrington, J., Cubillos, P. E., Bowman, M. O., Rojo, P., Stemm, M. M., Challener, R. C., Foster, A. J., Dobbs-Dixon, I., Foster, A. S., Lust, N. B., Blumenthal, S. D., Bruce, D., Himes, M. D., & Loredo, T. J. 2020, ApJ, in prep

Blecic, J., Harrington, J., Madhusudhan, N., Stevenson, K. B., Hardy, R. A., Cubillos, P. E., Hardin, M., Bowman, O., Nymeyer, S., Anderson, D. R., Hellier, C., Smith, A. M. S., & Collier Cameron, A. 2014, ApJ, 781, 116

Blecic, J., Harrington, J., Madhusudhan, N., Stevenson, K. B., Hardy, R. A., Cubillos, P. E., Hardin, M., Campo, C. J., Bowman, W. C., Nymeyer, S., Loredo, T. J., Anderson, D. R., & Maxted, P. F. L. 2013, ApJ, 779, 5

Branch, M. B., Coleman, T. F., & Li, Y. 1999, SIAM J. Sci. Comp., 21, 1

Buhler, P. B., Knutson, H. A., Batygin, K., Fulton, B. J., Fortney, J. J., Burrows, A., & Wong, I. 2016, ApJ, 821, 26

Campo, C. J., Harrington, J., Hardy, R. A., Stevenson, K. B., Nymeyer, S., Ragozzine, D., Lust, N. B., Anderson, D. R., Collier-Cameron, A., Blecic, J., Britt, C. B. T., Bowman, W. C., Wheatley, P. J., Loredo, T. J., Deming, D., Hebb, L., Hellier, C., Maxted, P. F. L., Pollaco, D., & West, R. G. 2011, ApJ, 727, 125

Charbonneau, D., Allen, L. E., Megeath, S. T., Torres, G., Alonso, R., Brown, T. M., Gilliland, R. L., Latham, D. W., Mandushev, G., O'Donovan, F. T., & Sozzetti, A. 2005, ApJ, 626, 523

Charbonneau, D., Brown, T. M., Noyes, R. W., & Gilliland, R. L. 2002, ApJ, 568, 377

Cubillos, P., Harrington, J., Loredo, T. J., Lust, N. B., Blecic, J., & Stemm, M. 2017, AJ, 153, 3

Cubillos, P., Harrington, J., Madhusudhan, N., Foster, A. S. D., Lust, N. B., Hardy, R. A., & Bowman, M. O. 2014, ApJ, 797, 42

Cubillos, P., Harrington, J., Madhusudhan, N., Stevenson, K. B., Hardy, R. A., Blecic, J., Anderson, D. R., Hardin, M., & Campo, C. J. 2013, ApJ, 768, 42

Cubillos, P. E. 2016, ArXiv e-prints

Cubillos, P. E., Harrington, J., Blecic, J., Himes, M. D., Rojo, P. M., Loredo, T. J., Lust, N. B., Challener, R. C., Foster, A. J., Stemm, M. M., Foster, A. S., & Blumenthal, S. D. 2020, ApJ, in prep

Deming, D., Knutson, H., Kammer, J., Fulton, B. J., Ingalls, J., Carey, S., Burrows, A., Fortney, J. J., Todorov, K., Agol, E., Cowan, N., Desert, J.-M., Fraine, J., Langton, J., Morley, C., & Showman, A. P. 2015, ApJ, 805, 132

Deming, D., Seager, S., Richardson, L. J., & Harrington, J. 2005, Nature, 434, 740

Dragomir, D., Kane, S. R., Pilyavsky, G., Mahadevan, S., Ciardi, D. R., Gazak, J. Z., Gelino, D. M., Payne, A., Rabus, M., Ramirez, S. V., von Braun, K., Wright, J. T., & Wyatt, P. 2011, AJ, 142, 115

Fazio, G. G., Hora, J. L., Allen, L. E., Ashby, M. L. N., Barmby, P., Deutsch, L. K., Huang, J.-S., Kleiner, S., Marengo, M., Megeath, S. T., Melnick, G. J., Pahre, M. A., Patten, B. M., Polizotti, J., Smith, H. A., Taylor, R. S., Wang, Z., Willner, S. P., Hoffmann, W. F., Pipher, J. L., Forrest, W. J., McMurty, C. W., McCreight, C. R., McKelvey, M. E., McMurray, R. E., Koch, D. G., Moseley, S. H., Arendt, R. G., Mentzell, J. E., Marx, C. T., Losch, P., Mayman, P., Eichhorn,

W., Krebs, D., Jhabvala, M., Gezari, D. Y., Fixsen, D. J., Flores, J., Shakoorzadeh, K., Jungo, R., Hakun, C., Workman, L., Karpati, G., Kichak, R., Whitley, R., Mann, S., Tollestrup, E. V., Eisenhardt, P., Stern, D., Gorjian, V., Bhattacharya, B., Carey, S., Nelson, B. O., Glaccum, W. J., Lacy, M., Lowrance, P. J., Laine, S., Reach, W. T., Stauffer, J. A., Surace, J. A., Wilson, G., Wright, E. L., Hoffman, A., Domingo, G., & Cohen, M. 2004, ApJS, 154, 10

Gelman, A. & Rubin, D. B. 1992, Statistical Science, 7, 457

Goldreich, P. & Soter, S. 1966, Icarus, 5, 375

Hardy, R. A., Harrington, J., Hardin, M. R., Madhusudhan, N., Loredo, T. J., Challener, R. C., Foster, A. S. D., Cubillos, P. E., & Blecic, J. 2017, ApJ, 836, 143

Harrington, J., Himes, M. D., Cubillos, P. E., Blecic, J., Rojo, P. M., Challener, R. C., Lust, N. B., Bowman, M. O., Blumenthal, S. D., Dobbs-Dixon, I., Foster, A. S., Foster, A. J., Green, M., Loredo, T. J., McIntyre, K. J., & Stemm, M. M. 2020, ApJ, in prep

Hellier, C., Anderson, D. R., Collier Cameron, A., Gillon, M., Lendl, M., Maxted, P. F. L., Queloz, D., Smalley, B., Triaud, A. H. M. J., West, R. G., Brown, D. J. A., Enoch, B., Lister, T. A., Pepe, F., Pollacco, D., Ségransan, D., & Udry, S. 2010, ApJ, 723, L60

Ingalls, J. G., Krick, J. E., Carey, S. J., Laine, S., Surace, J. A., Glaccum, W. J., Grillmair, C. C., & Lowrance, P. J. 2012, in Proc. SPIE, Vol. 8442, Space Telescopes and Instrumentation 2012: Optical, Infrared, and Millimeter Wave, 84421Y

Ingalls, J. G., Krick, J. E., Carey, S. J., Stauffer, J. R., Lowrance, P. J., Grillmair, C. J., Buzasi, D., Deming, D., Diamond-Lowe, H., Evans, T. M., Morello, G., Stevenson, K. B., Wong, I., Capak, P., Glaccum, W., Laine, S., Surace, J., & Storrie-Lombardi, L. 2016, AJ, 152, 44

Jordán, A. & Bakos, G. Á. 2008, ApJ, 685, 543

Kilpatrick, B. M., Lewis, N. K., Kataria, T., Deming, D., Ingalls, J. G., Krick, J. E., & Tucker, G. S. 2017, AJ, 153, 22

Lewis, N. K., Knutson, H. A., Showman, A. P., Cowan, N. B., Laughlin, G., Burrows, A., Deming, D., Crepp, J. R., Mighell, K. J., Agol, E., Bakos, G. Á., Charbonneau, D., Désert, J.-M., Fischer, D. A., Fortney, J. J., Hartman, J. D., Hinkley, S., Howard, A. W., Johnson, J. A., Kao, M., Langton, J., & Marcy, G. W. 2013, ApJ, 766, 95

Line, M. R., Wolf, A. S., Zhang, X., Knutson, H., Kammer, J. A., Ellison, E., Deroo, P., Crisp, D., & Yung, Y. L. 2013, ApJ, 775, 137

Lust, N. B., Britt, D., Harrington, J., Nymeyer, S., Stevenson, K. B., Ross, E. L., Bowman, W., & Fraine, J. 2014, PASP, 126, 1092

Mandel, K. & Agol, E. 2002, ApJ, 580, L171

Mardling, R. A. 2007, MNRAS, 382, 1768

Morello, G., Waldmann, I. P., Tinetti, G., Howarth, I. D., Micela, G., & Allard, F. 2015, ApJ, 802, 117

Moses, J. I. 2014, Philosophical Transactions of the Royal Society of London Series A, 372, 20130073

Nymeyer, S., Harrington, J., Hardy, R. A., Stevenson, K. B., Campo, C. J., Madhusudhan, N., Collier-Cameron, A., Loredo, T. J., Blecic, J., Bowman, W. C., Britt, C. B. T., Cubillos, P., Hellier, C., Gillon, M., Maxted, P. F. L., Hebb, L., Wheatley, P. J., Pollacco, D., & Anderson, D. R. 2011, ApJ, 742, 35

Raftery, A. E. 1995, Sociological Mehodology, 25, 111

Rojo, P. M. 2006, PhD thesis, Cornell University

Schwartz, J. C. & Cowan, N. B. 2017, PASP, 129, 014001

Schwarz, G. 1978, Ann. Statist., 6, 461

Stevenson, K. B., Harrington, J., Fortney, J. J., Loredo, T. J., Hardy, R. A., Nymeyer, S., Bowman,
W. C., Cubillos, P., Bowman, M. O., & Hardin, M. 2012, ApJ, 754, 136

Stevenson, K. B., Harrington, J., Nymeyer, S., Madhusudhan, N., Seager, S., Bowman, W. C.,
Hardy, R. A., Deming, D., Rauscher, E., & Lust, N. B. 2010, Nature, 464, 1161

Werner, M. W., Roellig, T. L., Low, F. J., Rieke, G. H., Rieke, M., Hoffmann, W. F., Young,
E., Houck, J. R., Brandl, B., Fazio, G. G., Hora, J. L., Gehrz, R. D., Helou, G., Soifer, B. T.,
Stauffer, J., Keene, J., Eisenhardt, P., Gallagher, D., Gautier, T. N., Irace, W., Lawrence, C. R.,
Simmons, L., Van Cleve, J. E., Jura, M., Wright, E. L., & Cruikshank, D. P. 2004, ApJS, 154, 1

Wong, I., Knutson, H. A., Lewis, N. K., Kataria, T., Burrows, A., Fortney, J. J., Schwartz, J.,
Agol, E., Cowan, N. B., Deming, D., Désert, J.-M., Fulton, B. J., Howard, A. W., Langton, J.,
Laughlin, G., Showman, A. P., & Todorov, K. 2015, ApJ, 811, 122

Wu, Y. 2005, ApJ, 635, 688

Zhang, K., Hamilton, D. P., & Matsumura, S. 2013, ApJ, 778, 6

CHAPTER 4: SPITZER DAYSIDE EMISSION OF WASP-34b

Ryan C. Challener[1]**, Joseph Harrington**[1]**, Patricio E. Cubillos**[1,2]**, Jasmina Blecic**[1,3]**, and Barry Smalley**[4]

[1] *Planetary Sciences Group, Department of Physics, University of Central Florida, Orlando, FL 32816-2385*
[2] *Space Research Institute, Austrian Academy of Sciences, Graz, Austria*
[3] *New York University Abu Dhabi, Abu Dhabi, United Arab Emirates*
[4] *Astrophysics Group, Keele University, Staffordshire ST5 5BG, UK*

4.1 Abstract

We analyzed two eclipse observations of the low-density, transiting, and likely grazing exoplanet WASP-34b with the *Spitzer Space Telescope's* InfraRed Array Camera using two techniques to correct for intrapixel sensitivity variation: Pixel-Level Decorrelation and BiLinearly Interpolated Subpixel Sensitivity. Timing results are extremely consistent ($\lesssim 0.7\sigma$) between the two models and eclipse depths are consistent within $\lesssim 2.3\sigma$, where the difference is due to photometry methods, not the models themselves. By combining published radial velocity data, amateur and professional transit observations, and our eclipse timings, we improved upon measurements of orbital parameters and found an eccentricity consistent with zero. Atmospheric retrieval, using our Bayesian Atmospheric Radiative Transfer code, shows that the planetary spectrum most resembles a blackbody, with no constraint on molecular abundances or vertical temperature variation.

4.2 Introduction

Relative system flux variations, during planetary and stellar occultations, are the primary way we characterize exoplanetary atmospheres. Eclipse observations, when the planet passes behind the star, reveal temperature and atmospheric composition of the planet's day side, and eclipse ephemerides constrain planetary orbital eccentricity.

In this work, we analyzed two *Spitzer Space Telescope* (Werner et al. 2004) InfraRed Array Camera (IRAC, Fazio et al. 2004) eclipse observations of the exoplanet WASP-34b. WASP-34b is a hot Jupiter on a potentially-grazing orbit around a Sun-like star. Its mass of 0.59 ± 0.01 Jupiter masses and radius of 1.22 ± 0.08 Jupiter radii imply a very low density of $\sim 0.43 \pm 0.01$ g/cm^3 (Smalley et al. 2011).

97

IRAC exhibits several systematic effects which must be carefully removed. Of particular interest for this work is a correlation between target position and flux due to subpixel gain variation in the detector. Several methods have been used to deal with this effect, including polynomial maps (e.g. Charbonneau et al. 2005), BiLinearly Interpolated Subpixel Sensitivity maps (BLISS, Stevenson et al. 2012), Pixel-Level Decorrelation (PLD, Deming et al. 2015), Independent Componenet Analysis (Morello et al. 2015), and Gaussian Processes (Gibson et al. 2012). We measure eclipse depths and timings utilizing both BLISS and PLD, which have been shown to be among the most accurate methods (Ingalls et al. 2016).

This paper is organized as follows: in Section 4.3 we present the observations, in Section 4.4 we describe our data analysis procedure, in Section 4.5 we fit orbital models to our light curve results, in Section 4.6 we present atmospheric retrievals based on measured eclipse depths, and in Section 4.7 we lay out our conclusions.

4.3   Observations

We observed WASP-34 once with each of the 3.6 and 4.5 μm photometric filters available during the warm *Spitzer* mission, as part of program 60003 (PI: Harrington). Each observation spanned ∼ 7 hours, such that the WASP-34b eclipses would occur roughly in the middle and there would be enough baseline to characterize and remove the *Spitzer* systematic effects. The two observations occurred 8 days apart, on July 19 and July 27 2010, or two orbits of WASP-34b. We used the 0.4 second exposure time for both observations.

4.4   Data Analysis

The challenge with *Spitzer* observations lies in correcting the telescope's systematic effects. IRAC was designed for 1% relative flux precision, but exoplanet eclipse observations are of order 0.1%. We are able to achieve $\sim$0.01% precision with a careful treatment of correlated noise using our Photometry for Orbits, Eclipses, and Transits code (POET, Nymeyer et al. 2011, Stevenson et al. 2012, Blecic et al. 2013, Cubillos et al. 2013, Blecic et al. 2014, Cubillos et al. 2014, Hardy et al. 2017).

POET applies a multitude of centering and photometry methods to produce light curves. We use center-of-light, Gaussian, and least-asymmetry (Lust et al. 2014) centering techniques. For photometry, we use three types of apertures: fixed, where the size of the aperture does not change over the course of an observation; variable, where the size of the aperture is adjusted for changes in the width of the point-spread function (PSF) according to the "noise pixels" (Lewis et al. 2013); and elliptical, where we use an elliptical aperture with x and y widths dependent on a Gaussian fit to the star in every frame (Challener et al. 2020). We try fixed-aperture radii from $1.5 - 4.0$ pixels in 0.25 pixel increments. For variable apertures, we use radii described by

$$R_{var} = a\sqrt{N} + b, \qquad (4.1)$$

where N is the noise-pixel measurement for a given frame, a ranges from $0.5 - 1.5$ in 0.25 increments, and b ranges from $-1 - 2$ in steps of 0.5. The elliptical-aperture sizes are given by

$$R_x = a\sigma_x + b,$$

$$R_y = a\sigma_y + b, \tag{4.2}$$

where σ_x and σ_y are the 1σ widths of a Gaussian fit to the star along the x and y axes, a ranges from $3 - 7$ in steps of 1, and b covers $-1 - 2$ in 0.5 increments.

POET chooses the best combination of centering and photometry methods by minimizing the binned-σ χ^2 (hereafter χ^2_{bin}, Deming et al. 2015). When dominated by white noise, the model standard deviation of normalized residuals (SDNR) should reduce predictably with bin size as $1/\sqrt{\mathrm{bin\ size}}$. The χ^2_{bin} measures how well a line of slope $-1/2$ fits to log(SDNR) vs. log(bin size), with a lower χ^2_{bin} indicating less correlated noise. The optimal centering and photometry methods are listed in Table 4.1.

Table 4.1: Centering and Photometry Parameters

Wavelength (µm)	Centering Method	Photometry Method	Aperture Radius[a] (pixels)
BLISS			
3.6	Gaussian	Elliptical	3.0+0.5
4.5	Least Asymmetry	Fixed	2.5
PLD			
3.6	Center-of-light	Fixed	2.00
4.5	Gaussian	Elliptical	4.00+0.5

[a] Variable and elliptical aperture radii are given as $a + b$ (Equations 4.1 and 4.2).

There are two main systematics in IRAC photometry: a non-flat baseline ("ramp") and a position-dependent gain variation across the detector at the subpixel level. The first can generally be corrected with a linear or quadratic function, or occasionally no correction is necessary. To remove the position-dependent effect, we use both BLISS (Stevenson et al. 2012) and PLD (Deming et al. 2015), separately.

BLISS grids the detector into subpixels. We use the root mean square (RMS) of the point-to-point variation in the x and y positions of the target on the detector as the grid size in each respective dimension. BLISS then directly computes the detector gain variation for each grid bin by assuming any remaining unmodeled effects are due to gain variation. This is dependent on the centering method, as each frame is assigned to a grid bin, and thus to a correction factor, based on the position of the target. With BLISS, the light curve model is

$$F(x, y, t) = F_s E(t) R(t) M(x, y) \tag{4.3}$$

where F_s is the total system flux, $E(t)$ is an eclipse model, $R(t)$ is a "ramp" model, and $M(x, y)$ is the BLISS map.

PLD notes that the motion of the target is encoded in the brightness of the pixels; if the target moves left, pixels on the left brighten and pixels on the right dim. It models the light curve as the sum of several of the brightest pixels, multiplied by a weighting factor. The pixel values are normalized at each frame such that their sum is one, so that any time-dependent astrophysical effects are removed. We choose to use the nine brightest pixels in this work. The light curve model is then

$$F(t) = F_s \left(\sum_{n_p=1}^{9} c_i \hat{P}_i^t + R(t) + E(t) \right), \tag{4.4}$$

where c_i are the pixel weights, $\hat{P}_i^t$ are the normalized pixel values at time t, $R(t)$ is a ramp model, and $E(t)$ is an eclipse model. PLD also bins the data in time and chooses the best binning level using χ^2_{bin}.

In this work, we try the following "ramp" functions with BLISS:

$$R(t) = 1, \tag{4.5}$$

$$R(t) = r_1(t - 0.5) + 1, \tag{4.6}$$

$$R(t) = r_2(t - 0.5)^2 + r_1(t - 0.5) + 1, \tag{4.7}$$

where r_i are free parameters and t is in units of orbital phase (transit occurs at 0 orbital phase). With PLD, we instead use the following functions, because PLD treats variations additively and thus, the functions must be relative to 0:

$$R(t) = 0, \tag{4.8}$$

$$R(t) = r_1(t - 0.5), \tag{4.9}$$

$$R(t) = r_2(t - 0.5)^2 + r_1(t - 0.5). \tag{4.10}$$

For the final fit, we choose the ramp model which results in the lowest Bayesian Information Criterion (BIC, Raftery 1995), given by

$$\mathrm{BIC} = \chi^2 + k \ln N_{\mathrm{data}}, \tag{4.11}$$

where k is the number of free parameters and N_{data} is the number of data points. The BIC is a measure of goodness of fit with a penalty for added free parameters. Relative model confidence is assessed as

$$P_{21} = \exp\left(-\frac{\mathrm{BIC}_2 - \mathrm{BIC}_1}{2}\right), \tag{4.12}$$

where model 2 has a larger BIC than model 1. Note that since the BIC is dependent on the size of the data set, data binning must be kept constant when comparing the BICs of different models.

For the eclipse model $E(t)$ we use a version of the uniform source model from Mandel & Agol (2002). Since WASP-34b is potentially a grazing planet (Smalley et al. 2011), we account for a nonzero impact parameter, and thus fit to the maximum depth of the eclipse (if it was not grazing), rather than the depth of the feature in the light curve. Such a model is necessary to get an accurate temperature measurement of the day side of the planet. For a planet smaller than its star, Mandel & Agol (2002) define the ratio of obscured light during a transit as $F^e(p, z) = 1 - \lambda^e(p, z)$, where

$$
\lambda^e(p, z) = \begin{cases} \frac{1}{\pi} \left(k_0 p^2 + k_1 - \sqrt{\frac{4z^2 - (1 + z^2 - p^2)^2}{4}} \right), & 1 - p < z < 1 + p \\ p^2, & z \leq 1 - p \\ 0, & \text{otherwise} \end{cases} \tag{4.13}
$$

where k_0 and k_1 are defined as

$$
k_0 = \arccos \left(\frac{p^2 + z^2 - 1}{2pz} \right), \tag{4.14}
$$

$$
k_1 = \arccos \left(\frac{1 - p^2 + z^2}{2z} \right), \tag{4.15}
$$

p^2 is the area ratio of the planetary disk to the stellar disk R_p/R_s, and z is the distance, in stellar radii, from center of the stellar disk to the center of the planetary disk, if both are projected onto a plane perpendicular to the line of sight.

For eclipses, we rewrite this function to separate the depth of the transit from the conditions of the piecewise definition. We note that the area of overlap between the planetary and stellar disks is

$$A_{\mathrm{over}} = A_s \lambda^e(p, z), \tag{4.16}$$

where $A_s = \pi R_s^2$ is the area of the stellar disk. Then, the area ratio of the obscured portion of the planetary disk to the total planetary disk is

$$A_{\mathrm{rat}} = \frac{\lambda^e(p, z)}{p^2}. \tag{4.17}$$

Then, if we define D as the flux ratio of the planet to the star, the eclipse function is

$$E(t) = 1 - D\frac{\lambda^e(p, z)}{p^2}. \tag{4.18}$$

We compute z as a function of time, eclipse midpoint, and impact parameter, where we assume the planet moves at a constant velocity behind the stellar disk dependent on the orbital period and semimajor axis. The full eclipse model has parameters for eclipse midpoint, planet-to-star flux ratio (maximum eclipse depth if non-grazing), impact parameter b, orbital period, stellar radius, planetary radius, and orbital semi-major axis.

In both observations the eclipse signals are too weak to constrain all model parameters, so we fix period to 4.31768 days, planetary radius to 1.22 R_J, stellar radius to 0.93 $R_\odot$, and semimajor axis to 0.0524 AU, all based on orbital parameters from Smalley et al. (2011). Models which fit both impact parameter and planet-to-star flux ratio determine $b \simeq 1$, but leave the flux ratio largely unconstrained. Given that we are interested in characterizing the planet's emission, we fix the impact parameter to 0.904 (Smalley et al. 2011). We note this b is for transit geometry but, since we later determine an orbit consistent with zero eccentricity (see Section 4.5), it is a reasonable choice for eclipse impact parameter. Thus, we fit to eclipse midpoint, planet-to-star flux ratio, and ramp parameters, as well as pixel weights when using PLD.

We determined best fits using least-squares and calculated uncertainties with Markov-chain Monte Carlo (MCMC) utilizing Multi-Core Markov-Chain Monte Carlo (MC[3], Cubillos et al. 2017). We rescale the data uncertainties such that our fits have a reduced χ^2 of 1, except when comparing BICs of ramp models, as the rescaling forces a "good" fit when there may be none. We ran our MCMC until the chains satisfied the Gelman-Rubin convergence test within 1% (Gelman & Rubin 1992). We use the MCMC posterior distribution of eclipse depths as a Monte Carlo sample to determine a band-integral brightness temperature for each observation.

4.4.1   3.6 μm

Assuming a non-inclined orbit, we expect a 3.6 μm eclipse S/N of < 5. Given that WASP-34b's orbit is likely grazing (Smalley et al. 2011), and that systematic effects are stronger at 3.6 μm, it is unsurprising that this detection is very weak. With BLISS, we determine an eclipse depth of 495 ± 126 ppm centered at $2455396.68703 \pm 0.00374$ BJD$_\mathrm{TDB}$ (barycentric dynamical time). PLD finds an eclipse depth of 557 ± 144 ppm at $2455396.67878 \pm 0.00432$ BJD$_\mathrm{TDB}$, using a bin

size of 8 frames. Figures 4.1 and 4.2 show the BLISS and PLD fits. These depths correspond to band-integrated brightness temperatures of 1160 ± 81 K and 1251 ± 100 K for BLISS and PLD, respectively. Table 4.2 lists the optimal ramp models for each systematic-removal technique. We note telescope settling was pronounced in this observation, so we clipped the first 10% and 17.5% of the data set for the BLISS and PLD fits, respectively.

Table 4.2: Ramp Model BICs

	BLISS		PLD	
Ramp	ΔBIC	P_{21}	ΔBIC	P_{21}
3.6 μm				
None	891.1	3.16×10^{-194}	317.5	1.14×10^{-69}
Linramp	97.4	7.08×10^{-22}	14.6	6.76×10^{-4}
Quadramp	0.0	—	0.0	—
4.5 μm				
None	0.6	7.41×10^{-1}	0.0	—
Linramp	0.0	—	10.1	6.41×10^{-3}
Quadramp	10.6	4.99×10^{-3}	19.9	4.77×10^{-5}

4.4.2   4.5 μm

Since the planet is brighter at 4.5 μm than 3.6 μm relative to the host star, here we expect a deeper eclipse. Indeed, BLISS finds an eclipse depth of 853 ± 155 at $2455405.30904 \pm 0.00306$ BJD$_{\text{TDB}}$, and PLD finds an eclipse depth of 1319 ± 145 ppm at $2455405.30725 \pm 0.00254$ BJD$_{\text{TDB}}$. These depths correspond to band-integrated brightness temperatures of 1250 ± 83 K and 1465 ± 68 K for BLISS and PLD, respectively. Figures 4.1 and 4.2 show the BLISS and PLD fits. Due to unusual sky level activity and a reaction wheel spike, we removed frames 49000 – 52000 and 53740 – 53790, respectively. Again, Table 4.2 compares the ramp models.
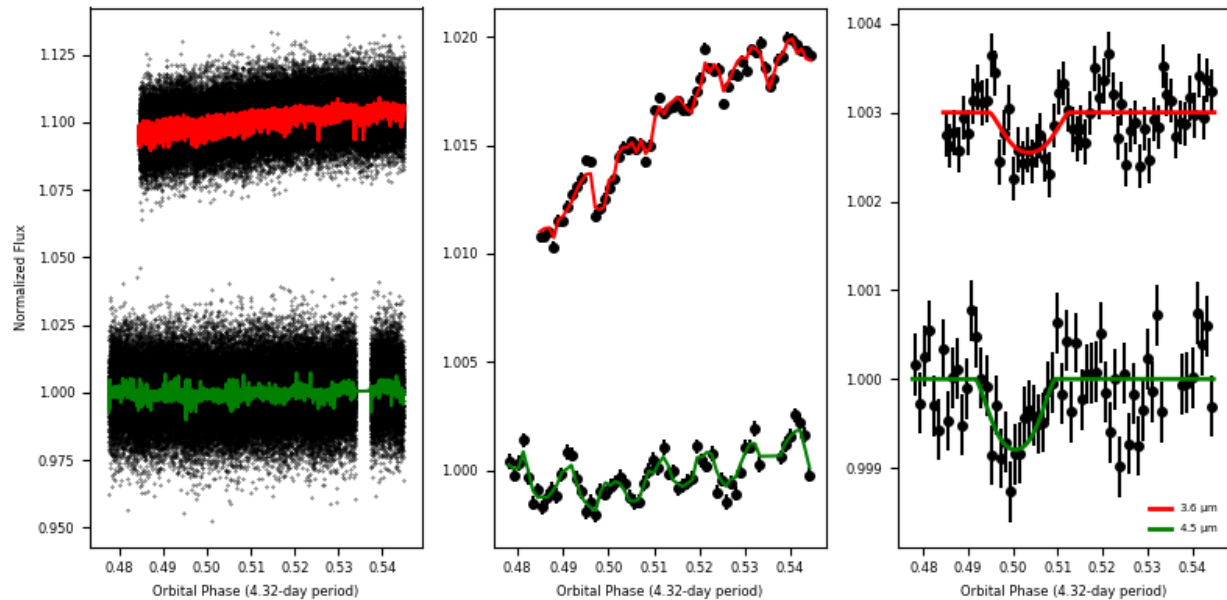
Figure 4.1: BLISS light curves of WASP-34, vertically offset for visual clarity. Note that we clipped out frames 49000 – 52000 due to erratic sky levels and frames 53740 – 53790 due to a reaction wheel spike. **Left:** Normalized raw photometry with best-fit models overplotted. **Middle:** Normalized binned photometry and binned best-fit models. **Right:** Normalized binned photometry and best-fit models with systematics divided out to highlight the eclipses.

We note there is a $\sim$2.1σ difference between these eclipse depths. This is entirely due to differences in the selected photometry methods. Regardless of PLD or BLISS, fixed aperture photometry finds an eclipse depth of $\sim$850 ppm, whereas variable and elliptical photometry produce an eclipse depth of $\sim$1300 ppm. Since the χ^2_{bin} prefers elliptical photometry when using a PLD model, we present those results, but note that, at least in this observation, the choice of photometry method impacts results.
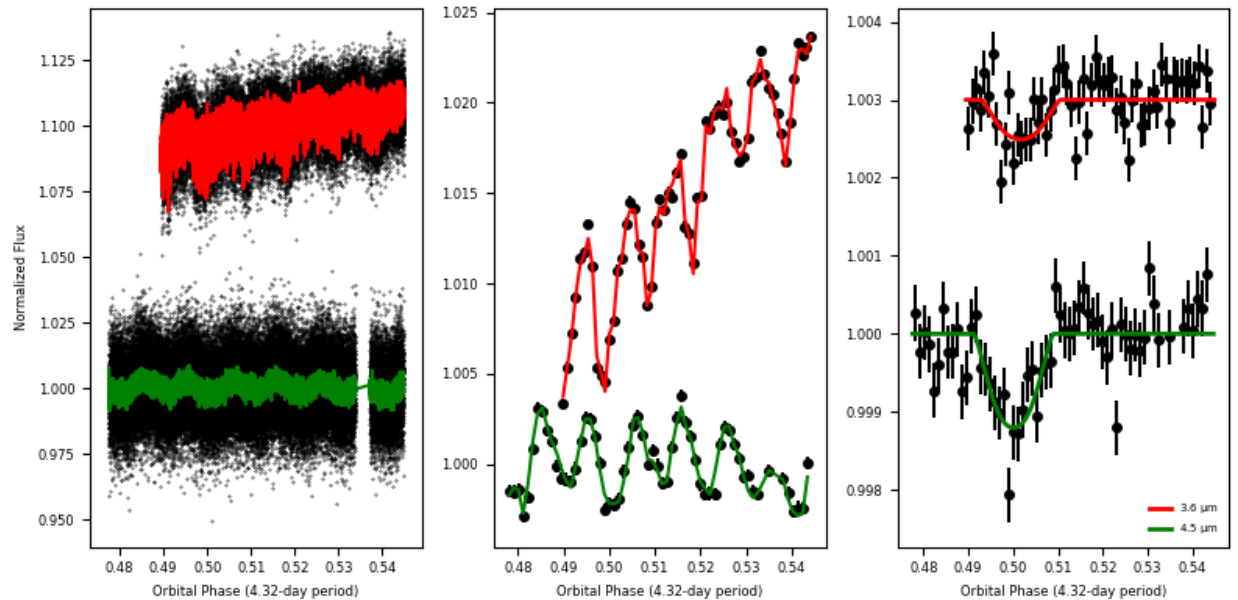
Figure 4.2: PLD light curves of WASP-34, vertically offset for visual clarity. Note that we clipped out frames 49000 – 52000 due to erratic sky levels and frames 53740 – 53790 due to a reaction wheel spike. **Left:** Normalized raw photometry with best-fit models overplotted. **Middle:** Normalized binned photometry and binned best-fit models. **Right:** Normalized binned photometry and best-fit models with systematics divided out to highlight the eclipses.

4.4.3 Joint Light-curve Modeling

In an attempt to constrain b, we jointly fit to both light curves, with both BLISS and PLD using the photometry listed in Table 4.1. We use the same model parameterization scheme as described above, but let b vary, and share b between models of the 3.6 μm and 4.5 μm eclipses. With BLISS we find $b = 0.967 \pm 0.042$, and with PLD $b = 0.957 \pm 0.044$. However, we still find eclipse depth to be largely unconstrained, so for the following orbital and atmospheric analyses, we use the fits with b fixed to 0.904.

4.5   Orbit

Eclipse observations sample a different portion of the orbit than transits, so they can significantly reduce uncertainties on eccentricity, as well as detect eccentricity false positives in radial-velocity (RV) data (Arras et al. 2012). We use an MCMC code, described by Campo et al. (2011), to fit a Keplerian orbit to the measured eclipse midpoint timings, published and amateur transit ephemerides (var2.astro.cz/ETD/, Table 4.3), and RV data (Table 4.4) from Smalley et al. (2011). None of the RV data occur during transit, so there is no need to account for the Rossiter-McLaughlin effect.

Table 4.3: WASP-34b Transit Observations

Time (BJD_{TDB})	Uncertainty (BJD_{TDB})	Reference[a]
2455739.92619	0.00117	ETD: Curtis I.
2455726.97299	0.0016	ETD: Curtis I.
2455631.97466	0.0013	ETD: Evans P.
2455580.17290	0.00116	ETD: Tan TG
2454647.55359	0.00064	Smalley et al. (2011)

[a] ETD: Exoplanet Transit Database. We require that transits have a data quality of 3 or better.

Our model includes terms for $e\cos\omega$, $e\sin\omega$, precession $\dot{\omega}$, transit ephemeris T_0, orbital period, RV semi-amplitude K, system radial velocity γ, and system radial acceleration $\dot{v}$. We find, through BIC comparison (see Equations 4.11 and 4.12), that models without precession are preferred $\sim$5:1, so we fix the precession term to 0.

We fit to both the BLISS and PLD results to check for consistency (see Table 4.5). Aside from $e\cos\omega$, the fitted parameters are within $< 0.5\sigma$, and match Smalley et al. (2011) at $< 3\sigma$, with only $e\cos\omega$ differing by $> 2.3\sigma$. Note that eccentricity and angle of periastron are derived from fitted parameters, and the asymmetric uncertainties are calculated by finding a 1σ region around the best fit of the derived MCMC posteriors, which are non-Gaussian (see Figure 4.3).

Table 4.4: WASP-34b Radial Velocity Data

Time (BJD$_{\text{TDB}}$)	RV (m/s)
2455166.8246	49790.3 ± 4.4
2455168.8191	49937.2 ± 4.3
2455170.8439	49792.3 ± 4.2
2455172.8246	49925.3 ± 4.6
2455174.8495	49814.1 ± 4.1
2455175.8487	49797.3 ± 3.9
2455176.8235	49880.6 ± 4.2
2455179.8425	49788.8 ± 4.1
2455180.8566	49861.1 ± 4.1
2455181.8219	49941.4 ± 4.2
2455182.8521	49876.5 ± 4.9
2455184.8554	49843.2 ± 4.4
2455186.8299	49905.8 ± 4.6
2455190.8509	49915.2 ± 4.5
2455261.7740	49768.6 ± 4.9
2455262.6724	49819.1 ± 4.1
2455372.5078	49873.1 ± 5.0
2455375.6020	49879.7 ± 7.0
2455376.5170	49895.6 ± 8.0
2455380.5170	49892.2 ± 4.8
2455391.4971	49763.1 ± 5.3
2455399.4719	49769.5 ± 4.8
2455403.4683	49815.9 ± 4.9
2455410.4719	49891.3 ± 4.9

Smalley et al. 2011

While the 1σ uncertainty on e indicates only a marginal detection of eccentricity, the posterior distributions show a 2–3σ detection so we investigate the expected circularization timescale for this planet and compare with the age of the system. This timescale, from Goldreich & Soter (1966), is given by

$$\tau_e = \frac{4}{63} Q \left(\frac{a^3}{GM} \right)^{1/2} \left(\frac{m}{M} \right) \left(\frac{a}{R_{\text{p}}} \right)^5,\qquad(4.19)$$
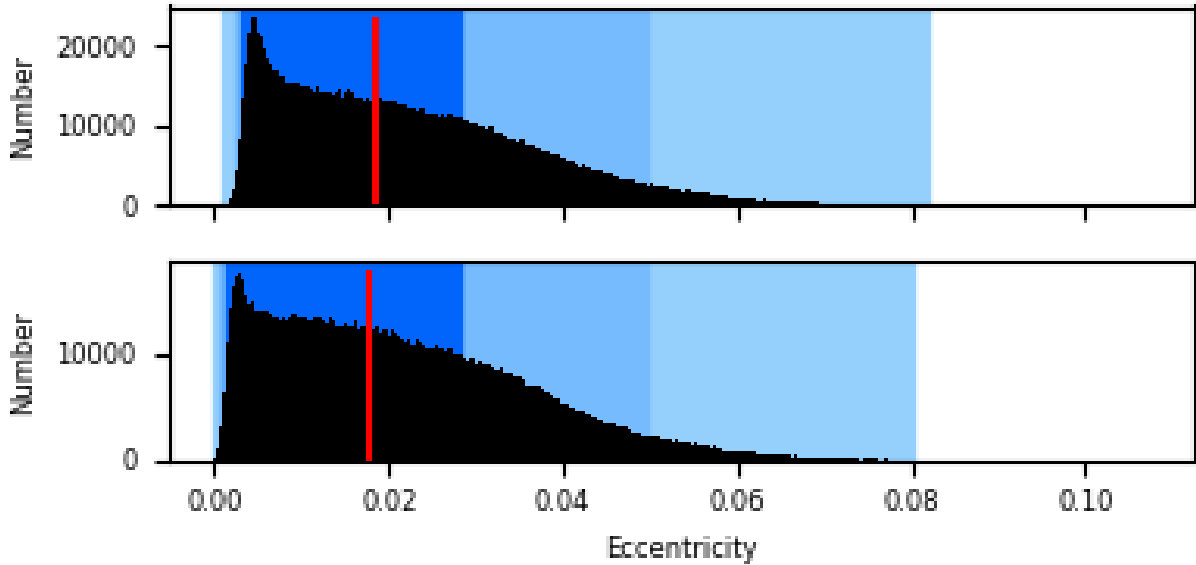
Figure 4.3: Eccentricity histograms derived from MCMC posterior distributions of $e\sin\omega$ and $e\cos\omega$. The red line marks the best-fit value, and the blue regions denote the 1, 2, and 3σ regions. **Top:** Posterior from the fit to the BLISS results. **Bottom:** Posterior from the fit to the PLD results.

where Q is a tidal dissipation factor, typically $\sim 10^6$ for hot Jupiters (Wu 2005), a is orbital radius, M is stellar mass, m is planetary mass, and R_p is planetary radius. Using $M = 1.01\ M_\odot$, $m = 0.59\ R_J$, and $a = 0.0524$ AU (Smalley et al. 2011), we determine a circularization timescale of $\sim 4 \times 10^8$ years. Smalley et al. (2011) note that lithium depletion in WASP-34 indicates an age $\gtrsim 5$ Gyr (Sestito & Randich 2005), implying that the planet's orbit should have circularized. This is consistent with our results within $\sim 2\sigma$.

Table 4.5: WASP-34b Orbital Parameters

	BLISS	PLD	Smalley et al. (2011)
Fitted Parameters			
$e \sin \omega$	-0.0180 ± 0.0184	-0.0177 ± 0.0184	-0.024 ± 0.016
$e \cos \omega$	0.0036 ± 0.0009	0.0016 ± 0.0008	0.028 ± 0.009
Period (days)	4.317670 ± 0.000004	4.317670 ± 0.000004	4.3176782 ± 0.0000045
Transit time, T_0 (BJD$_{\text{TDB}}$)	$2454647.55356 \pm 0.00064$	$2454647.55356 \pm 0.00064$	$2454647.55358 \pm 0.00064$
RV semiamplitude, K (m/s)	71.9 ± 1.2	71.9 ± 1.2	72.1 ± 1.2
system RV, γ (m/s)	49936.0 ± 6.1	49935.7 ± 6.1	49939.5 ± 6.4
system acceleration, $\dot{v}$ (m/s/yr)	-52.6 ± 3.7	-52.4 ± 3.7	-54.8 ± 4.0
Derived Parameters			
e	$0.018^{+0.010}_{-0.015}$	$0.018^{+0.010}_{-0.016}$	0.038 ± 0.012
ω (°)	$-78.7^{+9.7}_{-9.2}$	$-84.8^{+5.1}_{-5.7}$	$-40.2^{+23.2}_{-18.6}$

4.6   Atmosphere

We used our Bayesian Atmospheric Radiative Transfer code (BART, Harrington et al. 2020, Cubillos et al. 2020, Blecic et al. 2020, `https://github.com/exosports/BART`) to retrieve the atmosphere of WASP-34b. BART consists of three main packages: Transit (Rojo 2006), a radiative transfer code that produces spectra from a parameterized atmosphere model; Thermochemical Equilibrium Abundances (TEA, Blecic et al. 2016), which calculates species abundances at each pressure and temperature in a planet's atmosphere based on equilibrium chemistry; and MC[3] (Cubillos et al. 2017), an MCMC routine wrapper. BART ties these packages together to retrieve thermal profiles and abundances of atmospheric constituents from eclipse or transit observations.

BART parameterizes the planetary thermal structure with the thermal profile from Line et al. (2013). This model has five free parameters: κ_{IR}, the infrared Planck mean opacity; γ_1 and γ_2, the ratios of Planck mean opacities in the two visible streams to the infrared stream; α, which splits flux between the two visible streams; and β, which covers albedo, emissivity, and heat redistribution. We also fit logarithmic scale factors on the abundances of H_2O, CH_4, CO, and CO_2. Given the low signal-to-noise of our data and the limited spectral coverage, we use uniform abundances with respect to pressure. We include opacity from the four aforementioned molecules as well as H_2 - H_2 collision-induced absorption. For all model parameters, we use non-informative (uniform) priors with wide boundaries such that the parameter space can be fully explored. We also reject MCMC iterations that create non-physical abundances ($¿100\%$) or negative thermal profiles.

Our spectrum is only two broadband photometric filters, so models are prone to overfitting. We try several statistically- and physically-motivated cases to determine what information we can learn from our data:

1. All parameters free (κ_{IR}, γ_1, γ_2, α, β, and logarithmic scale factors for H_2O, CH_4, CO, and CO_2 abundances).

2. Since CH_4 and CO_2 are not expected to be abundant at hot-Jupiter temperatures and pressures, we fix their abundances to 6.93×10^{-6} and 1.66×10^{-7}, respectively. These are TEA-computed values at 0.1 bars pressure and the planetary equilibrium temperature of 1158 K, assuming 0 albedo and uniform heat redistribution. Thermal profile parameters and the other molecular abundances are left free to vary.

3. Same as 2. but the the CO mixing ratio is fixed to 4.53×10^{-4} (thermochemical equilibrium as in case 2), since only the 4.5 μm filter is sensitive to CO abundance.

4. Same as 3. but the H_2O mixing ratio is fixed to 3.84×10^{-6} (thermochemical equilibrium as in case 2). Only the thermal profile parameters are free to vary.

5. Same as 4. but $\alpha = 0.0$ and $\gamma_2 = 1$, removing one visible stream.

6. Same as 5. but $\beta = 1$. This sets the irradiation temperature equal to the planet's equilibrium temperature, assuming zero albedo and perfect heat redistribution.

7. An isothermal atmosphere, where planetary temperature is the only free parameter.

Case 1 represents the most flexible model, cases 2 – 4 make simplifying assumptions about the atmospheric composition, and cases 5 – 7 represent a range from complex to simple thermal profiles, all with vertically-uniform molecular abundances. All cases include the same opacity sources. As with the "ramp" in the light-curve modeling, we use the BIC to determine which model is warranted by our data (Equation 3.7, Table 4.6). We fit to both the PLD and BLISS eclipse depths, separately, to compare results.

Table 4.6: Atmospheric Fit BICs

Case	BLISS		PLD	
	BIC	P_{21}	BIC	P_{21}
1	6.2383	0.0627	6.2396	0.1299
2	4.8521	0.1253	4.8527	0.2599
3	4.1589	0.1772	4.1631	0.3633
4	3.4659	0.2506	3.9343	0.4114
5	2.0798	0.5011	2.7517	0.7432
6	1.3865	0.7088	2.1581	—
7	0.6980	—	2.8758	0.6985

The retrievals using the PLD and BLISS eclipse depths are very similar. Cases 1, 2, and 3 result in fits with unconstrained abundances for all fitted molecules, with flat MCMC posteriors, indicating that for any abundance within reasonable parameter bounds, there exists a parameter set that fits equally well. The flat posteriors and a BIC comparison show we are statistically justified in fixing the molecular abundances to thermochemical equilibrium (Table 4.6). Likewise, our data are unable to support a temperature structure as complex as case 4, with an uninformative posterior distribution for α. Cases 5, 6, and 7 have informative (non-flat) marginalized posterior distributions for their parameters, although case 5 still overfits the data. With the BLISS eclipse depths, we are only justified in fitting an isothermal atmosphere, and determine a temperature of 1100 $\pm$ 50 K (Figure 4.4, left). With the PLD depths, case 6 has the best BIC, although the posterior distribution of thermal profiles suggest a likely isothermal atmosphere with a small chance for a thermal inversion (Figure 4.4, right). Figure 4.5 shows the BIC-optimized spectra.

Following Harrington et al. (2020), we compute the Steps Per Effectively-Independent Sample (SPEIS), Effective Sample Size (ESS), and 3σ credible region accuracy to ensure we run sufficient MCMC iterations on our BIC-optimized models. Table 4.7 shows the results, which indicate high accuracy in the posterior distribution.

Table 4.7: Convergence Criteria

Light-curve Model	SPEIS	ESS	3σ Accuracy
PLD	68	1471	0.0014
BLISS	16	563	0.0022
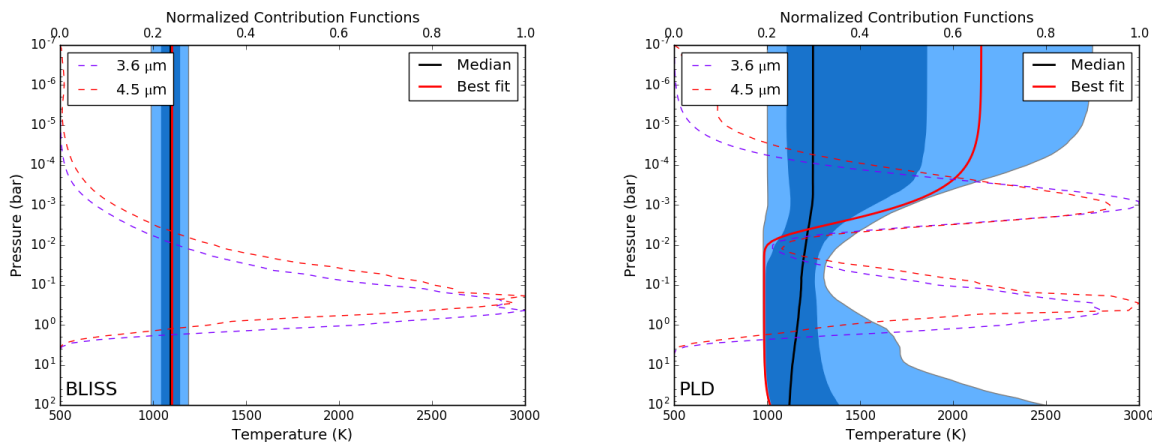
Figure 4.4: Lowest BIC BART-retrieved temperature-pressure profiles. Dark blue and light blue regions denote the 68% and 95% boundaries, respectively. We have overplotted contribution functions for the two *Spitzer* data points, which show the portion of the atmosphere probed by our retrieval. **Left:** The isothermal (case 7) profile retrieved from the BLISS eclipse depths. **Right:** The thermal profile retrieved using PLD eclipse depths (case 6).

Per the BART license, the code version, inputs, outputs, and output-processing scripts for these best-fitting atmospheres are contained in a reproducible-research compendium that can be found at `https://doi.org/10.5281/zenodo.3759978`. The compendium also includes the raw light curves used to determine the inputs to our atmospheric retrieval, our best-fitting models, and some (nominal) correlated noise diagnostics.
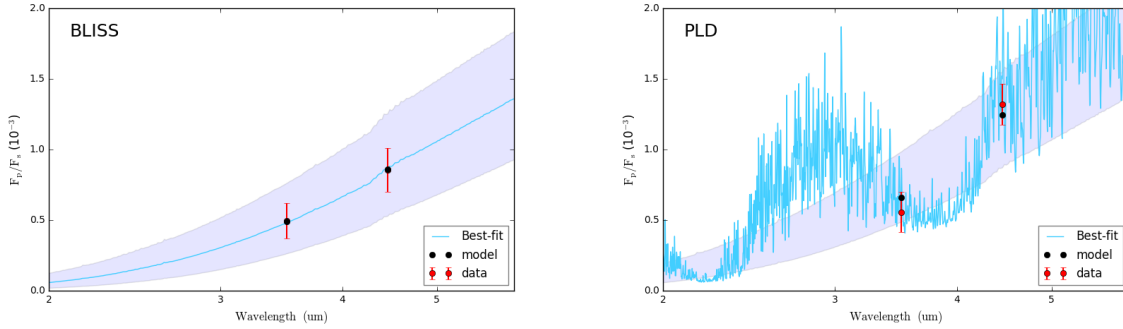
Figure 4.5: Lowest BIC (isothermal, case 7) BART-retrieved spectra as planet-to-star flux ratio. The black dots are the spectrum integrated over the filters. The black dots, not the light blue line, should match the red data. The shaded region denotes the 3σ uncertainty on the best-fit isothermal atmosphere. **Left:** Isothermal (blackbody) spectrum retrieved using the BLISS eclipse depths. Features are caused by the stellar spectrum (ATLAS9, Castelli & Kurucz 2004); the planetary spectrum is a smooth blackbody curve. **Right:** The isothermal spectrum retrieved using the PLD eclipse depths.

4.7   Conclusions

We analyzed two *Spitzer* observations of the exoplanet WASP-34b using two light-curve modeling methods, BLISS and PLD, and applying a modified eclipse model to account for the planet's high impact parameter. The resulting eclipse depths agree at $\lesssim 2\sigma$ and midpoints agree at $\lesssim 0.6\sigma$ between the two methods. By minimizing a combination of white and correlated noise, BLISS selects a fixed photometry aperture radius but PLD prefers a variable aperture radius. If the two models are forced to use the same light curve, the resulting eclipse depths more closely match.

The measured eclipse midpoints further constrained the orbit of the planet. We determined an eccentricity lower and more consistent with zero than previously reported (Smalley et al. 2011). The orbital fit results do not differ between BLISS and PLD ($< 0.6\sigma$ agreement).

We also performed atmospheric retrieval on our measured eclipse depths, separately for each light-curve modeling technique, using a series of physically-motivated cases to determine what we could learn from the data. For both BLISS and PLD, despite differences in the eclipse depths, we preferred atmospheric models that fixed molecular abundances to thermochemical equilibrium over those that fit the abundances. Thus, we cannot constrain atmospheric constituents. We find the best model, by BIC comparison, is an isothermal atmosphere at $\sim 1000 - 1100$ K.

WASP-34b is somewhat unusual, with its low density. The implied large scale height makes it an attractive target for transit studies. Unfortunately, the planet's grazing nature makes it difficult to observe and characterize. Further improvement over the atmospheric results presented here may be possible with the *Hubble Space Telescope*, at least in transit geometry, but additional eclipses to constrain the day-side atmosphere and orbit likely must wait for the *James Webb Space Telescope*.

4.8   Acknowledgments

4.9   List of References

Arras, P., Burkart, J., Quataert, E., & Weinberg, N. N. 2012, MNRAS, 422, 1761

Blecic, J., Harrington, J., & Bowman, M. O. 2016, ApJS, 225, 4

Blecic, J., Harrington, J., Cubillos, P. E., Bowman, M. O., Rojo, P., Stemm, M. M., Challener, R. C., Foster, A. J., Dobbs-Dixon, I., Foster, A. S., Lust, N. B., Blumenthal, S. D., Bruce, D., Himes, M. D., & Loredo, T. J. 2020, ApJ, in prep

Blecic, J., Harrington, J., Madhusudhan, N., Stevenson, K. B., Hardy, R. A., Cubillos, P. E., Hardin, M., Bowman, O., Nymeyer, S., Anderson, D. R., Hellier, C., Smith, A. M. S., & Collier Cameron, A. 2014, ApJ, 781, 116

Blecic, J., Harrington, J., Madhusudhan, N., Stevenson, K. B., Hardy, R. A., Cubillos, P. E., Hardin, M., Campo, C. J., Bowman, W. C., Nymeyer, S., Loredo, T. J., Anderson, D. R., & Maxted, P. F. L. 2013, ApJ, 779, 5

Campo, C. J., Harrington, J., Hardy, R. A., Stevenson, K. B., Nymeyer, S., Ragozzine, D., Lust, N. B., Anderson, D. R., Collier-Cameron, A., Blecic, J., Britt, C. B. T., Bowman, W. C., Wheatley, P. J., Loredo, T. J., Deming, D., Hebb, L., Hellier, C., Maxted, P. F. L., Pollaco, D., & West, R. G. 2011, ApJ, 727, 125

Castelli, F. & Kurucz, R. L. 2004, ArXiv Astrophysics e-prints

Challener, R. C., Harrington, J., Jenkins, J. S., Kurtovic, N. T., Ramirez, R., Peña, J., McIntyre, K. J., Himes, M. D., Rodríguez, E., Anglada-Escudé, G., Dreizler, S., Ofir, A., Peña Rojas, P. A., Ribas, I., Rojo, P., Kipping, D., Butler, R. P., Amado, P. J., Rodríguez-López, C., Kempton, E. M. R., Palle, E., & Murgas, F. 2020, ApJ,, in prep

Charbonneau, D., Allen, L. E., Megeath, S. T., Torres, G., Alonso, R., Brown, T. M., Gilliland, R. L., Latham, D. W., Mandushev, G., O'Donovan, F. T., & Sozzetti, A. 2005, ApJ, 626, 523

Cubillos, P., Harrington, J., Loredo, T. J., Lust, N. B., Blecic, J., & Stemm, M. 2017, AJ, 153, 3

Cubillos, P., Harrington, J., Madhusudhan, N., Foster, A. S. D., Lust, N. B., Hardy, R. A., & Bowman, M. O. 2014, ApJ, 797, 42

Cubillos, P., Harrington, J., Madhusudhan, N., Stevenson, K. B., Hardy, R. A., Blecic, J., Anderson, D. R., Hardin, M., & Campo, C. J. 2013, ApJ, 768, 42

Cubillos, P. E., Harrington, J., Blecic, J., Himes, M. D., Rojo, P. M., Loredo, T. J., Lust, N. B., Challener, R. C., Foster, A. J., Stemm, M. M., Foster, A. S., & Blumenthal, S. D. 2020, ApJ, in prep

Deming, D., Knutson, H., Kammer, J., Fulton, B. J., Ingalls, J., Carey, S., Burrows, A., Fortney, J. J., Todorov, K., Agol, E., Cowan, N., Desert, J.-M., Fraine, J., Langton, J., Morley, C., & Showman, A. P. 2015, ApJ, 805, 132

Fazio, G. G., Hora, J. L., Allen, L. E., Ashby, M. L. N., Barmby, P., Deutsch, L. K., Huang, J.-S., Kleiner, S., Marengo, M., Megeath, S. T., Melnick, G. J., Pahre, M. A., Patten, B. M., Polizotti, J., Smith, H. A., Taylor, R. S., Wang, Z., Willner, S. P., Hoffmann, W. F., Pipher, J. L., Forrest, W. J., McMurty, C. W., McCreight, C. R., McKelvey, M. E., McMurray, R. E., Koch, D. G., Moseley, S. H., Arendt, R. G., Mentzell, J. E., Marx, C. T., Losch, P., Mayman, P., Eichhorn, W., Krebs, D., Jhabvala, M., Gezari, D. Y., Fixsen, D. J., Flores, J., Shakoorzadeh, K., Jungo, R., Hakun, C., Workman, L., Karpati, G., Kichak, R., Whitley, R., Mann, S., Tollestrup, E. V., Eisenhardt, P., Stern, D., Gorjian, V., Bhattacharya, B., Carey, S., Nelson, B. O., Glaccum, W. J., Lacy, M., Lowrance, P. J., Laine, S., Reach, W. T., Stauffer, J. A., Surace, J. A., Wilson, G., Wright, E. L., Hoffman, A., Domingo, G., & Cohen, M. 2004, ApJS, 154, 10

Gelman, A. & Rubin, D. B. 1992, Statistical Science, 7, 457

Gibson, N. P., Aigrain, S., Roberts, S., Evans, T. M., Osborne, M., & Pont, F. 2012, MNRAS, 419, 2683

Goldreich, P. & Soter, S. 1966, Icarus, 5, 375

Hardy, R. A., Harrington, J., Hardin, M. R., Madhusudhan, N., Loredo, T. J., Challener, R. C., Foster, A. S. D., Cubillos, P. E., & Blecic, J. 2017, ApJ, 836, 143

Harrington, J., Himes, M. D., Cubillos, P. E., Blecic, J., Rojo, P. M., Challener, R. C., Lust, N. B., Bowman, M. O., Blumenthal, S. D., Dobbs-Dixon, I., Foster, A. S., Foster, A. J., Green, M., Loredo, T. J., McIntyre, K. J., & Stemm, M. M. 2020, ApJ, in prep

Ingalls, J. G., Krick, J. E., Carey, S. J., Stauffer, J. R., Lowrance, P. J., Grillmair, C. J., Buzasi, D., Deming, D., Diamond-Lowe, H., Evans, T. M., Morello, G., Stevenson, K. B., Wong, I., Capak, P., Glaccum, W., Laine, S., Surace, J., & Storrie-Lombardi, L. 2016, AJ, 152, 44

Lewis, N. K., Knutson, H. A., Showman, A. P., Cowan, N. B., Laughlin, G., Burrows, A., Deming, D., Crepp, J. R., Mighell, K. J., Agol, E., Bakos, G. Á., Charbonneau, D., Désert, J.-M., Fischer, D. A., Fortney, J. J., Hartman, J. D., Hinkley, S., Howard, A. W., Johnson, J. A., Kao, M., Langton, J., & Marcy, G. W. 2013, ApJ, 766, 95

Line, M. R., Wolf, A. S., Zhang, X., Knutson, H., Kammer, J. A., Ellison, E., Deroo, P., Crisp, D., & Yung, Y. L. 2013, ApJ, 775, 137

Lust, N. B., Britt, D., Harrington, J., Nymeyer, S., Stevenson, K. B., Ross, E. L., Bowman, W., & Fraine, J. 2014, PASP, 126, 1092

Mandel, K. & Agol, E. 2002, ApJ, 580, L171

Morello, G., Waldmann, I. P., Tinetti, G., Howarth, I. D., Micela, G., & Allard, F. 2015, ApJ, 802, 117

Nymeyer, S., Harrington, J., Hardy, R. A., Stevenson, K. B., Campo, C. J., Madhusudhan, N., Collier-Cameron, A., Loredo, T. J., Blecic, J., Bowman, W. C., Britt, C. B. T., Cubillos, P., Hellier, C., Gillon, M., Maxted, P. F. L., Hebb, L., Wheatley, P. J., Pollacco, D., & Anderson, D. R. 2011, ApJ, 742, 35

Raftery, A. E. 1995, Sociological Mehodology, 25, 111

Rojo, P. M. 2006, PhD thesis, Cornell University

Sestito, P. & Randich, S. 2005, A&A, 442, 615

Smalley, B., Anderson, D. R., Collier Cameron, A., Hellier, C., Lendl, M., Maxted, P. F. L., Queloz, D., Triaud, A. H. M. J., West, R. G., Bentley, S. J., Enoch, B., Gillon, M., Lister, T. A., Pepe, F., Pollacco, D., Segransan, D., Smith, A. M. S., Southworth, J., Udry, S., Wheatley, P. J., Wood, P. L., & Bento, J. 2011, A&A, 526, A130

Stevenson, K. B., Harrington, J., Fortney, J. J., Loredo, T. J., Hardy, R. A., Nymeyer, S., Bowman, W. C., Cubillos, P., Bowman, M. O., & Hardin, M. 2012, ApJ, 754, 136

Werner, M. W., Roellig, T. L., Low, F. J., Rieke, G. H., Rieke, M., Hoffmann, W. F., Young, E., Houck, J. R., Brandl, B., Fazio, G. G., Hora, J. L., Gehrz, R. D., Helou, G., Soifer, B. T., Stauffer, J., Keene, J., Eisenhardt, P., Gallagher, D., Gautier, T. N., Irace, W., Lawrence, C. R., Simmons, L., Van Cleve, J. E., Jura, M., Wright, E. L., & Cruikshank, D. P. 2004, ApJS, 154, 1

Wu, Y. 2005, ApJ, 635, 688

CHAPTER 5: A REANALYSIS OF SPITZER GJ 436B EMISSION

Ryan C. Challener[1]**, Joseph Harrington**[1]**, and Zacchaeus Scheffer**[1]

[1] *Planetary Sciences Group, Department of Physics, University of Central Florida, Orlando, FL 32816-2385*

5.1 Abstract

Here we present a reanalysis of all *Spitzer* eclipse observations of GJ 436b, leveraging elliptical-aperture photometry and applying both BLISS and PLD modeling methods to minimize correlated noise in our light curves. By combining these techniques and more recent observations, we achieve comparable or better signal-to-noise ratios than previous works, and find general agreement between our light-curve modeling results. Using RadVel, we performed an orbital analysis, combining our eclipse timings with our measured phase curve transit times, transit times from the literature, amateur transit observations, and radial velocity data from the literature. We find an orbital period of $2.643898036 \pm 6.7 \times 10^{-7}$ days and an eccentricity of 0.1729 ± 0.0052. Using the Bayesian Atmospheric Radiative Transfer code, we retrieve the day-side atmosphere of the planet, and determine a non-inverted thermal profile in chemical disequilibrium. While we measure a lower 3.6 μm emission, the undetectable 4.5 μm emission still implies a CO/CO_2-dominated atmosphere depleted in methane, confirming past works (Stevenson et al. 2010, Lanotte et al. 2014, Morley et al. 2017).

5.2 Introduction

Transiting exoplanets provide an excellent opportunity for planetary characterization. As a planet passes in front of its host star, the system's flux is modulated by the cross-sectional area of the planet. Molecules in the planet's terminator adjust the atmosphere's opacity with wavelength, so observing transits spectroscopically or with a range of photometric filters can inform atmospheric composition and temperature models (e.g., Deming et al. 2013, Stevenson et al. 2014c, Morello et al. 2015). When the planet passes behind the star, the system flux decreases by an amount equal to the planet's emission. This "eclipse" geometry similarly provides atmospheric information, but of the planet's day side (e.g., Knutson et al. 2008, Anderson et al. 2011, Stevenson et al. 2014b).

As the first Neptune-sized exoplanet discovered (Butler et al. 2004), and one of the few such planets amenable to atmospheric characterization, GJ 436b is a prime target for observation. Gillon et al. (2007b) identified GJ 436b as a transiting planet, and soon after *Spitzer* detected the first eclipse (Demory et al. 2007, Deming et al. 2007). Further observations revealed unusual atmospheric chemistry (Stevenson et al. 2010), a cloudy upper atmosphere (Knutson et al. 2014), hydrogen outflow (Ehrenreich et al. 2015), and a misaligned spin axis with its host star (Bourrier et al. 2018). Ballard et al. (2010b) and Stevenson et al. (2012b) discuss the potential for additional small planets in the system, although further analyses and observations have contradicted these detections (Ballard et al. 2010a, Stevenson et al. 2014a, Lanotte et al. 2014).

The atmospheric composition of GJ 436b has been a subject of discussion. Stevenson et al. (2010) found strong 3.6 μm emission and low 4.5 μm emission, requiring an atmosphere in disequilibrium with an elevated CO abundance and a low CH_4 abundance. Further analysis with additional data by Lanotte et al. (2014), found weaker 3.6 μm emission but still favor a methane-depleted, CO/CO_2-rich atmosphere. Clouds can obscure molecular absorption features in exoplanet atmospheres, especially in transmission (e.g., Knutson et al. 2014, Kreidberg et al. 2014), although Morley et al.

(2017) showed that a cloudy atmosphere cannot replicate GJ 436b emission observations. Similar atmospheres have been proposed for the super-Earth GJ 1214b (Miller-Ricci Kempton et al. 2012) and GJ 3470b (Benneke et al. 2019), although the mechanism for methane destruction is not clear (Line et al. 2011, Miller-Ricci Kempton et al. 2012). The metallicity of GJ 436b may be several orders of magnitude greater than solar metallicity (Moses et al. 2013, Morley et al. 2017).

These conclusions hinge on a small number of measurements of weak signals buried in noise. Since the discovery of GJ 436b, methods of analyzing *Spitzer* InfraRed Array Camera (IRAC, Fazio et al. 2004) have evolved dramatically. Methods like BiLinearly Interpolated Subpixel Sensitivity maps (BLISS, Stevenson et al. 2012a) and Pixel-Level Decorrelation (PLD, Deming et al. 2015) minimize the impact of intrapixel gain variation (Charbonneau et al. 2005), and photometry techniques like variable-radius circular-aperture photometry (Lewis et al. 2013) and elliptical-aperture photometry (Challener et al. 2020c) correct for changes in the shape of the instrument's point-spread function (PSF). Together, these methods have pushed IRAC far beyond its design criteria. GJ 436b is one of the smallest, coldest planets observed with *Spitzer*, so techniques like these are crucial to disentangling the planet's emission signal from the noise.

In this work, we reanalyze all existing *Spitzer* emission observations using the aforementioned methods. Section 5.3 introduces the observations, Section 5.4 describes our light-curve modeling process, Section 5.5 presents our orbital fitting, Section 5.6 shows our atmospheric retrieval, and Section 5.7 lays out our conclusions.

5.3 Observations

There is a plethora of emission data of GJ 436b, including measurements with the 5.8, 8.0, 16, and 24 μm *Spitzer* channels that have been non-functional since the telescope's cryogen was exhausted in 2009. The 16 μm channel is the blue peak-up camera of the InfraRed Spectrograph (IRS) and the 24 μm channel is a filter of the Mid-Infrared Photometer for *Spitzer* (MIPS). Table 5.1 lists the eclipse and phase curve observations available. Some GJ 436b observations in the *Spitzer* Heritage Archive are actually part of a search for transits of a second planet, GJ 436c, and do not contain GJ 436b events; they are marked as such in the table.

Table 5.1: *Spitzer* Observations of GJ 436 Emission

Wavelength (µm)	Visit	Obs. Start	Obs. End	Program	PI	Notes
Eclipses						
3.6	1	2008-01-30 19:07:32	2008-01-31 01:04:24	40685	Harrington, J.	
3.6	2	2010-06-23 17:37:08	2010-06-23 23:35:15	60003	Harrington, J.	Transit search. No eclipse.
3.6	3	2011-02-01 01:27:35	2011-02-01 07:36:12	60003	Harrington, J.	
3.6	4	2014-07-29 10:57:42	2014-07-29 15:24:41	10054	Knutson, H.	
4.5	1	2008-02-02 10:41:12	2008-02-02 16:36:57	40685	Harrington, J.	
4.5	2	2010-06-29 00:28:44	2010-06-29 06:31:04	60003	Harrington, J.	Transit search. No eclipse.
4.5	3	2011-01-24 02:44:54	2011-01-24 08:53:26	60003	Harrington, J.	
4.5	4	2014-08-11 16:10:54	2014-08-11 20:37:53	10054	Knutson, H.	
4.5	5	2015-02-25 23:17:06	2015-02-26 03:44:05	10054	Knutson, H.	
4.5	6	2010-01-28 06:41:00	2010-01-29 00:42:11	541	Ballard, S.	Transit search. No eclipse.
5.8	1	2008-02-05 01:52:46	2008-02-05 07:48:31	40685	Harrington, J.	
8.0	1	2007-06-30 15:32:03	2007-06-30 21:27:48	30129	Harrington, J.	
8.0	2	2008-06-11 01:30:56	2008-06-11 04:59:07	50734	Laughlin, G.	
8.0	3	2008-06-13 17:06:37	2008-06-13 20:34:50	50734	Laughlin, G.	
8.0	4	2008-06-16 08:48:26	2008-06-16 12:13:29	50734	Laughlin, G.	
8.0	5	2008-06-19 00:29:08	2008-06-19 03:57:19	50734	Laughlin, G.	
8.0	6	2009-01-27 02:46:46	2009-01-27 06:20:29	50734	Laughlin, G.	
8.0	7	2009-01-29 18:09:27	2009-01-29 21:42:52	50734	Laughlin, G.	
8.0	8	2009-02-01 09:29:42	2009-02-01 12:54:45	50734	Laughlin, G.	
8.0	9	2009-02-04 00:55:31	2009-02-04 04:29:05	50734	Laughlin, G.	
16	1	2008-01-12 06:49:07	2008-01-12 12:48:49	40685	Harrington, J.	
24	1	2008-01-04 08:38:14	2008-01-04 14:14:28	40685	Harrington, J.	
Phase Curves (two eclipses each)						
3.6	1	2018-08-31 06:00:28	2018-09-03 02:01:56	13234	Parmentier, V.	
8.0	1	2008-07-12 18:39:54	2008-07-15 16:47:22	50056	Knutson, H.	

5.4   Light-curve Modeling

We use our Photometry for Orbits, Eclipses, and Transits code (POET, e.g., Nymeyer et al. 2011, Stevenson et al. 2010, 2012a, Blecic et al. 2013, Cubillos et al. 2013, Blecic et al. 2014, Cubillos et al. 2014a, Hardy et al. 2017) for all analyses herein. When producing light curves, we use several different centering and photometry methodologies, in all possible combinations. For a full description of our methods, see Challener et al. (2020a) and Challener et al. (2020b). In brief, we apply the following techniques: Gaussian, least asymmetry (Lust et al. 2014), and center-of-light centering; fixed-circle aperture, variable-circle aperture (Lewis et al. 2013), and elliptical-aperture photometry (Challener et al. 2020c); flat, linear, quadratic, and exponential baseline ("ramp") models; and BLISS maps (Stevenson et al. 2012a) and PLD (Deming et al. 2015) intrapixel (IP) gain variation modeling methods.

To produce light curves, POET performs $5\times$-interpolated, flux-conserving aperture photometry. For fixed-radius circular apertures we use aperture radii from $1.5 - 4.0$ pixels in increments of 0.25. For variable-radius circular apertures, we define aperture radii by

$$R_{\mathrm{var}} = a\sqrt{N} + b \qquad\qquad (5.1)$$

where a is a scale factor from $0.5 - 1.5$ in steps of 0.25, b is an offset from $-1 - 2.0$ pixels in steps of 0.5 pixels, and N is the noise pixel parameter, which varies frame to frame (Lewis et al. 2013). With elliptical apertures, we describe the ellipse with two radii given by

$$R_{\text{ell,x}} = a\sigma_x + b$$

$$R_{\text{ell,y}} = a\sigma_y + b \tag{5.2}$$

where σ_x and σ_y are 1σ Gaussian-fit widths of the point-spread function (PSF) in the x and y dimensions, a is a scale from $3 - 7$ in steps of 1, and b is an offset from $-1 - 2.0$ pixels in steps of 0.5 pixels.

The general form of the light curve model used with BLISS is given by

$$F(x, y, t) = F_s A(t) R(t) M(x, y), \tag{5.3}$$

where F_s is the out-of-eclipse system flux, $A(t)$ is a set of astrophysical effect models, $R(t)$ is a ramp model, and $M(x, y)$ is the BLISS map. For all fits, we set the BLISS map subpixel gridding size to the root-mean-square of the point-to-point variation in the x and y position of the target found by our centering methods, and we require that every BLISS grid cell contain at least four frames.

The PLD light-curve model is described by

$$F(t) = F_s \left(\sum_{i=1}^{n_p} c_i P_i + R(t) + A(t) \right), \tag{5.4}$$

where P_i is the time-dependent normalized flux of pixel i, c_i are free parameter pixel weights, and n_p is the number of pixels considered. In this work we use the nine brightest pixels of the mean frame. With PLD, we find that F_s is degenerate with the c_i parameters so we fix it equal to the average flux.

The flat, linear, quadratic, and exponential ramp models are given by

$$R(t) = r_0, \tag{5.5}$$

$$R(t) = r_1(t - t_0) + r_0, \tag{5.6}$$

$$R(t) = r_2(t - t_0) + r_1(t - t_0) + r_0, \tag{5.7}$$

$$R(t) = r_1(1 - \exp(-m(t - t_0))), \tag{5.8}$$

respectively. The flat, linear, and quadratic models are used for individual eclipse observations (not phase curves), where we set $t_0 = 0.5$ orbital phase. In phase curves, the ramp effect occupies a comparatively small portion of the observation, so in those cases we use the exponential model. For BLISS models, since they are multiplicative, we set $r_0 = 1$, and similarly we set $r_0 = 0$ for the additive PLD models.

The astrophysical model $A(t)$ contains up to four terms depending on the observation: a uniform-source Mandel & Agol (2002) eclipse model, a small-planet non-linear limb-darkening transit model also from Mandel & Agol (2002), and a phase curve variation model. The eclipse model has parameters for eclipse midpoint t_{ecl}, eclipse duration t_{14}, eclipse depth D, ingress time t_{12}, and egress time t_{34}. For all observations we set $t_{12} = t_{34} = 0.04025$ orbital phase, and set a lower limit on t_{14} of 0.0805 orbital phase to prevent non-physical models. When fitting light curves and quoting ephemerides in orbital phase, we assume 0.0 phase corresponds to a transit at time 2454603.33657 BJD and an orbital period of 2.64389579 days (Ballard et al. 2010b).

The transit model has free parameters for transit midpoint t_{tr}, inclination in the form $\cos i$, orbital semimajor axis a/R_*, orbital period P, and four non-linear limb-darkening parameters a_1, a_2, a_3, and a_4. We set $a/R_* = 14.34$ and $P = 2.64389579$ days. At 3.6 µm we set $a_1 = 1.0167$, $a_2 = -1.5347$, $a_3 = 1.2885$, and $a_4 = -0.4205$. For 8.0 µm we set $a_1 = 0.7141$, $a_2 = -0.9971$, $a_3 = 0.7839$, and $a_4 = -0.2421$. These values are taken from Claret & Bloemen (2011) assuming a stellar effective temperature of 3500 K, $\log(g)$ of 5.0, and metallicity of -0.3 (von Braun et al. 2012).

For the phase-curve variation, following Stevenson et al. (2017) we use an asymmetric cosine of the form

$$P(t) = A_1 \cos\left[2\pi(t - t_1)/P\right] + A_2 \cos\left[4\pi(t - t_2)/P\right], \qquad (5.9)$$

where A_1 and A_2 are phase-curve variation amplitudes, t_1 and t_2 are orbital phases of the peak amplitudes, and P is the planet's orbital period. The two cosines allow for asymmetry, which may be important for an orbit as eccentric as that of GJ 436b. We set $P = 2.64389579$ days for the light-curve fits and address the orbit further in Section 5.5.

We choose between combinations of centering and photometry methods by minimizing χ^2_{bin}(Deming et al. 2015, Challener et al. 2020a,b) of our model fits, a statistic that minimizes noise over a broad range of frequencies. We select the ramp model by minimizing the Bayesian Information Criterion (BIC, Raftery 1995), a statistic that penalizes models with more free parameters, given by

$$\mathrm{BIC} = \chi^2 + k \ln N_{\mathrm{data}}, \tag{5.10}$$

where k is the number of free parameters in the model, and N_{data} is the number of data points. Since BIC cannot be used to compare across centering and photometry combinations (effectively different data sets), optimizing these decisions is an iterative process. First, we determine the ramp model by comparing the BICs of each ramp when applied to a light curve from Gaussian centering and 2.5-pixel radius fixed-circle aperture photometry. Then we apply that ramp model to every centering and photometry method combination, and select by minimizing χ^2_{bin}. If a BIC comparison of each ramp model on this new light curve confirms that we still have chosen the optimal ramp, we accept this light curve as optimal; otherwise, we repeat the χ^2_{bin} optimization and ramp model check until we converge to an optimal light curve. In all cases, two iterations of this process was sufficient.

PLD utilizes binning to reduce correlated noise. We bin the data by 1 (no binning), 2, 4, 8, 16, 32, 64, 128, and 256 frames per bin, and choose that which results in the lowest χ^2_{bin}. All BIC comparisons are done without binning, as the BIC is dependent on the number of data points.

The general modeling process is:

1. Inspect centering positions to determine if any frames should be discarded due to reaction wheel spikes (when *Spitzer* transfers momentum between reaction wheels during the observation) or on-board processing errors (shifts in the image).

2. Fit a light-curve model to Gaussian-centered 2.5-pixel radius fixed-circle aperture photometry. Determine if any frames in the beginning of the observation should be discarded to minimize the telescope settling effect.

3. Fit each ramp model to the same photometry, and use a BIC comparison to choose the optimal one.

4. Fit the model with the optimal ramp to all light curves produced by each combination of centering and photometry methods. Choose the combination that results in the lowest $\chi^2_{\rm bin}$. With PLD, also choose the optimal bin size in this step.

5. Compare ramp model BICs on the chosen light curve. If the same model is selected as in step 3, accept this light curve as optimal. If not, repeat steps 4 and 5.

For the final model fits, we rescale our photometry uncertainties such that the model reduced χ^2 is 1. However, steps 3 and 5 must be done without uncertainty rescaling, as the BIC calculation depends on χ^2.

Once an optimal light curve is chosen, we use least-squares optimization to determine the best-fitting model, and Multi-Core Markov Chain Monte Carlo (MC^3, Cubillos et al. 2017) to explore the model parameter posterior distribution to determine parameter uncertainties. In all Markov-Chain Monte Carlo (MCMC) applications, we run enough iterations that our chains pass the Gelman & Rubin test within 1% of unity, to ensure the posterior distribution is thoroughly explored

(Gelman & Rubin 1992). The light-curve model parameters with uncertainties are listed in Table 5.2. As mentioned by Deming et al. (2015), PLD is ineffective for long observations like phase curves, so we model the full phase curves with BLISS and break those observations into smaller portions for PLD modeling. In the following sections we describe the modeling process for each light curve in further detail.

Table 5.2: Light-curve Model Results

Filter (μm)	Visit	IP Model + bin size	Cent. Method[a]	Phot. Method[b]	Ramp	Midpoint (phase)	Midpoint (MBJD$^c_{\text{TDB}}$)	Depth (ppm)	Duration (phase)	Preclip[d] (%)
Individual Eclipses										
3.6	1	BLISS	L	V0.50+0.5	None	0.5855(011)	4496.48567(0290)	179(071)	0.0127(30)	10
		PLD(32)	C	F2.50	None	0.5882(006)	4496.49283(0153)	222(028)	0.0214(10)	10
3.6	4	BLISS	G	E5.00-0.5	Quad.	0.5926(005)	6868.07879(0125)	305(068)	0.0106(15)	0
		PLD(32)	L	V0.75+1.0	Quad.	0.5923(024)	6868.07813(0646)	351(091)	0.0105(63)	0
4.5	1	BLISS	L	F2.00	Quad.	0.5839(045)	4499.12522(0674)	198(072)	0.0087(57)	0
		PLD(64)	C	F3.00	Quad.	0.5828(080)	4499.12238(2104)	184(062)	0.0084(64)	0
4.5	3	BLISS	G	V0.75-0.5	None	0.5740(093)	5585.74037(2775)	29(045)	0.0084(64)	20
		PLD(16)	G	E6.00+2.0	Lin.	0.5823(133)	5585.76225(3524)	73(033)	0.0084(65)	20
4.5	4	BLISS	G	E4.00+0.5	None	0.5949(033)	6881.30441(0868)	107(057)	0.0219(56)	0
		PLD(64)	C	V0.50+1.0	Quad.	0.5909(085)	6881.29385(2237)	163(068)	0.0145(98)	0
4.5	5	BLISS	G	V0.50+1.5	None	0.5858(027)	7079.57260(0831)	83(041)	0.0092(40)	0
		PLD(8)	C	V1.50-0.5	Quad.	0.5923(012)	7079.58976(0306)	226(048)	0.0269(20)	0
5.8	1	BLISS	G	E5.00+1.0	Quad.	0.5940(065)	4501.79592(1620)	288(124)	0.0300(66)	20
		PLD(32)	L	V1.50+1.0	Quad.	0.5861(110)	4501.77492(2902)	255(139)	0.0139(66)	20
8.0	1	BLISS	L	F2.25	Quad.	0.5872(007)	4282.33453(0179)	647(085)	0.0191(16)	10
		PLD(128)	L	V0.50+1.5	Quad.	0.5865(006)	4282.33271(0161)	857(089)	0.0199(15)	10
8.0	2	BLISS	C	V1.50+1.5	Quad.	0.5869(020)	4628.68412(0348)	551(158)	0.0167(38)	0
		PLD(32)	L	V1.50+2.0	Quad.	0.5870(021)	4628.68431(0566)	574(171)	0.0165(42)	0
8.0	3	BLISS	C	V0.50+2.0	Lin.	0.5864(017)	4631.32678(0323)	341(111)	0.0155(25)	15
		PLD(4)	L	V1.50+0.0	Lin.	0.5869(026)	4631.32786(0689)	357(117)	0.0162(48)	15
8.0	4	BLISS	G	V1.00+0.0	Quad.	0.5867(020)	4633.97148(0431)	731(183)	0.0191(37)	0
		PLD(16)	C	V1.50+2.0	Quad.	0.5875(012)	4633.97337(0306)	804(145)	0.0187(24)	0
8.0	5	BLISS	L	V1.50+1.0	Lin.	0.5879(046)	4636.61829(0840)	208(102)	0.0162(38)	15
		PLD(64)	L	V1.50+0.5	Lin.	0.5941(062)	4636.63507(1650)	549(188)	0.0286(41)	15
8.0	6	BLISS	L	V1.25+1.5	Lin.	0.5887(053)	4858.70792(0943)	183(108)	0.0171(47)	20
		PLD(4)	L	V1.25+0.5	Lin.	0.5884(052)	4858.70693(1362)	187(095)	0.0176(62)	20
8.0	7	BLISS	G	V1.50+0.0	Lin.	0.5871(025)	4861.34733(0495)	275(104)	0.0172(35)	15

Filter (µm)	Visit	IP Model + bin size	Cent. Method[a]	Phot. Method[b]	Ramp	Midpoint (phase)	Midpoint (MBJD$^c_{\mathrm{TDB}}$)	Depth (ppm)	Duration (phase)	Preclip[d] (%)
		PLD(4)	C	V1.25+1.5	Lin.	0.5871(075)	4861.34741(1985)	257(129)	0.0172(48)	15
8.0	8	BLISS	G	F4.00	Quad.	0.5882(009)	4863.99421(0228)	534(108)	0.0215(18)	15
		PLD(1)	G	E5.00+1.5	Quad.	0.5872(016)	4863.99162(0430)	523(117)	0.0191(30)	15
8.0	9	BLISS	G	F3.50	Lin.	0.5849(034)	4866.62937(0724)	437(128)	0.0084(46)	15
		PLD(32)	C	V1.50+1.0	Lin.	0.5904(029)	4866.64396(0774)	369(179)	0.0187(61)	15
16	1	BLISS	C	F2.50	Lin.	0.5866(006)	4477.98123(0149)	2235(346)	0.0120(16)	25
		PLD(8)	G	E7.00+2.0	None	0.5839(018)	4477.97399(0487)	2345(640)	0.0139(36)	25
24	1	BLISS	L	F2.00	Lin.	0.5881(047)	4470.05344(1017)	1369(629)	0.0192(61)	0
		PLD(1)	L	F2.25	Lin.	0.5879(060)	4470.05311(1581)	1550(701)	0.0198(48)	0

[a] G = Gaussian fitting, L = least-asymmetry fitting, C = center-of-light.

[b] F = fixed-radius circular apertures, V = variable-radius circular apertures, E = elliptical apertures. For fixed-radius circular apertures, we list the aperture radius in pixels. For variable-radius circular and elliptical apertures we list the aperture scale a and offset b as $a + b$ (see Equations 5.1 and 5.2).

[c] Modified Barycentric Julian Date = BJD - 2,450,000

[d] Percentage of frames discarded at the start of the observation.

5.4.1 3.6 µm

In the first observation, Stevenson et al. (2010) elected to not model the portion of the light curve after the eclipse due to possible stellar activity. In agreement with Lanotte et al. (2014), we find this feature to be a systematic effect related to aperture size, and we are able to minimize its impact with elliptical apertures.

The second 3.6 µm observation is part of the transit search for GJ 436c, and does not coincide with any transit or eclipse events of GJ 436b. While the third 3.6 µm observation is also part of the GJ 436c transit search, a GJ 436b eclipse should be present. However, despite advancements in analysis techniques, we find the same stellar activity reported by Stevenson et al. (2012b). Neither BLISS nor PLD can recover the eclipse.

The final 3.6 µm observation also contains unexplained features during the eclipse. Elliptical photometry is able to mitigate them enough to model the eclipse, suggesting telescope vibration is the cause.

5.4.2 4.5 µm

In agreement with past works, our 4.5 µm light-curve models all show very weak eclipses (most $\lesssim 3\sigma$ detections). Many of the eclipses are best fit by the minimum eclipse duration, but that is simply a symptom of the low signal-to-noise ratio (S/N). By later jointly fitting all the light curves simultaneously, we are able to leverage the higher S/N observations to constrain the eclipse midpoint and duration, which then enables us to constrain the 4.5 µm eclipse depth.

Like the second visit at 3.6 μm, the second 4.5 μm observation is part of the transit search for GJ 436c, and we do not include it in this analysis. The third 4.5 μm visit is also part of that search, but coincides with an eclipse of GJ 436b.

5.4.3   5.8 μm

The lone eclipse observation with this channel is very weak, with a S/N of ~2.

5.4.4   8.0 μm

The nine eclipse observations at 8.0 μm offer the strongest emission detection. In visit 4, there is a negative feature prior to the eclipse that interferes with fitting, and is not removed by BLISS, PLD, or our photometry methods, so we discarded frames 14,000 − 16,000.

5.4.5   16 μm

For this observation, we elected to not use a BLISS map, as there is little evidence for IP gain variation. A fit with the BLISS map improves the BIC by ~ 125 but would incur a BIC penalty of > 350 if all the BLISS map knots are considered free parameters. While a BLISS map improves the fit, we are not justified in using it. Therefore, the BLISS fits to this dataset are simply a stellar flux modulated by a ramp model and an eclipse model. With PLD, we restrict bin sizes to 1, 2, 4, 8, 16, 32, and 64 to ensure we have more data points than model parameters, since this observation only consists of 1580 exposures.

We also tested PSF-fitting centering and optimal photometry methods (Horne 1986, Deming et al. 2005, Cubillos et al. 2014b). Using TinyTim[1], we generated a $100\times$-subsampled IRS peak-up camera PSF for a blackbody target at 3416 K (see Figure 5.1). We then fit this subsampled PSF to our data to determine target position, binned down to native data resolution, and scaled the PSF flux to fit our images. This approach slightly reduces the standard deviation of normalized residuals (SDNR), a measure of white noise, but increases χ^2_{bin}.

5.4.6   24 μm

At 24 μm, the noise pixel parameter becomes very large due to significant background levels, which in turn makes the variable-radius circular apertures very large. At such sizes, the apertures frequently contain bad or hot pixels and are discarded. Likewise, the PSF at 24 μm is much wider, leading to the same problem with elliptical apertures. Therefore, we use only fixed-radius circular apertures with this observation. We correct for the background variation described by Crossfield et al. (2010) by calculating and subtracting the background on a frame-by-frame basis.

As with the 16 μm observation, we test PSF-fitting centering and optimal photometry, using a similarly-generated PSF (see Figure 5.1). Again optimal photometry produces less white noise, with $\sim 10\%$ lower SDNR, but increases χ^2_{bin} over fixed-radius circular-aperture photometry.

---

[1] irsa.ipac.caltech.edu/data/SPITZER/docs/dataanalysistools/tools/contributed/general/stinytim/

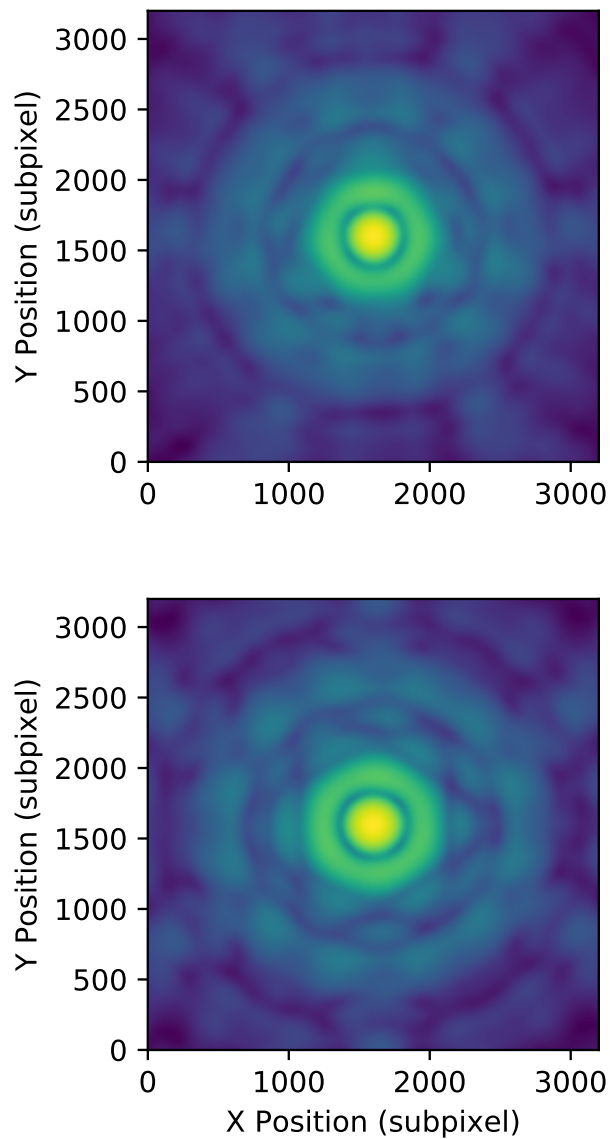Figure 5.1: TinyTim-generated log-scaled PSFs for the 16 μm (top) and 24 μm (bottom) observations. PSFs are 100× subsampled and generated assuming a target effective temperature of 3416 K.

This observation is dithered, with seven positions at each of two telescope nods, for a total of 14 different target locations. We adjust the flux at each dither position by the fraction of the average flux at that position compared to the average flux of the total observation. The dither, combined with the low number of exposures, makes a BLISS map infeasible. PLD cannot be used because nine pixels at each of 14 positions would add 126 model parameters, and we also do not bin the data to avoid binning over multiple dither positions. Therefore, the "BLISS" fit to this data set is Equation 5.3 with $M(x, y) = 1$ and the "PLD" fit is Equation 5.4 with $\sum_{i}^{N} c_i P_i = 1$ and a bin size of 1. In the PLD fit, we allow F_s to vary, as fixing the pixel terms removes the degeneracy mentioned above.

5.4.7   3.6 µm Phase Curve

The 3.6 µm phase curve is fraught with correlated noise, and the phase-curve variation is undetectable. Besides a small number of frames at the start of the observation, we remove the following frames: 83,328 – 83,391, for telescope reaction wheel motion; 295,680 – 317,375, due to increased variance in the background level; 409,210 – 490,751, due to probable stellar activity; and 324,356 – 324,415, 390,922 – 390,975, and 573,508 – 573,567 as these 171 frames are falsely shifted by one pixel due to an on-board processing error. These last frames cannot be salvaged by simply shifting them back, as theprocessing error also affects the pixel values. None of the discarded frames interfere with the eclipses and transit, although together they amount to $\sim 17\%$ of the observation.

Table 5.3: Phase Curve Model Results

Parameter	3.6 μm	8.0 μm
BLISS		
$t_{\mathrm{ecl},1}$ (phase)	0.5854 ± 0.0044	0.5903 ± 0.0007
$t_{\mathrm{ecl},1}$ (MBJD)	8361.86068 ± 0.00975	4660.41980 ± 0.00174
D_1 (ppm)	318 ± 128	698 ± 130
$t_{14,1}$ (phase)	0.0086 ± 0.0064	0.0131 ± 0.0017
$t_{\mathrm{ecl},2}$ (phase)	1.5960 ± 0.0035	1.5868 ± 0.0019
$t_{\mathrm{ecl},2}$ (MBJD)	8364.53288 ± 0.00371	4663.05453 ± 0.00487
D_2 (ppm)	179 ± 53	330 ± 87
$t_{14,2}$ (phase)	0.0289 ± 0.0044	0.0175 ± 0.0042
t_{tr} (phase)	1.00134 ± 0.00004	1.00023 ± 0.00005
t_{tr} (MBJD)	8362.95999 ± 0.00010	4661.50289 ± 0.00013
R_p/R_*	0.08000 ± 0.00042	0.08299 ± 0.00053
$\cos(i)$	0.05750 ± 0.00018	0.05793 ± 0.00022
A_0 (ppm)	0 ± 3	118 ± 40
t_1 (phase)	0.5500 ± 0.0291	0.5466 ± 0.0634
PLD[a]		
$t_{\mathrm{ecl},1}$ (phase)	0.5875 ± 0.0036	0.5901 ± 0.0008
$t_{\mathrm{ecl},1}$ (MBJD)	8361.86646 ± 0.00963	4660.41922 ± 0.00217
D_1 (ppm)	196 ± 88	774 ± 135
$t_{14,1}$ (phase)	0.0173 ± 0.0065	0.0144 ± 0.0021
$t_{\mathrm{ecl},2}$ (phase)	1.5890 ± 0.0023	1.5868 ± 0.0018
$t_{\mathrm{ecl},2}$ (MBJD)	8364.51454 ± 0.00614	4663.05439 ± 0.00468
D_2 (ppm)	263 ± 151	351 ± 88
$t_{14,2}$ (phase)	0.0152 ± 0.0052	0.0175 ± 0.0040

[a] With PLD we restrict the fit to a region around the eclipses.

We initially fit this observation with the exponential ramp function (see Equation 5.5) and the phase-curve variation in Equation 5.9, but we find that the ramp function and the asymmetric cosine term A_2 of the phase-curve function are not justified in a BIC comparison. Removing both from our model improves the BIC by ~ 25. We achieve the best χ^2_{bin} with least-asymmetry centering and a 2.25-pixel circular aperture. Table 5.3 lists the best-fitting model parameters, and Figure 5.2 displays the phase curve (using the best joint fit from section 5.4.9), with the BLISS model divided out.
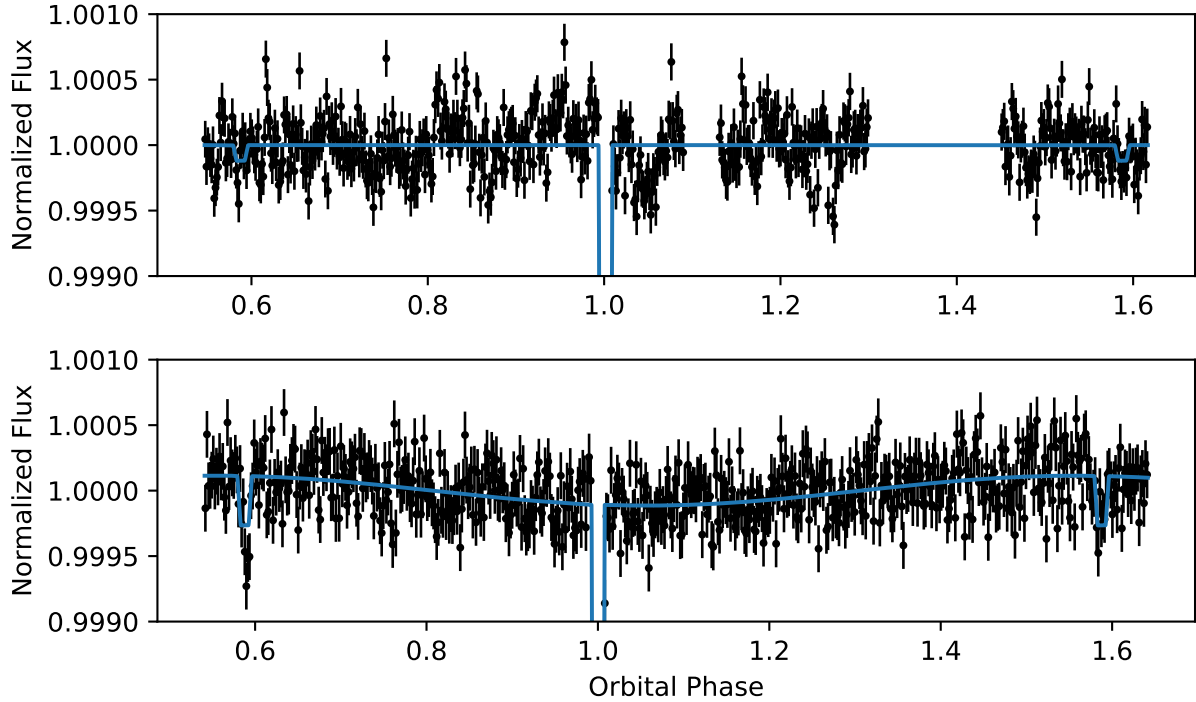
Figure 5.2: Jointly-fit phase curves modeled with BLISS. **Top:** The 3.6 μm phase curve. See text for description of data gaps. Phase curve variation is too weak to be detected. **Bottom:** The 4.5 μm phase curve.

As mentioned above, PLD performs poorly on long observations like phase curves. Thus, we restrict our PLD fits to small regions around the two eclipses and model them as we would individual eclipses, with the BIC-optimized ramp models and no orbital emission variation. For the first eclipse, we model until 0.61 orbital phase (with the same discarded frames as the BLISS fit), and for the second eclipse we model from 0.54 orbital phase until the end of the observation. We use center-of-light centering with 2.5-pixel circular apertures with a bin size of 8 for the first eclipse, and center-of-light centering with $a = 1.5$, $b = -1.0$, variable, circular apertures and a bin size of 16 for the second eclipse. These results are also listed in Table 5.3, with the unused parameters omitted.

To compare BLISS and PLD model results, we also fit BLISS models to the same region of the light curve. For the first eclipse, using the quadratic ramp model, Gaussian centering, and $a = 6.0$, $b = -1.0$, elliptical apertures, we find $t_{\text{ecl},1} = 0.5793 \pm 0.0028$ orbital phase, $D_1 = 281 \pm 86$, and $t_{14,1} = 0.0209 \pm 0.0033$ orbital phase. For the second eclipse, using a flat ramp model, Gaussian centering, and $a = 1.0$, $b = -0.5$, variable apertures, we find $t_{\text{ecl},2} = 0.5911 \pm 0.0016$ orbital phase, $D_2 = 416 \pm 121$, and $t_{14,2} = 0.0100 \pm 0.0037$ orbital phase. This D_2 is 1.8σ deeper than the BLISS depth of the same eclipse when modeling the full phase curve, and consistent with the PLD depth at 0.8σ. Differences are small compared to uncertainties.

5.4.8   8.0 μm Phase Curve

The 8.0 μm phase curve has well-defined phase-curve variation, with two well-constrained eclipses. Initially, we fit the phase-curve variation with Equation 5.9, but we find the second cosine term is unjustified. By setting $A_2 = 0$, we improve the BIC of the model by ~ 25, so we use a single-cosine model for the phase-curve variation. The uncertainty on t_1 is too high for a confident detection of a hot-spot offset. We use least-asymmetry centering and $a = 1.25$, $b = 1.5$, variable, circular photometry. Table 5.3 lists the model parameters and uncertainties for this observation. The full phase curve and model, using the joint-fit parameters determined in section 5.4.9, is shown in Figure 5.2.

We use the same procedure for PLD fits as used with the 3.6 μm phase curve. For the first eclipse, we use Gaussian centering with $a = 1.5$, $b = 2.0$, variable, circular apertures and a bin size of 16, and for the second eclipse we use Gaussian centering with $a = 7.0$, $b = 1.0$, elliptical apertures and a bin size of 16.

As with the 3.6 μm phase curve, we also fit BLISS models to light-curve region used in the PLD fits. For the first eclipse, using the quadratic ramp model, Gaussian centering, and $a = 1.0$, $b = 1.0$, variable apertures, we find $t_{\text{ecl},1} = 0.5894 \pm 0.0010$ orbital phase, $D_1 = 737 \pm 96$, and $t_{14,1} = 0.0163 \pm 0.0024$ orbital phase. For the second eclipse, using a flat ramp model, least-asymmetry centering, and $a = 1.5$, $b = -1.0$, variable apertures, we find $t_{\text{ecl},2} = 0.5868 \pm 0.0020$ orbital phase, $D_2 = 338 \pm 88$, and $t_{14,2} = 0.0164 \pm 0.0044$ orbital phase. These fits are within 0.5σ of the PLD fits to the individual eclipses and within 1.1σ of the BLISS fit to the full phase curve.

5.4.9 Jointly-fit Light Curves

We also fit all our light curves jointly, with both BLISS and PLD, to share parameters between models, thereby reducing uncertainties. We expect that eclipse phase and eclipse duration should be the same for each observation, or at least well within the constraints of our data. Also, we expect that eclipse depth should be consistent between measurements with the same filter. Therefore we simultaneously fit all our light curves, with free parameters for 3.6 μm, 4.5 μm, 5.8 μm, 8.0 μm, 16 μm, and 24 μm eclipse depths, a single t_{ecl}, a single t_{14}, a separate flux term for each observation, separate ramp function parameters for each observation, and different c_i parameters per observation (when using PLD). We use the optimized centering and photometry methods listed in Table 5.2 (it is computationally infeasible to re-optimize for the joint fit). Figure 5.3 shows the resulting BLISS light curve fits, phase-folded at each *Spitzer* filter. Figure 5.4 shows the same for BLISS, and Table 5.4 lists the best-fitting parameters. There are several inconsistencies between the individual eclipse fits and the joint fit (for instance, one might expect a deeper 3.6 μm eclipse based on the individual fits), but eclipse midpoint and duration constraints from the higher S/N observations force adjustments in the fits to the low S/N eclipses.

147

Table 5.4: Joint Fit Model Results

Parameter	BLISS	PLD
3.6 μm D (ppm)	120(20)	207(22)
4.5 μm D (ppm)	17(15)	35(18)
5.8 μm D (ppm)	163(105)	199(63)
8.0 μm D (ppm)	378(26)	411(30)
16 μm D (ppm)	1697(255)	1957(249)
24 μm D (ppm)	1318(506)	1899(192)
3.6 μm T (K)	825(37)	928(33)
4.5 μm T (K)	521(64)	558(56)
5.8 μm T (K)	644(106)	667(61)
8.0 μm T (K)	649(27)	669(28)
16 μm T (K)	1061(120)	1161(120)
24 μm T (K)	811(244)	1055(94)
t_{14} (phase)	0.01737(52)	0.01849(49)
t_{ecl} (phase)	0.58771(24)	0.58777(23)

There are a few minor inconsistencies between our PLD and BLISS results. The 3.6 μm eclipse depths differ by 3σ, which is likely due to the different approaches when modeling the phase curve. As discussed above, with PLD we are forced to fit to a region around the phase curve eclipses, treating them as separate individual eclipse observations, but with BLISS we model the entire observation. Since the two phase curve eclipses amount to half the eclipses in this filter, the differences in phase curve modeling approaches could lead to different results in the joint fit.

With the PLD joint fit, we find that the 16 μm eclipse phase is not fit well by the same eclipse phase that fits the other eclipses. If our assumed period of 2.64389579 days was inaccurate, we would expect the later observations to be even more poorly fit, and BLISS would suffer from the same problem, but this is not the case. When the phases of all eclipses are forced to match, the 16 μm eclipse depth is 589 ppm, significantly lower than when this observation is fit individually, and the fit is clearly poor. Thus, in order to accurately capture the depth of this eclipse, we allow
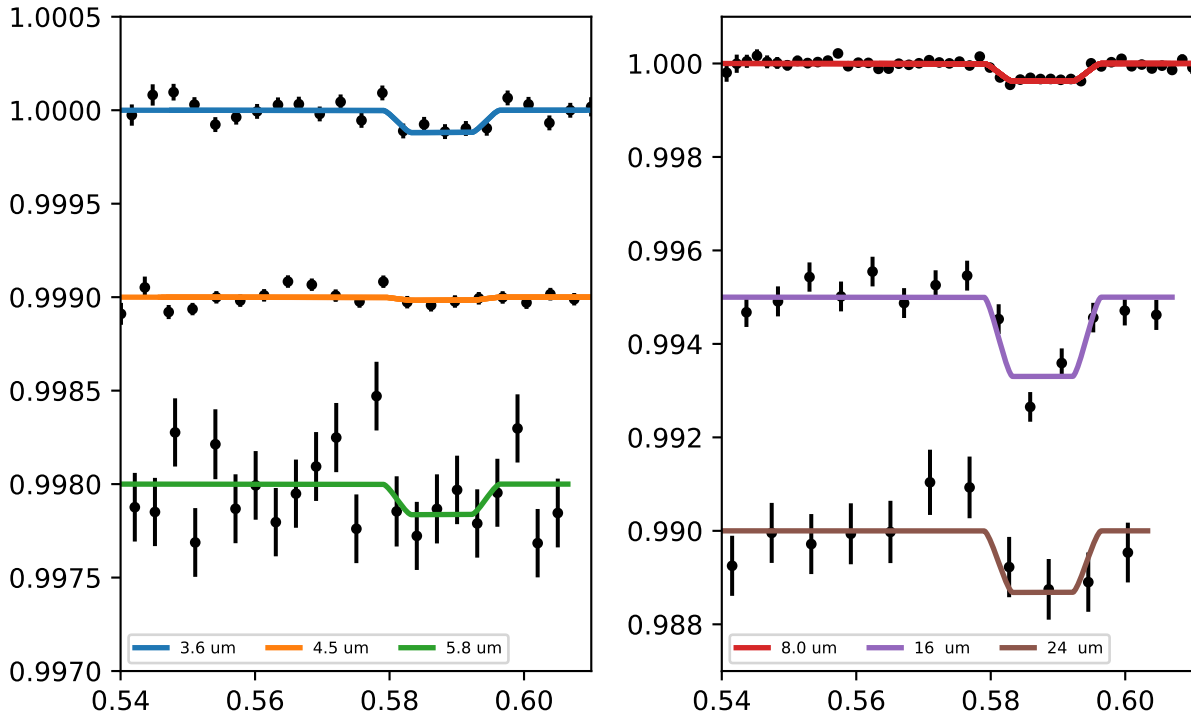
Figure 5.3: Jointly-fit BLISS light curves and models, phase-folded and binned at each filter. We have divided out the BLISS models (where applicable) and ramp models. The light curves are offset for clarity.

the 16 μm eclipse midpoint to fit separate from the other eclipse timings. We elected to treat every observation in a consistent way, and used the brightest nine pixels in the PLD model for every observation. The PSF is noticeably wider at 16 μm, however, and may require additional pixels to accurately model the photometry, which may have caused the difficulty with PLD fits to this observation.
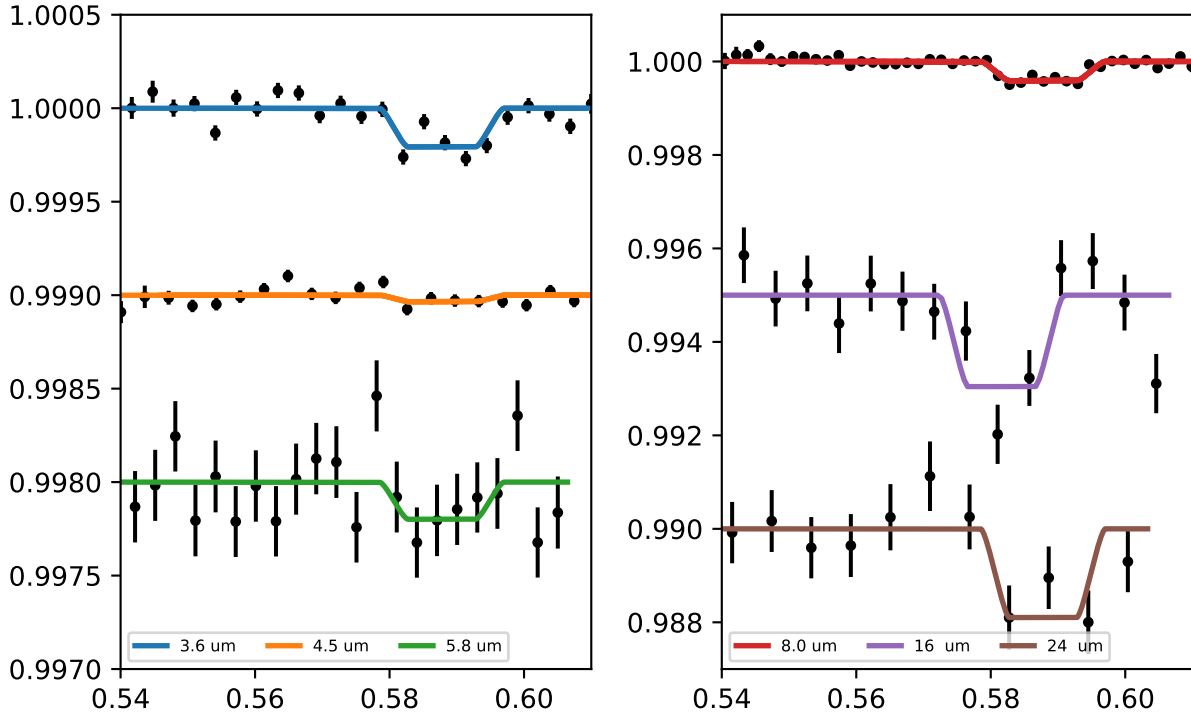
Figure 5.4: Jointly-fit PLD eclipses and models, phase-folded and binned at each filter. We have subtracted the PLD models (where applicable) and ramp models. The light curves are offset for clarity.

We use the MCMC posterior distribution of eclipse depths at each wavelength to run a Monte Carlo calculation of band-integrated temperatures. Assuming the planet is a blackbody and using ATLAS9 stellar spectra (Castelli et al. 1997, http://kurucz.harvard.edu/grids.html), we compute a temperature for eclipse depths sampled from the posterior distribution, and take the standard deviation of the resulting distribution as the uncertainty on the median temperature. These brightness temperatures are listed in Table 5.4. We address the planetary temperature further in Section 5.6.

In the following sections we characterize the planet using both the BLISS and PLD light-curve modeling results. Since the BLISS fit includes more data, and there are issues with the PLD fit to the 16 μm observations, we quote our orbital and atmospheric fits to the BLISS eclipses as our final results. We stress, however, that the PLD light curves lead to very similar results.

5.5   Orbital Analysis

We fit a Keplerian orbit to our modeled eclipse and transit timings (Tables 5.2 and 5.3), transit timings from the literature (Table 5.5), transits from the Exoplanet Transit Database (ETD, var2.astro.cz/ETD/, Table 5.5), and published radial-velocity (RV) data. Eclipse timings can significantly improve uncertainties on eccentricity, and help avoid false positives from RV data alone (Arras et al. 2012). For ETD transits, we require a listed timing uncertainty and a data quality of 3 or lower, where a lower data quality indicates lower uncertainties and faster sampling of the light curve. We use 171 RV measurements from the High Accuracy Radial velocity Planet Searcher (HARPS, Lanotte et al. 2014), 356 from the Keck High Resolution Echelle Spectrograph (HIRES, Butler et al. 2017, Tal-Or et al. 2019), and 113 from the Calar Alto high-Resolution search for M dwarfs with Exoearths with Near-infrared and optical Echelle Spectrographs (CARMENES, Trifonov et al. 2018).

Table 5.5: GJ 436b Transit Events

Transit Midpoint BJD(TDB)	Data Quality[a]	Source
2458886.45068 ± 0.00075	3	Hentunen V.
2458878.52815 ± 0.00073	3	Wünsche A.
2458870.59354 ± 0.00089	3	Raetz M.
2458619.41977 ± 0.00085	3	Wünsche A.
2458582.40344 ± 0.00072	3	Wünsche A.
2458566.54082 ± 0.0008	3	Jongen Y.
2458566.53638 ± 0.00086	3	Scaggiante F., Zardin D.
2458545.39767 ± 0.0009	3	Plazas J.
2458537.45532 ± 0.00061	3	Guerra P.
2458529.52763 ± 0.00075	3	Scaggiante F., Zardin D.
2458529.52659 ± 0.00062	3	Jongen Y.
2458241.34936 ± 0.00107	3	Nosál P.
2458241.34389 ± 0.00144	3	Nosál P.
2458233.41288 ± 0.00054	3	Jongen Y.
2458233.40946 ± 0.0009	3	Scaggiante F., Zardin D.
2458172.59964 ± 0.00075	3	Molina D.
2457855.33530 ± 0.00098	3	Bretton M.
2457810.38214 ± 0.001	3	Gaitan J.
2457797.16604 ± 0.00074	3	Kang W.
2457437.59529 ± 0.0008	3	Molina D.
2457149.41112 ± 0.00075	3	Garcia F.
2457096.53319 ± 0.00081	3	Hentunen V.
2457067.45185 ± 0.00095	3	Vrašťák, M.
2457011.92837 ± 0.00079	3	Benni P.
2456792.48419 ± 0.00058	3	Salisbury M.
2456744.89805 ± 0.00099	3	Shadic S., Aziz U.
2456726.38834 ± 0.00075	3	Sokov E. N.
2456723.74314 ± 0.00063	3	Benni P.
2456681.44051 ± 0.00064	3	Hentunen V.
2456670.86543 ± 0.00043	2	Benni P.
2456662.93479 ± 0.00046	3	Benni P.
2456406.47782 ± 0.00074	3	Garcia F.
2456057.47951 ± 0.00077	3	Carreño A.
2456036.33109 ± 0.00091	3	Sokov E. N.
2456025.75506 ± 0.00094	3	Shadic S.
2455991.38385 ± 0.00071	3	Poddaný S.
2455991.37951 ± 0.00078	3	Lomoz F.
2455967.58830 ± 0.00078	3	Slesarenko V., Sokov E.

Transit Midpoint BJD(TDB)	Data Quality[a]	Source
$2455935.86277 \pm 0.00105$	3	Shadic S.
$2455930.57086 \pm 0.00086$	3	Lopesino J.
$2455922.64000 \pm 0.00081$	3	Naves R.
$2455679.40313 \pm 0.00077$	3	Sergison D.
$2455676.75972 \pm 0.00065$	3	Shadic S.
$2455676.75918 \pm 0.00088$	3	Shadic S.
$2455671.46785 \pm 0.00068$	3	Scarmato T.
$2455650.32028 \pm 0.00097$	3	Hentunen V.
$2455634.45769 \pm 0.00115$	3	Gajdoš Š., Vilgi J.
$2455634.45599 \pm 0.00078$	3	Sergison D.
$2455626.52402 \pm 0.00108$	3	Nicolas E.
$2455626.52284 \pm 0.00068$	3	Herrero E.
$2455594.79725 \pm 0.00087$	3	Shadic S.
$2455573.64352 \pm 0.00102$	3	Naves R.
$2455293.39500 \pm 0.00135$	3	Corfini G.
$2455293.39402 \pm 0.00095$	3	Thomas S.
2455269.60178 ± 0.0009	3	Zambelli R.
$2455253.73482 \pm 0.00075$	3	Tieman B.
$2455253.73482 \pm 0.00075$	3	Tieman B.
2454944.39982 ± 0.0012	3	Gregorio
$2454936.47019 \pm 0.00099$	3	Trnka J.
2454915.31682 ± 0.0009	3	Hentunen V.
2454899.45552 ± 0.0009	3	Naves R.
2454862.43949 ± 0.0009	3	Marchini A.
$2454862.43906 \pm 0.00103$	3	Zambelli R.
$2454600.69796 \pm 0.00118$	1	Coughlin et al. (2008)
$2454592.76282 \pm 0.00084$	1	Coughlin et al. (2008)
$2454592.76203 \pm 0.00177$	1	Coughlin et al. (2008)
2454592.76124 ± 0.0014	1	Coughlin et al. (2008)
$2454584.83302 \pm 0.00117$	1	Coughlin et al. (2008)
$2454584.83085 \pm 0.00035$	1	Coughlin et al. (2008)
2454584.83071 ± 0.0014	3	Gary
$2454584.82869 \pm 0.00166$	1	Coughlin et al. (2008)
$2454563.67969 \pm 0.00051$	1	Coughlin et al. (2008)
$2454563.67938 \pm 0.00257$	1	Coughlin et al. (2008)
$2454558.39250 \pm 0.00099$	3	Lopresti C.
2454547.81531 ± 0.0014	3	Gary
$2454534.59612 \pm 0.00014$	1	Alonso et al. (2008)
2454531.95131 ± 0.0018	3	Schwartz
2454505.51561 ± 0.0022	3	Mendez

Transit Midpoint BJD(TDB)	Data Quality[a]	Source
2454497.57901 ± 0.0025	3	Naves
2454455.27925 ± 0.00026	1	Bean et al. (2008)
2454280.78211 ± 0.00011	1	Southworth (2008)
2454280.78186 ± 0.00015	1	Gillon et al. (2007a)
2454280.78149 ± 0.00016	1	Deming et al. (2007)
2454246.41012 ± 0.00079	1	Shporer et al. (2009)
2454225.26052 ± 0.00089	1	Shporer et al. (2009)
2454225.26050 ± 0.00072	1	Shporer et al. (2009)
2453381.85582 ± 0.00179	2	Coughlin et al. (2008)

[a] Data quality ranges from 1 (best) to 5 (worst). The ETD assigns quality ratings based on light-curve uncertainties and sampling rate. We use timings with quality ratings of 3 or better.

For our fitting, we use a version of RadVel (Fulton et al. 2018) modified to fit to transit and eclipse timings as well as radial velocities. RadVel fits a Keplerian orbit described by the orbital period P, transit epoch t_{tr}, eccentricity e, and angle of periastron ω, as well as the RV semi-amplitude K, relative system velocity γ (for each instrument), relative system acceleration $\dot{\gamma}$, and the acceleration time derivative $\ddot{\gamma}$. We solve for the γ velocity terms directly, so they do not vary in the MCMC. We also fit to a jitter parameter j for each RV instrument, which is added in quadrature to the RV measurement uncertainties to account for unmodeled astrophysical and systematic noise sources.

To assess the reliability of our light-curve modeling, we fit, separately, to the BLISS and PLD eclipse midpoints. Figure 5.5 shows the orbital fits to the RV data, eclipse times, and transit times. The best-fitting parameters and uncertainties are listed in Table 5.6. The parameters retrieved from the BLISS and PLD eclipses agree within 0.5σ.
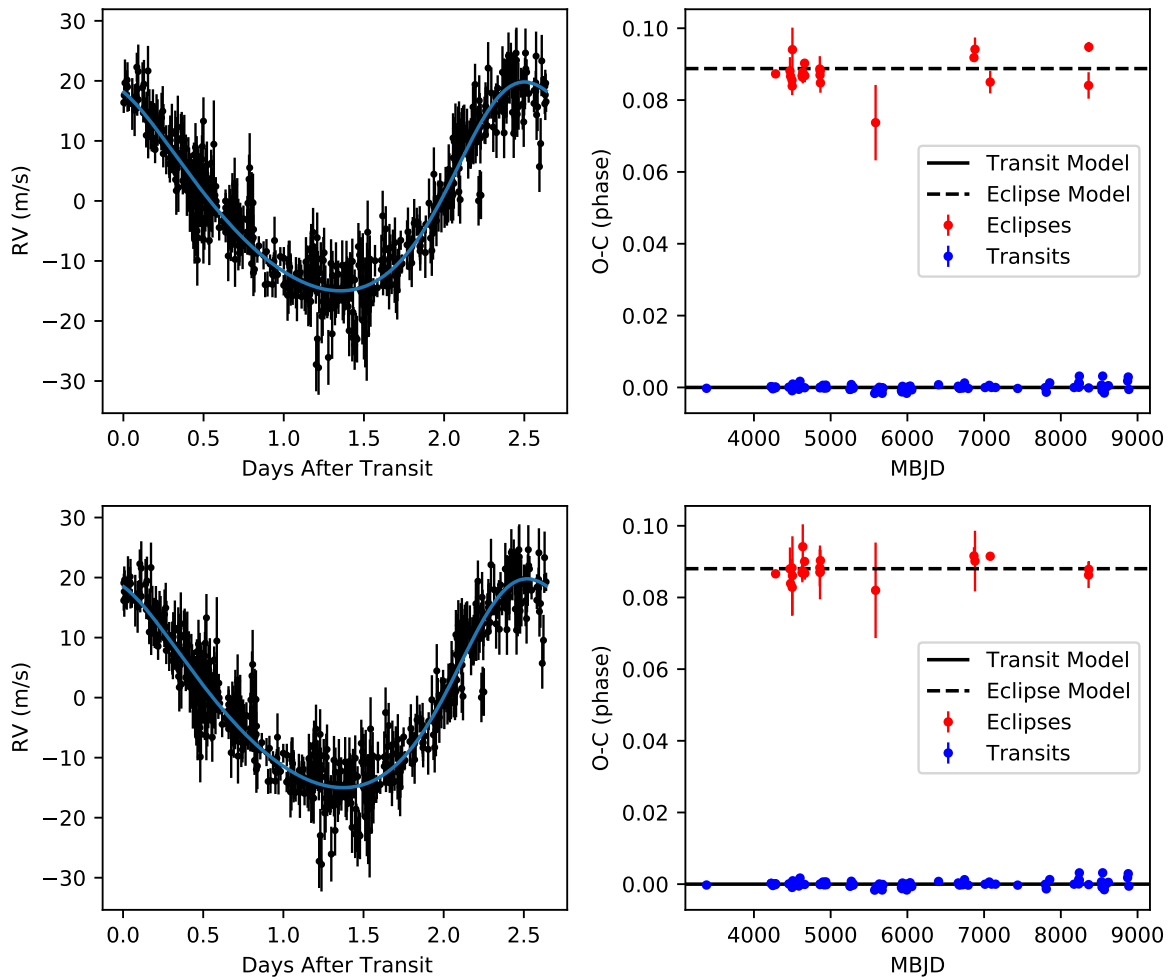
Figure 5.5: Orbital fits to the RV, transit, and eclipse data. The left column shows the phase-folded fit to the RV data, with γ subtracted. The right column shows the observed minus calculated (O-C) of the transit and eclipse times, where transits are relative to 0 orbital phase and eclipses are relative to 0.5 orbital phase. The top row shows fits to the BLISS eclipse data and the bottom row shows fits to the PLD eclipse data. Phase is relative to the fitted transit times in Table 5.6.

Table 5.6: GJ436b Orbit Fit Results

Parameter	BLISS	PLD
Fitted		
P (d)	2.643898036(67)	2.643898014(69)
t_{tr} (MBJD)	4222.616028(57)	4222.616040(57)
$\sqrt{e}\cos\omega$	0.3347(54)	0.3329(53)
$\sqrt{e}\sin\omega$	-0.247(18)	-0.247(17)
$\ln K$ (m s^{-1})	2.8566(89)	2.8564(87)
$\dot{\gamma}$ (m s^{-1} d^{-1})	-0.00011(28)	-0.00011(29)
$\ddot{\gamma}$ (m s^{-1} d^{-2})	-0.00000016(16)	-0.00000016(16)
γ_{HARPS} (m s^{-1})	9791.11	9791.12
γ_{HIRES} (m s^{-1})	0.58	0.58
$\gamma_{\mathrm{CARMENES}}$ (m s^{-1})	-19.80	-19.80
j_{HARPS} (m s^{-1})	1.22(13)	1.22(13)
j_{HIRES} (m s^{-1})	3.19(20)	3.19(20)
j_{CARMENES} (m s^{-1})	1.71(22)	1.71(22)
Derived		
e	0.1729(52)	0.1718(52)
$\omega(°)$	323.6(24)	323.4(23)
K (m s^{-1})	17.40(15)	17.40(15)

5.6 Atmospheric Retrieval

We used the Bayesian Atmospheric Radiative Transfer code (BART, Harrington et al. 2020, Cubillos et al. 2020, Blecic et al. 2020, `https://github.com/exosports/BART`) to retrieve the day-side atmosphere of GJ 436b. BART has three main modules: Thermochemical Equilibrium Abundances (TEA, Blecic et al. 2016), which calculates abundances of molecular constituents at given pressures and temperatures; MC^3 (Cubillos et al. 2017), an MCMC wrapper; and Transit (Rojo 2006), a line-by-line radiative-transfer code. TEA calculates the initial state of the atmosphere, although uniform abundances or custom atmospheres can be used in its place. MC^3 runs Markov-chain Monte Carlo which proposes new atmospheres, and calls Transit to compute the emission spectra of those atmospheres which are then integrated and compared to our eclipse measurements.

We parameterize the atmospheric thermal structure with the temperature profile of Line et al. (2013). This thermal profile has five parameters: κ_{IR}, the thermal Planck mean opacity; γ_1 and γ_2, the ratios of two visible streams to the infrared stream; α, a parameter ranging from $0-1$ that divides flux between the visible streams; and β, a scaling factor on the irradiative temperature to account for albedo and heat redistribution.

Our atmosphere models contain H_2O, CO, CO_2, CH_4, and NH_3, with opacities from the HITRAN/HITEMP line-list databases (Rothman et al. 2010, 2013), and H_2-H_2 collision-induced absorption (Borysow et al. 2001, Borysow 2002). We scale the abundances of these five molecules with free parameter logarithmic factors on the initial pressure-dependent molecular-abundance profiles (scaling is uniform with pressure). We test two cases: pressure-uniform abundance profiles, and thermochemical equilibrium abundances.

In both cases we use uniform priors on all model parameters. The thermal profile parameter boundaries are as follows: $\log\kappa_{\mathrm{IR}}$ from -5 to 1, $\log\gamma_1$ and $\log\gamma_2$ from -4 to 1, α from 0 to 1, and β from 0.55 to 1.2. For uniform abundance profiles, we allow the molar mixing fractions to explore from 10^{-13} to 10% of the atmosphere. With thermochemical equilibrium abundances, we set boundaries of -9 to +3 orders of magnitude on the H_2O, CH_4, and NH_3 abundances, and boundaries of -9.0 to +15 orders of magnitude on the CO and CO_2 abundances (compared to equilibrium). However, there is an additional upper limit on the scaled equilibrium abundances to prevent non-physical (>100%) total abundances in any layer, which is discussed further below.
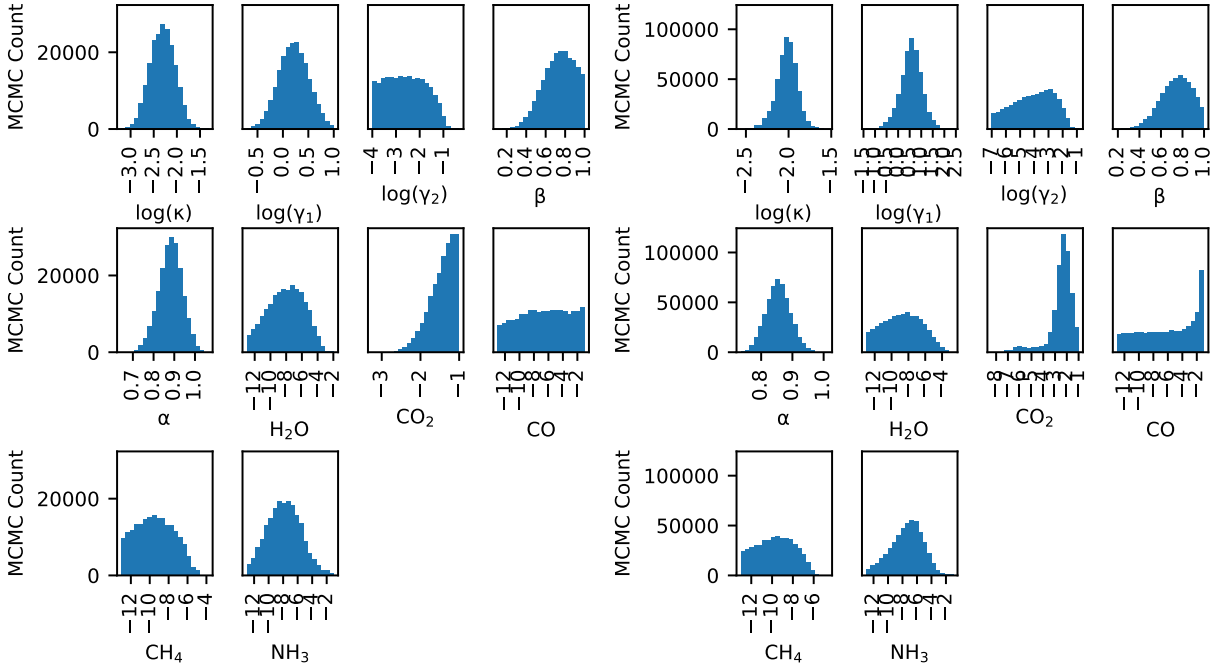
Figure 5.6: Marginalized posterior distributions for the atmosphere model parameters. Molecular parameters are presented as molar fraction of the atmosphere. Thermal profile parameters are unitless. **Left:** Posterior distribution for the fit to BLISS eclipse depths. **Right:** Posterior distribution for the fit to PLD eclipse depths.

5.6.1 Uniform Abundance Profiles

For the uniform abundance cases, we set an upper bound on abundances of 10% of the atmosphere for each molecule, as higher abundances are implausible for a H/He-dominated atmosphere. Using the BLISS eclipse depths, we retrieve an atmosphere with extreme CO_2 abundance, an unconstrained (flat posterior distribution) CO abundance, and low abundances of H_2O, CH_4, and NH_3 (Figure 5.6). H_2O and CH_4 are depleted and CO_2 is enriched compared to thermochemical equilibrium, assuming a solar metallicity (Asplund et al. 2009). The thermal profile is slightly inverted, although a non-inverted atmosphere is well within uncertainties. The planetary emission spectrum fits the data well outside the deep 16 μm eclipse (Figure 5.7, left column).
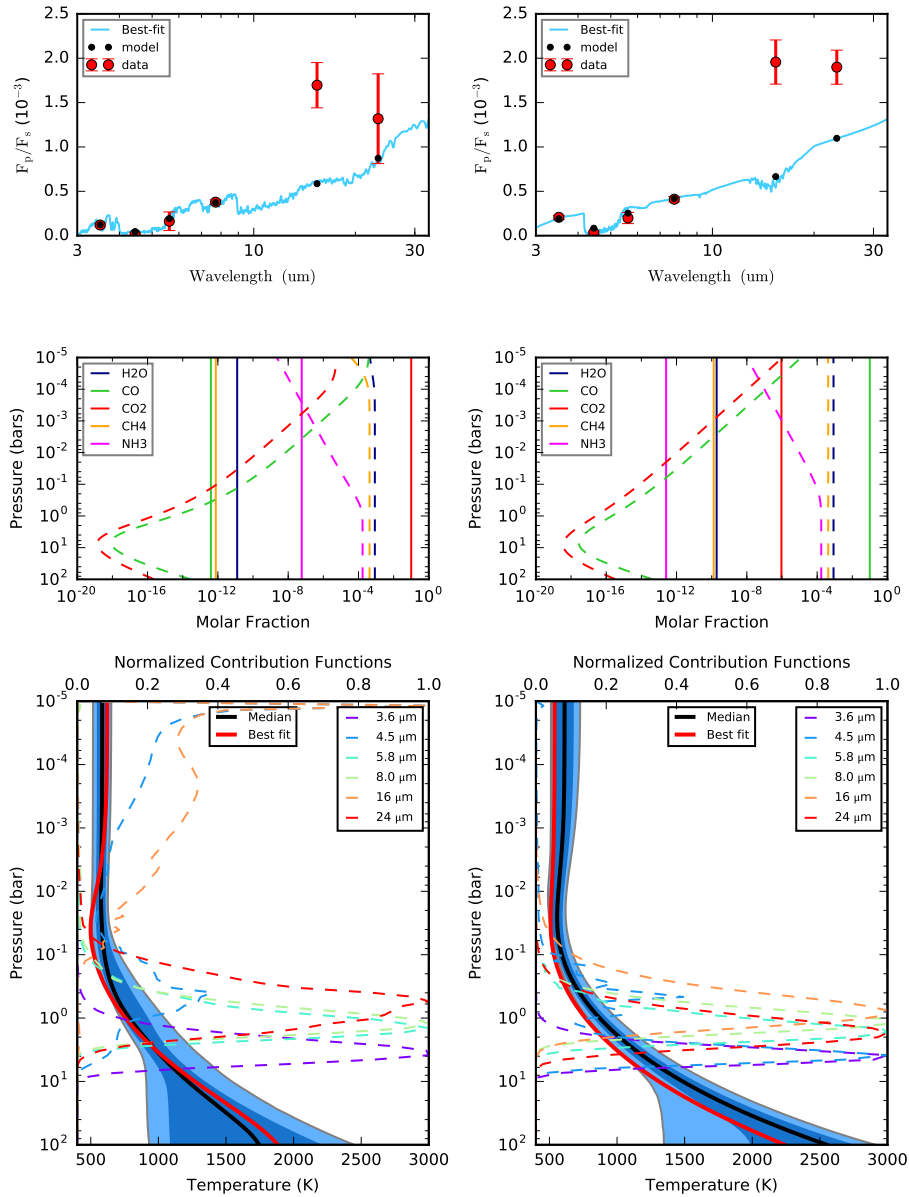
Figure 5.7: BART-retrieved atmospheres for the BLISS (left column) and PLD eclipses (right column). **Top row:** Eclipse depths (red), best-fitting spectrum (blue), and the spectrum integrated over the *Spitzer* filters (black). **Middle row:** Solid lines show the best-fitting atmosphere molecular composition. Dashed lines are the `rate`-computed thermochemical equilibrium abundances using the best-fitting thermal profile. **Bottom row:** The best-fitting thermal structure and normalized contribution functions (dashed), showing the emission source pressures of the atmosphere by filter (the region probed by each filter). Dark- and light-blue regions denote 68% and 95% percentiles of the temperature, computed layer-by-layer using the MCMC posterior.

159

Table 5.7: Convergence Criteria

Light-curve Model	SPEIS	ESS	3σ Region Uncertainty
PLD	1925	322	0.0029
BLISS	3271	92	0.0053

When using the PLD eclipse depths, the retrieved atmosphere is similar. The thermal profile is slightly inverted, and H_2, CH_4, and NH_3 abundances are low and somewhat constrained. However, we instead find a very high CO abundance with a lower, but constrained, CO_2 abundance. The spectral fit is significantly worse than the fit to the BLISS measurements, particularly with the deeper 16 μm and 24 μm eclipses (Figure 5.7, right column).

Following the methods outlined in Harrington et al. (2020), we compute the Steps Per Effectively-Independent Sample (SPEIS), Effective Sample Size (ESS), and uncertainty in the 3σ credible region of our MCMC posterior distribution. A low uncertainty in this credible region indicates that our MCMC posterior distribution has well sampled the true posterior distribution (i.e., we have run sufficient iterations). The results of these calculations are presented in Table 5.7.

5.6.2 *Thermochemical Equilibrium Abundance Profiles*

In an effort to achieve a better fit to our eclipse depths, we also fit an atmosphere with pressure-dependent abundance profiles calculated from thermochemical equilibrium. Using Reliable Analytic Thermochemical Equilibrium (`rate`, Cubillos et al. 2019) and solar atomic abundances (Asplund et al. 2009), we calculate atmospheric molecular abundances assuming the best-fitting thermal structure from the uniform-abundance retrievals. We then scale these abundances by logarithmic scale factors, as was done with the pressure-uniform abundances.

We find these fits are unable to satisfactorily replicate our measurements. As mentioned above, fitting these data requires significant enrichment of CO/CO_2, but in thermochemical equilibrium, these molecules are only present at low and high pressures. Achieving a significant quantity of CO/CO_2 in the $\sim$1 bar region of the atmosphere requires scaling these abundances to $> 100\%$, but MCMC steps in this area of parameter space are rejected outright due to physical impossibility. A different parameterization scheme, like one that fits low-order polynomial abundance profiles, may achieve a better fit than our log-scaling scheme, but our low-resolution spectrum cannot support a model that complex. Likewise, a parameterization scheme that explores metallicity may achieve better atmospheric fits (Moses et al. 2013, Morley et al. 2017).

In keeping with the BART reproducible-research license, the BART version used, inputs, outputs, analysis scripts, and commands used to run the code are all available in a reproducible-research compendium, permanently archived at `https://doi.org/10.5281/zenodo.3759980`. The compendium also includes tables of our optimized photometry and light-curve model fits, as well as nominal diagnostic plots of light-curve correlated noise.

5.7   Conclusions

We analyzed all existing *Spitzer* emission observations of GJ 436b, with a focus on the eclipses, leveraging multiple centering, photometry, and light-curve modeling methods to best mitigate correlated noise. Then, we combined our eclipse timings with RV data from HARPS, HIRES, and CARMENES, amateur transit timings, and transits in the literature to refine GJ 436b's orbital parameters. Finally, we retrieved the atmosphere using BART and confirmed the CO/CO_2 enrichment reported by previous analyses (Stevenson et al. 2010, Lanotte et al. 2014).

By using both BLISS and PLD, we cross-check our results and increase confidence in our measurements. While our measurements using BLISS and PLD differ for individual eclipses, the jointly-fit results, averaged over all observations, are consistent within 1.6σ except in the 3.6 μm eclipse depth, which differ by 3σ. Due to PLD's limitations modeling phase curves, we were forced to restrict PLD fits to a small region around the eclipses. Since we discarded one 3.6 μm observation due to stellar activity, the 3.6 μm phase curve amounts to 50% of the 3.6 μm eclipses. This different approach to modeling the phase curves likely explains the difference in eclipse depths with this filter. Both methods confirm the low 4.5 μm emission previously measured (Stevenson et al. 2010, Lanotte et al. 2014).

We extended the open-source RadVel orbit-modeling package to fit to transit and eclipse times, and used it to fit an orbit to our individually-modeled eclipses and phase curves, RV data, and transits to characterize the orbit of GJ 436b. We measure a period of $2.643898036 \pm 6.7 \times 10^{-7}$ days and an eccentricity of 0.1729 ± 0.0052.

Finally, we applied BART to retrieve the atmosphere of GJ 436b, separately fitting to our BLISS and PLD measurements. With the BLISS measurements we find an enrichment of CO_2 and with the PLD measurements we determine an enrichment of CO, in agreement with previous findings (Stevenson et al. 2010, Lanotte et al. 2014). In both cases, the thermal profile is slightly inverted, although a non-inverted atmosphere is well within uncertainties. We fit to both uniform abundance profiles and thermochemical equilibrium abundance profiles, but only uniform abundances were able to achieve satisfactory fits, although none of our models were able to replicate our measured 16 μm emission. A more complex model with flexible molecular abundance profiles or variable metallicity may do better, although the limited spectral resolution of our data restrict the justifiable complexity of our modeling. Further observation with the *James Webb Space Telescope* should provide the spectral resolution and S/N necessary to begin to understand GJ 436b's unusual atmosphere.

5.8 Acknowledgments

5.9 List of References

Alonso, R., Barbieri, M., Rabus, M., Deeg, H. J., Belmonte, J. A., & Almenara, J. M. 2008, A&A, 487, L5

Anderson, D. R., Smith, A. M. S., Lanotte, A. A., Barman, T. S., Collier Cameron, A., Campo, C. J., Gillon, M., Harrington, J., Hellier, C., Maxted, P. F. L., Queloz, D., Triaud, A. H. M. J., & Wheatley, P. J. 2011, MNRAS, 416, 2108

Arras, P., Burkart, J., Quataert, E., & Weinberg, N. N. 2012, MNRAS, 422, 1761

Asplund, M., Grevesse, N., Sauval, A. J., & Scott, P. 2009, ARA&A, 47, 481

Ballard, S., Charbonneau, D., Deming, D., Knutson, H. A., Christiansen, J. L., Holman, M. J., Fabrycky, D., Seager, S., & A'Hearn, M. F. 2010a, PASP, 122, 1341

Ballard, S., Christiansen, J. L., Charbonneau, D., Deming, D., Holman, M. J., Fabrycky, D., A'Hearn, M. F., Wellnitz, D. D., Barry, R. K., Kuchner, M. J., Livengood, T. A., Hewagama, T., Sunshine, J. M., Hampton, D. L., Lisse, C. M., Seager, S., & Veverka, J. F. 2010b, ApJ, 716, 1047

Bean, J. L., Benedict, G. F., Charbonneau, D., Homeier, D., Taylor, D. C., McArthur, B., Seifahrt, A., Dreizler, S., & Reiners, A. 2008, A&A, 486, 1039

Benneke, B., Knutson, H. A., Lothringer, J., Crossfield, I. J. M., Moses, J. I., Morley, C., Kreidberg, L., Fulton, B. J., Dragomir, D., Howard, A. W., Wong, I., Désert, J.-M., McCullough, P. R., Kempton, E. M. R., Fortney, J., Gilliland , R., Deming, D., & Kammer, J. 2019, Nature Astronomy, 3, 813

Blecic, J., Harrington, J., & Bowman, M. O. 2016, ApJS, 225, 4

Blecic, J., Harrington, J., Cubillos, P. E., Bowman, M. O., Rojo, P., Stemm, M. M., Challener, R. C., Foster, A. J., Dobbs-Dixon, I., Foster, A. S., Lust, N. B., Blumenthal, S. D., Bruce, D., Himes, M. D., & Loredo, T. J. 2020, ApJ,in prep

Blecic, J., Harrington, J., Madhusudhan, N., Stevenson, K. B., Hardy, R. A., Cubillos, P. E., Hardin, M., Bowman, O., Nymeyer, S., Anderson, D. R., Hellier, C., Smith, A. M. S., & Collier Cameron, A. 2014, ApJ, 781, 116

Blecic, J., Harrington, J., Madhusudhan, N., Stevenson, K. B., Hardy, R. A., Cubillos, P. E., Hardin, M., Campo, C. J., Bowman, W. C., Nymeyer, S., Loredo, T. J., Anderson, D. R., & Maxted, P. F. L. 2013, ApJ, 779, 5

Borysow, A. 2002, A&A, 390, 779

Borysow, A., Jorgensen, U. G., & Fu, Y. 2001, J. Quant. Spec. Radiat. Transf., 68, 235

Bourrier, V., Lovis, C., Beust, H., Ehrenreich, D., Henry, G. W., Astudillo-Defru, N., Allart, R., Bonfils, X., Ségransan, D., Delfosse, X., Cegla, H. M., Wyttenbach, A., Heng, K., Lavie, B., & Pepe, F. 2018, Nature, 553, 477

Butler, R. P., Vogt, S. S., Laughlin, G., Burt, J. A., Rivera, E. J., Tuomi, M., Teske, J., Arriagada, P., Diaz, M., Holden, B., & Keiser, S. 2017, AJ, 153, 208

Butler, R. P., Vogt, S. S., Marcy, G. W., Fischer, D. A., Wright, J. T., Henry, G. W., Laughlin, G., & Lissauer, J. J. 2004, ApJ, 617, 580

Castelli, F., Gratton, R. G., & Kurucz, R. L. 1997, A&A, 318, 841

Challener, R. C., Harrington, J., Cubillos, P. E., Blecic, J., Deming, D., & Hellier, C. 2020a, PSJ, , in prep

Challener, R. C., Harrington, J., Cubillos, P. E., Garland, J., Foster, A. S. D., Blecic, J., Foster, A. J., & Smalley, B. 2020b, PSJ, in prep

Challener, R. C., Harrington, J., Jenkins, J. S., Kurtovic, N. T., Ramirez, R., Peña, J., McIntyre, K. J., Himes, M. D., Rodríguez, E., Anglada-Escudé, G., Dreizler, S., Ofir, A., Peña Rojas, P. A., Ribas, I., Rojo, P., Kipping, D., Butler, R. P., Amado, P. J., Rodríguez-López, C., Kempton, E. M. R., Palle, E., & Murgas, F. 2020c, PSJ, in prep

Charbonneau, D., Allen, L. E., Megeath, S. T., Torres, G., Alonso, R., Brown, T. M., Gilliland, R. L., Latham, D. W., Mandushev, G., O'Donovan, F. T., & Sozzetti, A. 2005, ApJ, 626, 523

Claret, A. & Bloemen, S. 2011, A&A, 529, A75

Coughlin, J. L., Stringfellow, G. S., Becker, A. C., López-Morales, M., Mezzalira, F., & Krajci, T. 2008, ApJ, 689, L149

Crossfield, I. J. M., Hansen, B. M. S., Harrington, J., Cho, J. Y. K., Deming, D., Menou, K., & Seager, S. 2010, ApJ, 723, 1436

Cubillos, P., Harrington, J., Loredo, T. J., Lust, N. B., Blecic, J., & Stemm, M. 2017, AJ, 153, 3

Cubillos, P., Harrington, J., Madhusudhan, N., Foster, A. S. D., Lust, N. B., Hardy, R. A., & Bowman, M. O. 2014a, ApJ, 797, 42

—. 2014b, ApJ, 797, 42

Cubillos, P., Harrington, J., Madhusudhan, N., Stevenson, K. B., Hardy, R. A., Blecic, J., Anderson, D. R., Hardin, M., & Campo, C. J. 2013, ApJ, 768, 42

Cubillos, P. E., Blecic, J., & Dobbs-Dixon, I. 2019, ApJ, 872, 111

Cubillos, P. E., Harrington, J., Blecic, J., Himes, M. D., Rojo, P. M., Loredo, T. J., Lust, N. B., Challener, R. C., Foster, A. J., Stemm, M. M., Foster, A. S., & Blumenthal, S. D. 2020, ApJ, in prep

Deming, D., Harrington, J., Laughlin, G., Seager, S., Navarro, S. B., Bowman, W. C., & Horning, K. 2007, ApJ, 667, L199

Deming, D., Knutson, H., Kammer, J., Fulton, B. J., Ingalls, J., Carey, S., Burrows, A., Fortney, J. J., Todorov, K., Agol, E., Cowan, N., Desert, J.-M., Fraine, J., Langton, J., Morley, C., & Showman, A. P. 2015, ApJ, 805, 132

Deming, D., Seager, S., Richardson, L. J., & Harrington, J. 2005, Nature, 434, 740

Deming, D., Wilkins, A., McCullough, P., Burrows, A., Fortney, J. J., Agol, E., Dobbs-Dixon, I., Madhusudhan, N., Crouzet, N., Desert, J.-M., Gilliland, R. L., Haynes, K., Knutson, H. A., Line, M., Magic, Z., Mandell, A. M., Ranjan, S., Charbonneau, D., Clampin, M., Seager, S., & Showman, A. P. 2013, ApJ, 774, 95

Demory, B. O., Gillon, M., Barman, T., Bonfils, X., Mayor, M., Mazeh, T., Queloz, D., Udry, S., Bouchy, F., Delfosse, X., Forveille, T., Mallmann, F., Pepe, F., & Perrier, C. 2007, A&A, 475, 1125

Ehrenreich, D., Bourrier, V., Wheatley, P. J., Lecavelier des Etangs, A., Hébrard, G., Udry, S., Bonfils, X., Delfosse, X., Désert, J.-M., Sing, D. K., & Vidal-Madjar, A. 2015, Nature, 522, 459

Fazio, G. G., Hora, J. L., Allen, L. E., Ashby, M. L. N., Barmby, P., Deutsch, L. K., Huang, J.-S., Kleiner, S., Marengo, M., Megeath, S. T., Melnick, G. J., Pahre, M. A., Patten, B. M., Polizotti, J., Smith, H. A., Taylor, R. S., Wang, Z., Willner, S. P., Hoffmann, W. F., Pipher, J. L., Forrest, W. J., McMurty, C. W., McCreight, C. R., McKelvey, M. E., McMurray, R. E., Koch, D. G., Moseley, S. H., Arendt, R. G., Mentzell, J. E., Marx, C. T., Losch, P., Mayman, P., Eichhorn, W., Krebs, D., Jhabvala, M., Gezari, D. Y., Fixsen, D. J., Flores, J., Shakoorzadeh, K., Jungo, R., Hakun, C., Workman, L., Karpati, G., Kichak, R., Whitley, R., Mann, S., Tollestrup, E. V., Eisenhardt, P., Stern, D., Gorjian, V., Bhattacharya, B., Carey, S., Nelson, B. O., Glaccum, W. J., Lacy, M., Lowrance, P. J., Laine, S., Reach, W. T., Stauffer, J. A., Surace, J. A., Wilson, G., Wright, E. L., Hoffman, A., Domingo, G., & Cohen, M. 2004, ApJS, 154, 10

Fulton, B. J., Petigura, E. A., Blunt, S., & Sinukoff, E. 2018, PASP, 130, 044504

Gelman, A. & Rubin, D. B. 1992, Statistical Science, 7, 457

Gillon, M., Demory, B. O., Barman, T., Bonfils, X., Mazeh, T., Pont, F., Udry, S., Mayor, M., & Queloz, D. 2007a, A&A, 471, L51

Gillon, M., Pont, F., Demory, B. O., Mallmann, F., Mayor, M., Mazeh, T., Queloz, D., Shporer, A., Udry, S., & Vuissoz, C. 2007b, A&A, 472, L13

Hardy, R. A., Harrington, J., Hardin, M. R., Madhusudhan, N., Loredo, T. J., Challener, R. C., Foster, A. S. D., Cubillos, P. E., & Blecic, J. 2017, ApJ, 836, 143

Harrington, J., Himes, M. D., Cubillos, P. E., Blecic, J., Rojo, P. M., Challener, R. C., Lust, N. B., Bowman, M. O., Blumenthal, S. D., Dobbs-Dixon, I., Foster, A. S., Foster, A. J., Green, M., Loredo, T. J., McIntyre, K. J., & Stemm, M. M. 2020, ApJ, in prep

Horne, K. 1986, PASP, 98, 609

Knutson, H. A., Benneke, B., Deming, D., & Homeier, D. 2014, Nature, 505, 66

Knutson, H. A., Charbonneau, D., Allen, L. E., Burrows, A., & Megeath, S. T. 2008, ApJ, 673, 526

Kreidberg, L., Bean, J. L., Désert, J.-M., Benneke, B., Deming, D., Stevenson, K. B., Seager, S., Berta-Thompson, Z., Seifahrt, A., & Homeier, D. 2014, Nature, 505, 69

Lanotte, A. A., Gillon, M., Demory, B. O., Fortney, J. J., Astudillo, N., Bonfils, X., Magain, P., Delfosse, X., Forveille, T., Lovis, C., Mayor, M., Neves, V., Pepe, F., Queloz, D., Santos, N., & Udry, S. 2014, A&A, 572, A73

Lewis, N. K., Knutson, H. A., Showman, A. P., Cowan, N. B., Laughlin, G., Burrows, A., Deming, D., Crepp, J. R., Mighell, K. J., Agol, E., Bakos, G. Á., Charbonneau, D., Désert, J.-M., Fischer, D. A., Fortney, J. J., Hartman, J. D., Hinkley, S., Howard, A. W., Johnson, J. A., Kao, M., Langton, J., & Marcy, G. W. 2013, ApJ, 766, 95

Line, M. R., Vasisht, G., Chen, P., Angerhausen, D., & Yung, Y. L. 2011, ApJ, 738, 32

Line, M. R., Wolf, A. S., Zhang, X., Knutson, H., Kammer, J. A., Ellison, E., Deroo, P., Crisp, D., & Yung, Y. L. 2013, ApJ, 775, 137

Lust, N. B., Britt, D., Harrington, J., Nymeyer, S., Stevenson, K. B., Ross, E. L., Bowman, W., & Fraine, J. 2014, PASP, 126, 1092

Mandel, K. & Agol, E. 2002, ApJ, 580, L171

Miller-Ricci Kempton, E., Zahnle, K., & Fortney, J. J. 2012, ApJ, 745, 3

Morello, G., Waldmann, I. P., Tinetti, G., Howarth, I. D., Micela, G., & Allard, F. 2015, ApJ, 802, 117

Morley, C. V., Knutson, H., Line, M., Fortney, J. J., Thorngren, D., Marley, M. S., Teal, D., & Lupu, R. 2017, AJ, 153, 86

Moses, J. I., Line, M. R., Visscher, C., Richardson, M. R., Nettelmann, N., Fortney, J. J., Barman, T. S., Stevenson, K. B., & Madhusudhan, N. 2013, ApJ, 777, 34

Nymeyer, S., Harrington, J., Hardy, R. A., Stevenson, K. B., Campo, C. J., Madhusudhan, N., Collier-Cameron, A., Loredo, T. J., Blecic, J., Bowman, W. C., Britt, C. B. T., Cubillos, P., Hellier, C., Gillon, M., Maxted, P. F. L., Hebb, L., Wheatley, P. J., Pollacco, D., & Anderson, D. R. 2011, ApJ, 742, 35

Raftery, A. E. 1995, Sociological Mehodology, 25, 111

Rojo, P. M. 2006, PhD thesis, Cornell University

Rothman, L. S., Gordon, I. E., Babikov, Y., Barbe, A., Chris Benner, D., Bernath, P. F., Birk, M., Bizzocchi, L., Boudon, V., Brown, L. R., Campargue, A., Chance, K., Cohen, E. A., Coudert, L. H., Devi, V. M., Drouin, B. J., Fayt, A., Flaud, J.-M., Gamache, R. R., Harrison, J. J., Hartmann, J.-M., Hill, C., Hodges, J. T., Jacquemart, D., Jolly, A., Lamouroux, J., Le Roy, R. J., Li, G., Long, D. A., Lyulin, O. M., Mackie, C. J., Massie, S. T., Mikhailenko, S., Müller, H. S. P., Naumenko, O. V., Nikitin, A. V., Orphal, J., Perevalov, V., Perrin, A., Polovtseva, E. R., Richard, C., Smith, M. A. H., Starikova, E., Sung, K., Tashkun, S., Tennyson, J., Toon, G. C., Tyuterev, V. G., & Wagner, G. 2013, J. Quant. Spec. Radiat. Transf., 130, 4

Rothman, L. S., Gordon, I. E., Barber, R. J., Dothe, H., Gamache, R. R., Goldman, A., Perevalov, V. I., Tashkun, S. A., & Tennyson, J. 2010, J. Quant. Spec. Radiat. Transf., 111, 2139

Shporer, A., Mazeh, T., Pont, F., Winn, J. N., Holman, M. J., Latham, D. W., & Esquerdo, G. A. 2009, ApJ, 694, 1559

Southworth, J. 2008, MNRAS, 386, 1644

Stevenson, K. B., Bean, J. L., Fabrycky, D., & Kreidberg, L. 2014a, ApJ, 796, 32

Stevenson, K. B., Bean, J. L., Madhusudhan, N., & Harrington, J. 2014b, ApJ, 791, 36

Stevenson, K. B., Bean, J. L., Seifahrt, A., Désert, J.-M., Madhusudhan, N., Bergmann, M., Kreidberg, L., & Homeier, D. 2014c, AJ, 147, 161

Stevenson, K. B., Harrington, J., Fortney, J. J., Loredo, T. J., Hardy, R. A., Nymeyer, S., Bowman, W. C., Cubillos, P., Bowman, M. O., & Hardin, M. 2012a, ApJ, 754, 136

Stevenson, K. B., Harrington, J., Lust, N. B., Lewis, N. K., Montagnier, G., Moses, J. I., Visscher, C., Blecic, J., Hardy, R. A., Cubillos, P., & Campo, C. J. 2012b, ApJ, 755, 9

Stevenson, K. B., Harrington, J., Nymeyer, S., Madhusudhan, N., Seager, S., Bowman, W. C., Hardy, R. A., Deming, D., Rauscher, E., & Lust, N. B. 2010, Nature, 464, 1161

Stevenson, K. B., Line, M. R., Bean, J. L., Désert, J.-M., Fortney, J. J., Showman, A. P., Kataria, T., Kreidberg, L., & Feng, Y. K. 2017, AJ, 153, 68

Tal-Or, L., Trifonov, T., Zucker, S., Mazeh, T., & Zechmeister, M. 2019, MNRAS, 484, L8

Trifonov, T., Kürster, M., Zechmeister, M., Tal-Or, L., Caballero, J. A., Quirrenbach, A., Amado, P. J., Ribas, I., Reiners, A., Reffert, S., Dreizler, S., Hatzes, A. P., Kaminski, A., Launhardt, R., Henning, T., Montes, D., Béjar, V. J. S., Mundt, R., Pavlov, A., Schmitt, J. H. M. M., Seifert, W., Morales, J. C., Nowak, G., Jeffers, S. V., Rodríguez-López, C., del Burgo, C., Anglada-Escudé, G., López-Santiago, J., Mathar, R. J., Ammler-von Eiff, M., Guenther, E. W., Barrado, D., González Hernández, J. I., Mancini, L., Stürmer, J., Abril, M., Aceituno, J., Alonso-Floriano,

F. J., Antona, R., Anwand-Heerwart, H., Arroyo-Torres, B., Azzaro, M., Baroch, D., Bauer, F. F., Becerril, S., Benítez, D., Berdiñas, Z. M., Bergond, G., Blümcke, M., Brinkmöller, M., Cano, J., Cárdenas Vázquez, M. C., Casal, E., Cifuentes, C., Claret, A., Colomé, J., Cortés-Contreras, M., Czesla, S., Díez-Alonso, E., Feiz, C., Fernández, M., Ferro, I. M., Fuhrmeister, B., Galadí-Enríquez, D., Garcia-Piquer, A., García Vargas, M. L., Gesa, L., Gómez Galera, V., González-Peinado, R., Grözinger, U., Grohnert, S., Guàrdia, J., Guijarro, A., de Guindos, E., Gutiérrez-Soto, J., Hagen, H. J., Hauschildt, P. H., Hedrosa, R. P., Helmling, J., Hermelo, I., Hernández Arabí, R., Hernández Castaño, L., Hernández Hernando, F., Herrero, E., Huber, A., Huke, P., Johnson, E., de Juan, E., Kim, M., Klein, R., Klüter, J., Klutsch, A., Lafarga, M., Lampón, M., Lara, L. M., Laun, W., Lemke, U., Lenzen, R., López del Fresno, M., López-González, M. J., López-Puertas, M., López Salas, J. F., Luque, R., Magán Madinabeitia, H., Mall, U., Mandel, H., Marfil, E., Marín Molina, J. A., Maroto Fernández, D., Martín, E. L., Martín-Ruiz, S., Marvin, C. J., Mirabet, E., Moya, A., Moreno-Raya, M. E., Nagel, E., Naranjo, V., Nortmann, L., Ofir, A., Oreiro, R., Pallé, E., Panduro, J., Pascual, J., Passegger, V. M., Pedraz, S., Pérez-Calpena, A., Pérez Medialdea, D., Perger, M., Perryman, M. A. C., Pluto, M., Rabaza, O., Ramón, A., Rebolo, R., Redondo, P., Reinhardt, S., Rhode, P., Rix, H. W., Rodler, F., Rodríguez, E., Rodríguez Trinidad, A., Rohloff, R. R., Rosich, A., Sadegi, S., Sánchez-Blanco, E., Sánchez Carrasco, M. A., Sánchez-López, A., Sanz-Forcada, J., Sarkis, P., Sarmiento, L. F., Schäfer, S., Schiller, J., Schöfer, P., Schweitzer, A., Solano, E., Stahl, O., Strachan, J. B. P., Suárez, J. C., Tabernero, H. M., Tala, M., Tulloch, S. M., Veredas, G., Vico Linares, J. I., Vilardell, F., Wagner, K., Winkler, J., Wolthoff, V., Xu, W., Yan, F., & Zapatero Osorio, M. R. 2018, A&A, 609, A117

von Braun, K., Boyajian, T. S., Kane, S. R., Hebb, L., van Belle, G. T., Farrington, C., Ciardi, D. R., Knutson, H. A., ten Brummelaar, T. A., López-Morales, M., McAlister, H. A., Schaefer, G., Ridgway, S., Collier Cameron, A., Goldfinger, P. J., Turner, N. H., Sturmann, L., & Sturmann, J. 2012, ApJ, 753, 171

APPENDIX A: OPTIMIZING DATA SETS WITH χ^2_{bin}

[This appendix will be attached to Chapter 2 when published.]

In this work, we choose the optimal centering methods, photometry techniques, and photometry aperture sizes by minimizing χ^2_{bin}, a measurement of residual correlated noise (Deming et al. 2015). Here we describe that calculation in detail. This calculation assesses correlated noise like a root-mean-square vs. bin size plot (see Figure A.1) but in a more quantifiable way.
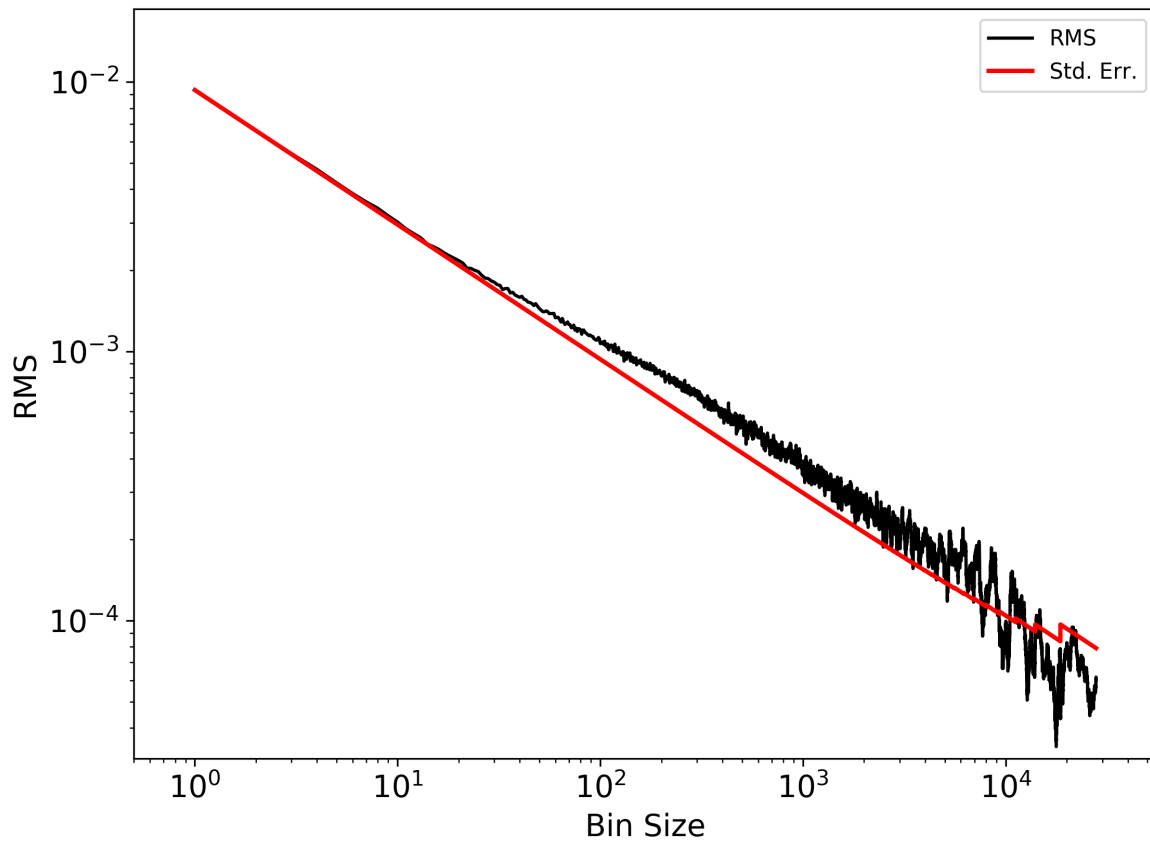

Figure A.1: A plot of the root-mean-squared (RMS) of light-curve model residuals vs. residual bin size compared to theory, assuming only non-correlated noise. Correlated noise is present in the data at a given binning level if the black line (measured RMS) lies above the red line (theoretical RMS).

First, we define the standard deviation of normalized residuals (SDNR) as

$$\text{SDNR} = \sqrt{\frac{1}{N-M} \sum_{i=0}^{N} (r_i - \bar{r})^2},$$

(A.1)

where r_i is the normalized model residual for frame i, $\bar{r}$ is the mean of the normalized residuals, N is the number of frames, and M is the number of free parameters in the model. Normalized model residuals are given by

$$r = \frac{\text{data} - \text{model}}{\text{planetless model}},$$

(A.2)

where the planetless model is the best-fitting model evaluated without any planet terms (i.e., no eclipses, transits, or phase curve variation).

If r contains only white noise, then, when binned, SDNR should decrease (improve) by a factor of $1/\sqrt{\text{bin size}}$, where bin size is the number of frames over which we average. On the other hand, if there is correlated noise in r, binning will not improve the SDNR as much. Thus, we define an Expected SDNR (ESDNR) as

$$\text{ESDNR}_i = \frac{\text{SDNR}_1}{\sqrt{i}},$$

(A.3)

where i is the number of residual points per bin (bin size), SDNR_i is the SDNR with bin size i, and ESDNR_i is the ESDNR at bin size i.

175

We calculate a χ^2 goodness-of-fit measurement for SDNR vs. bin size compared to ESDNR, given by

$$\chi^2_{\mathrm{bin}} = \sqrt{\sum_{i=0}^{n} \left(\frac{\mathrm{SDNR}_{2^i} - \mathrm{ESDNR}_{2^i}}{\sigma_{\mathrm{SDNR}_{2^i}}} \right)^2}, \qquad (A.4)$$

where n is the largest integer possible such that a bin size of 2^n leaves more residual points than free parameters in the light-curve model, but 2^{n+1} does not. σ_{SDNR_i} is the uncertainty on SDNR_i, given by

$$\sigma_{\mathrm{SDNR}_i} = \frac{\mathrm{SDNR}_1}{\sqrt{2N_{\mathrm{bin}}}}, \qquad (A.5)$$

where N_{bin} is the number of residual points left after binning with bin size i. In Equation A.4 we bin by factors of 2^i, creating an evenly distributed number of bin sizes in log space, to avoid biasing χ^2_{bin} toward data sets with less correlated noise at large bin sizes.

A.1   List of References

Deming, D., Knutson, H., Kammer, J., Fulton, B. J., Ingalls, J., Carey, S., Burrows, A., Fortney, J. J., Todorov, K., Agol, E., Cowan, N., Desert, J.-M., Fraine, J., Langton, J., Morley, C., & Showman, A. P. 2015, ApJ, 805, 132